Universität Bremen

Centre for Industrial Mathematics

Deutsches Zentrum für Luft- und Raumfahrt
DLR

Institute of Space Systems

Uncertainty Dispersion Analysis and Optimal Control of Atmospheric Re-Entry

Master Thesis

presented by

B. Sc. Maren Hülsmann

Supervisor: Dr. Matthias Knauer, Centre for Industrial Mathematics, University of Bremen
Supervisor: Dr. Marco Scharringhausen, Institute of Space Systems, DLR Bremen

12th July 2017

Abstract

Uncertainty Dispersion Analysis and Optimal Control of Atmospheric Re-Entry

B.Sc. Maren Hülsmann

In this study, the atmospheric re-entry onto Earth and Mars is analysed with a focus on explicit considerations of uncertainties and evolution thereof. These uncertainties arise in the modelling and the initial entry angle and velocity during the re-entry leading to hazards and malfunctions influencing the mission's success. Therefore, the temporal evolution of uncertainties throughout the re-entry, descent and landing is examined using the Stochastic Liouville Equation.

This equation yields probability density functions depending on the states of the system dynamics and the time. From this a most probable trajectory together with 1-σ and 3-σ error bars are estimated giving an impression on the influence of uncertainties. Furthermore, the covariance matrices are deduced from the probability density functions generating landing dispersions at the end time of the re-entry.

Beside ballistic trajectories also optimal trajectories for manoeuvrable re-entry vehicles are calculated including dispersion analysis. In this case, the re-entry vehicle is controllable in its flight path angle and the trajectories are optimized concerning the descent time.

Math. It's just there ... You're either right or you're wrong. That's what I like about it.

Katherine Johnson
Mathematician at NASA (1953 – 1986)

Contents

Abstract iii

List of Figures ix

List of Tables xi

Nomenclature xiii

1 Introduction 1

1.1 Motivation . . . 1

1.2 Thesis Objective . . . 3

1.3 Structure of this Thesis . . . 3

2 The Re-Entry Problem 5

2.1 Trajectories . . . 6

2.2 Environment Modelling . . . 8

2.2.1 Gravity . . . 9

2.2.2 Atmosphere . . . 10

2.3 Aerodynamics . . . 11

2.4 Re-Entry Dynamics . . . 13

2.4.1 Three State Model . . . 13

2.4.2 Six State Model . . . 20

3 Uncertainty Dispersion Analysis 23

3.1 Fundamentals of Stochastics . . . 23

3.2 Uncertainty Propagation . . . 28

3.3 Analysis of the Three State Model . . . 32

3.3.1 Horizontal Flight . . . 32

3.3.2 Vertical Flight . . . 34
3.3.3 Re-Entry . . . 36
3.4 Most Probable Trajectory . . . 40
3.5 Landing Dispersion from Covariance Matrix . . . 44

4 Optimal Control of Re-Entry Trajectories 49
4.1 Fundamentals in Optimization and Optimal Control . . . 50
4.1.1 Nonlinear Optimization . . . 50
4.1.2 Optimal Control . . . 54
4.2 Optimal Control of the Three State Model . . . 58
4.3 Uncertainty Dispersion Analysis of Optimized Trajectories . . . 65
4.3.1 Temporal Evolution of the PDF . . . 65
4.3.2 Most Probable Trajectory . . . 66

5 Conclusion 69
5.1 Summary . . . 69
5.2 Evaluation of Results . . . 70
5.3 Future Work . . . 71

A Planetary Data 73
A.1 Orbital and Bulk Parameters . . . 73
A.2 Atmosphere Models . . . 73

B Further Investigations of the Three State Model 79
B.1 Optimal Control with Larger Box Constraints . . . 79
B.2 Uncertainty Dispersion Analysis of Optimized Trajectories . . . 81

C Six State Model 83
C.1 Re-Entry . . . 83
C.2 Optimal Control Problem . . . 88

Bibliography 95

List of Figures

1.1 Re-entry, descent and landing of ExoMars . . . 2
1.2 Landing ellipses of ExoMars . . . 3

2.1 The re-entry scenario . . . 5
2.2 Types of re-entry trajectories . . . 7
2.3 Re-Entry Corridor . . . 8
2.4 Gravitational field of Earth and Mars . . . 9
2.5 Earth and Mars Atmosphere Models . . . 10
2.6 Ballistic Coefficient . . . 11
2.7 Lift-to-drag ratio and ballistic coefficient . . . 13
2.8 Descent onto Earth and Mars . . . 14
2.9 Re-Entry onto Earth and Mars for different Atmosphere Models . . . 17
2.10 Re-Entry onto Earth and Mars for different entry velocities . . . 18
2.11 Re-Entry for different parameter settings . . . 19
2.12 The re-entry scenario of the six state model . . . 20

3.1 Density function of the normal distribution . . . 26
3.2 3-sigma-rule . . . 27
3.3 PDF of a Multivariate Normal Distribution . . . 27
3.4 Evolution of the PDF of the one-dimensional example . . . 30
3.5 Error of the PDF of the one-dimensional example . . . 30
3.6 Flow chart of the numerically estimation of the SLE . . . 31
3.7 Evolution of the PDF for horizontal flight . . . 33
3.8 Absolute error in case of horizontal flight . . . 34
3.9 Evolution of the PDF of vertical flight . . . 35
3.10 Absolute error in case of vertical flight . . . 35
3.11 Absolute error of the three state model . . . 37

3.12 Absolute error of the three state model with scaled atmosphere models . . . 37
3.13 Evolution of the PDF for re-entry onto Earth . . . 38
3.14 Evolution of the PDF for re-entry onto Mars . . . 39
3.15 Most probable trajectory for vertical flight . . . 42
3.16 Most probable trajectory for re-entry . . . 43
3.17 Covariance ellipsoid . . . 45
3.18 Schematic view of a landing dispersion . . . 46
3.19 Landing dispersion and its contributors of the Mars Exploration Rover . . . 47

4.1 Concept of a controllable re-entry vehicle . . . 49
4.2 Weighting factor of the regularization term . . . 59
4.3 Controlled re-entry onto Earth I . . . 61
4.4 Controlled re-entry onto Mars I . . . 62
4.5 Controlled re-entry onto Earth II . . . 63
4.6 Controlled re-entry onto Mars II . . . 64
4.7 Absolute error of the optimized trajectories . . . 66
4.8 Most probable trajectory of optimized trajectories . . . 66
4.9 Evolution of the PDF for optimized re-entry trajectories . . . 67

5.1 Hypersonic Inflatable Aerodynamic Decelerator . . . 71

B.1 Controlled descent with larger box constraints . . . 80
B.2 Absolute error of the optimized re-entry trajectories . . . 81
B.3 Most probable trajectory of optimized trajectories . . . 81
B.4 Evolution of the PDF for optimized re-entry trajectories . . . 82

C.1 Descent onto Earth and Mars . . . 84
C.2 Re-Entry onto Earth and Mars with different atmosphere models . . . 85
C.3 Re-Entry onto Earth and Mars with different entry velocities . . . 86
C.4 Re-Entry for different parameter settings . . . 87
C.5 Controlled re-entry onto Earth I . . . 90
C.6 Controlled re-entry onto Mars I . . . 91
C.7 Controlled re-entry onto Earth II . . . 92
C.8 Controlled re-entry onto Mars II . . . 93

List of Tables

2.1 Mission examples for ballistic coefficients and lift-to-drag ratios 12
2.2 Descent times of re-entry for different entry velocities 15
2.3 Combination of parameters for different re-entry scenarios 16
2.4 Descent times of re-entry for different parameters 16

3.1 Dispersion at end time for the altitude during vertical flight 40
3.2 Dispersion at end time for the altitude during re-entry 41

4.1 Descent times for oscillating control 59
4.2 Descent times for smoothed control 60
4.3 Technical details of the optimization (three state) using TransWORHP . . . 60
4.4 Descent times of the set of optimized trajectories 65

5.1 Resulting 1-σ neighbourhood of Mars 70

A.1 Planetary facts of Earth and Mars 73
A.2 Atmosphere data of Earth 76
A.3 Atmosphere data of Mars 77

B.1 Descent times of controlled re-entry 79

C.1 Technical details of the optimization (six state) using TransWORHP 89

Nomenclature

Abbreviations

Institutions

DLR	German Aerospace Center
ESA	European Space Agency
NASA	National Aeronautics and Space Administration
ZeTeM	Center for Industrial Mathematics

Methods, Models and Terms

EAM	Earth Atmosphere Model
EDL	Entry, descent and landing
FPA	Flight path angle
HIAD	Hypersonic Inflatable Aerodynamic Decelerator
MAM	Mars Atmosphere Model
MC	Monte-Carlo Analysis
MOC	Method of Characteristics
MPT	Most probable trajectory
NLP	Nonlinear Program
OCP	Optimal Control Problem
ODE	Ordinary differential equation
PDE	Partial differential equation
PDF	Probability density function
SLE	Stochastic Liouville Equation
SQP	Sequential Quadratic Programming
US76	United States Standard Atmosphere 1976
VAA	Velocity azimuth angle

List of Symbols

Re-Entry Dynamics

$h : \mathbb{R} \to \mathbb{R}$	Altitude
$\theta : \mathbb{R} \to \mathbb{R}$	Longitude
$\phi : \mathbb{R} \to \mathbb{R}$	Latitude
$v : \mathbb{R} \to \mathbb{R}$	Velocity relative to planet
$\gamma : \mathbb{R} \to \mathbb{R}$	Flight path angle
$\psi : \mathbb{R} \to \mathbb{R}$	Velocity azimuth angle measured form North
$R_0 \in \mathbb{R}$	Radius of planet
$\rho : \mathbb{R} \to \mathbb{R}$	Atmospheric density or fluid density
$B_c \in \mathbb{R}$	Ballistic coefficient
$\frac{C_L}{C_D} \in \mathbb{R}$	Lift-to-drag ratio
$C_D \in \mathbb{R}$	Drag coefficient
$C_L \in \mathbb{R}$	Lift coefficient
$g : \mathbb{R} \to \mathbb{R}$	Acceleration due to gravity
$GM \in \mathbb{R}$	Gravitational constant of planet
$G \in \mathbb{R}$	Universal gravity constant
$m \in \mathbb{R}$	Mass
$\alpha \in \mathbb{R}$	Bank angle
$\omega \in \mathbb{R}$	Rotational angular velocity
$T : \mathbb{R} \to \mathbb{R}$	Temperature
$P : \mathbb{R} \to \mathbb{R}$	Atmospheric pressure
$q \in \mathbb{R}$	Dynamic pressure
$A \in \mathbb{R}$	Cross-sectional area
$F_L \in \mathbb{R}$	Lift force
$F_D \in \mathbb{R}$	Drag force
$F_g \in \mathbb{R}$	Gravitational force

Uncertainty Dispersion Analysis

$X,\ Y : \Omega \to \mathbb{R}$	Random variables
$n \in \mathbb{N}$	Number of random variables
$\Omega \subset \mathbb{R}$	Probability space
$P(x)$	Probability
$\mu \in \mathbb{R}$	Expected value
$\sigma \in \mathbb{R}$	Standard deviation
$C \in \mathbb{R}^{n \times n}$	Covariance Matrix
$\varphi_{\mu,\sigma} : \mathbb{R} \to \mathbb{R}$	Normal distribution
$\varphi_{\mu,C} : \mathbb{R}^n \to \mathbb{R}$	Multivariate Normal distribution
$x \in \mathbb{R}^{n_x}$	States/ state vector
$p \in \mathbb{R}^{n_p}$	Parameters/ parameter vector
$\tilde{x} \in \mathbb{R}^{n_x+n_p}$	Augmented state vector
$n_x \in \mathbb{N}$	Number of states
$n_p \in \mathbb{N}$	Number of parameters
$\varphi :\in \mathbb{R}^{n_x} \to \mathbb{R}$	Probability density function estimated from SLE
$\Psi : \mathbb{R}^n \to \mathbb{R}$	Trace of Jacobian
$t \in [t_0, t_f]$	Time axis
$t_0 \geq 0$	Start time
$t_f > 0$	End time
ε	Gathers normalisation condition of the PDF
$\Delta_\varepsilon > 0$	Absolute error of violation of normalisation condition

Optimisation and Optimal Control

$f : \mathbb{R}^n \to \mathbb{R}$	Objective function
$g : \mathbb{R}^{n_x} \to \mathbb{R}^m$	Equality and ineqality constraints
$m \in \mathbb{N}$	Number of constraints
$n_x \in \mathbb{N}$	Number of states
$\mathcal{A}$	Active Set
$\lambda \in \mathbb{R}^m$	Lagrange multipliers
$L : \mathbb{R}^{n \times m} \to \mathbb{R}$	Lagrange Function
$\mathcal{K}$	Critical Cone
$x \in \mathbb{R}^{n_x}$	States/ state vector
$u \in \mathbb{R}^{n_u}$	Controls/ control vector
$n_u \in \mathbb{N}$	Number of controls
$t \in [t_0, t_f]$	Time axis
$t_0 \geq 0$	Start time
$t_f > 0$	End time
$I(x, u)$	Objective or Cost functional
$\xi : \mathbb{R}^{n_x \times n_x} \to \mathbb{R}^r$	Boundary constraints
$r \in \mathbb{N}$	Number of boundary constraints
$\kappa > 0$	Weighting factor

Chapter 1

Introduction

1.1 Motivation

Atmospheric re-entry[1] is the most challenging phase of space exploration missions in consideration of the extremes the re-entry vehicle is exposed to. These extremes are characterized by heating due to friction with the atmosphere and great loads due to the hyper- and supersonic velocities during re-entry, descent and landing (EDL).
A safe and as accurate as possible re-entry is not only necessary when executing manned missions but it is also conceivable to have unmanned sample return capsules from other celestial bodies or the return of reusable spacecrafts which are becoming increasingly common. When thinking of the exploration of other planets e.g. Mars, an accurate re-entry is necessary to reach scientific interesting regions. To solve these re-entry problems and ensure a successfull mission along with a safe landing, the requirements on the vehicle need to be carefully balanced with respect to the mission objectives.

In figure 1.1 the re-entry, descent and landing procedure of the ExoMars Schiapirelli mission is presented [61]. As it can be seen, the last approximately 10km are executed by parachutes and descent thrusters. These mechanisms are not considered in this study. Nevertheless the most accuracy is needed during the entry into the planet's atmosphere and the atmospheric deceleration phase, see first two sequences in figure 1.1. During these phases, changes in the entry angle and the entry velocity have large influence on the trajectory of the re-entry vehicle. Therefore, it is necessary to predict the performance of the re-entry vehicle in presence of uncertainties. Before the actual mission the re-entry is analysed considering uncertainties in the initial conditions entry angle, altitude and velocity as well as uncertainties in the atmosphere model and the model of the vehicle to find a reliable set of entry angle, altitude and velocity.

[1] here re-entry also stands for entry into planetary atmospheres even if the vehicle or spacecraft is not returning to the planet (e.g. Earth)

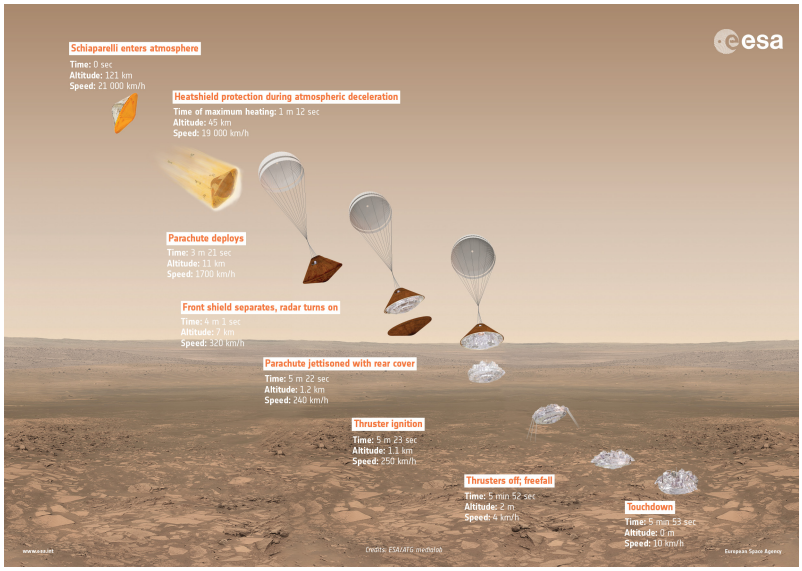

Figure 1.1: Re-entry, descent and landing of ExoMars Schiaparelli 2016 [61].

This can be done using a Monte-Carlo (MC) dispersion analysis. By this method, a large number of trajectories is simulated using a random sampled set of initial conditions and parameters. For high dimensional and nonlinear dynamics, as it is given by the re-entry problem, these simulations are computationally expensive. It is necessary to calculate uncertainties in a large number of states and parameters for each set of initial conditions [1]. Additionally the probability density functions need to be reconstucted from the resulting samples of the MC analysis.
An alternative approach analyses the time evolution of given dynamics with a given distribution of initial conditions and parameters resulting directly in probability density functions stating the proability over time of each state of the dynamics.

This method utilises the *Stochastic Liouville Equation* and is not only computationally attractive but also advantageous over the MC analysis, since from the directly resulting probability density functions all statistical moments can be derived. For example the covariance matrix, which in the specific case of atmospheric re-entry governs the landing dispersion. This landing dispersion provides information about the range across the landing site. In figure 1.2 estimated landing ellipses for the ExoMars 2018 and 2020 missions on one of the selected landing sites Mawrth Vallis are displayed [62].

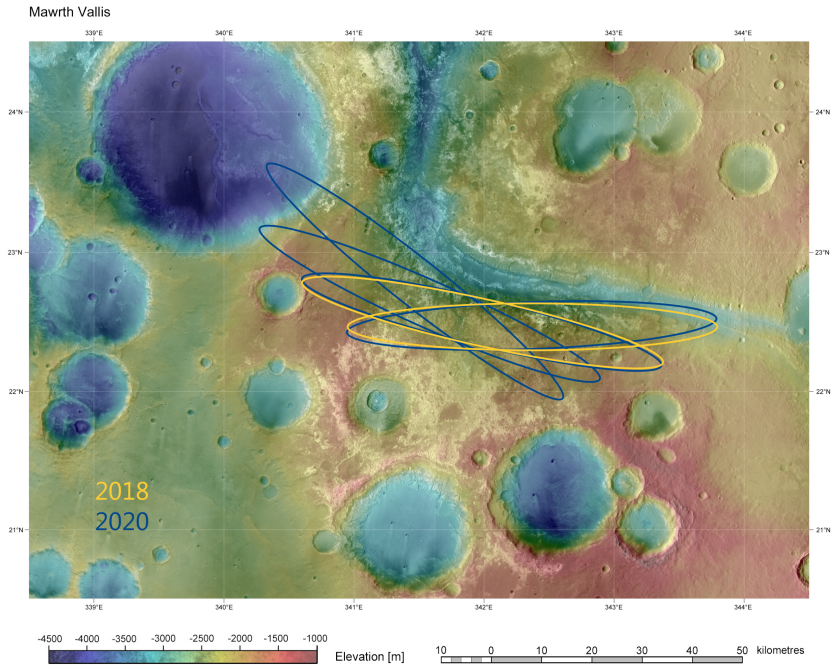

Figure 1.2: Landing ellipses of the ExoMars 2018 and 2020 missions on the possible landing site Mawrth Vallis on Mars [62].

1.2 Thesis Objective

In this study, an alternative for the Monte-Carlo (MC) dispersion analysis is presented which uses probability density functions to predict the temporal evolution of given re-entry dynamics in presence of uncertainties. Whereof covariance matrices in every time step during the re-entry can be estimated which for the last time step govern the landing dispersion. In addition, most probable re-entry trajectories are generated from the results of the uncertainty dispersion analysis.
Throughout this thesis, the re-entry onto Earth and Mars is considered for which ballistic and controlled trajectories are generated and analysed concerning uncertainties in the initial conditions.

1.3 Structure of this Thesis

In the first chapter the re-entry problem is laid out and explained in detail. Two models to simulate the re-entry onto a planet are introduced and first solutions for Earth and Mars are presented. The second chapter is dedicated to the uncertainty analysis which is based on the propagation of probability density functions. Therefore, the necessary fundamentals in stochastics are presented before the method to analyse the temporal evolution of uncertainties is derived. This method is used to analyse the re-entry onto Earth and Mars. Since usually a re-entry vehicle is manoeuvrable and can control for example its angle of

attack[2], a controlled re-entry is examined and optimal re-entry trajectories are generated in the next chapter. First the theory of optimization and optimal control is laid out. Afterwards optimal trajectories for re-entry onto Earth and Mars are presented. In the end the optimal control problem is analysed relating to uncertainty dispersion using the method developed in the previous chapter.
The thesis completes with final conclusions and remarks about the results of the uncertainty analysis. Additionally, possible future work is discussed.

[2] angle between the air flow and the body reference line

Chapter 2

The Re-Entry Problem

Atmospheric re-entry can be compared to the challenge of skipping stones on a lake. The shape of the stone, the angle in which it hits the surface of the lake and the velocity it was tossed with are important for a successful skip. Is the stone not flat enough and the impact angle too steep or it is tossed to fast, it won't skip of the surface and rather splash into the lake. The same holds for atmospheric re-entry. Thinking of the stone as the manned or unmanned re-entry vehicle the lake can be compared to the planet's atmosphere. At hypersonic velocities, the vehicle needs to hit the atmosphere at a precise angle and with a defined speed to ensure a safe landing. If the angle is too steep, the occurring forces will break the vehicle apart. On the contrary, a too shallow angle will make the vehicle skip off the atmosphere and back into space. [11]

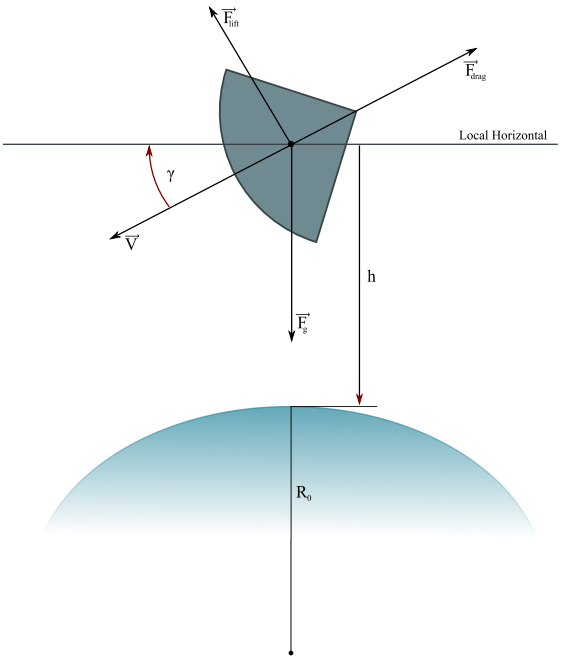

Figure 2.1: The re-entry scenario (adapted from [11]).

In figure 2.1 the re-entry scenario is presented schematically. The *flight path angle* γ (FPA) is the angle between the local horizon and the velocity vector. A negative angle implies that the vehicle is pointing towards the planet.
The main forces acting on the vehicle are the drag $\vec{F}_D$, lift $\vec{F}_L$ and gravity $\vec{F}_g$. The drag force acts in the opposite direction to the velocity and slows down the vehicle. The lift force is perpendicular to drag and velocity. The vehicle shape sets the aerodynamic attributes of the re-entry. These attributes are mainly described by the *ballistic coefficient* B_C and the *lift-to-drag ratio* $\frac{C_L}{C_D}$.
The ballistic coefficient B_C describes the ability of the vehicle to overcome air resistance. The higher the B_C the more streamlined the vehicle is. The lift-to-drag ratio $\frac{C_L}{C_D}$ estimates the amount of lift the vehicle generates. A low ratio characterises a vehicle which produces only a small amount of lift and a high value is given by vehicles producing a large amount of lift, e.g. airplanes or other winged vehicles.

These parameters are explained and the setting of the re-entry problem is laid out in more detail in the following sections. Starting with characteristic trajectories, the re-entry environment and the vehicle aerodynamics are discussed. These sections are based on [11, 12]. Afterwards the re-entry dynamics are summarised, which are taken from [3], and some trajectories are simulated for Earth as well as Mars with initial conditions based on [1, 2].

2.1 Trajectories

The trajectories a vehicle follows during entry into a planet's atmosphere depends on the vehicle's shape, its entry velocity and entry angle as well as its aerodynamic behaviour. The shapes of re-entry vehicles can be divided into two main types. The capsules, which were for example used in the Apollo, Gemini and Mercury missions, and the winged vehicles like the Space Shuttle. The first type is defined by its low lift-to-drag ratio ($\frac{C_L}{C_D} < 1$). On the contrary the winged vehicles have a high ratio ($\frac{C_L}{C_D} > 1$). Likewise the trajectory types can be categorised by the vehicle attributes and entry conditions.

The most simple but most drastic type of re-entry is the **ballistic entry** (see *a* in figure 2.2). It is defined by a short descent time and is performed by vehicles with a low lift-to-drag ratio $\frac{C_L}{C_D}$ like re-entry capsules, which are semi-ballistic since they produce a small amount of lift for aerodynamic controllability. During this entry, the vehicle enters the atmosphere at a high velocity and a steep angle, which remains almost constant throughout the entire descent. The drawback of this trajectory is the steep entry angle causing the vehicle to reach denser layers of the atmosphere at a high velocity leading to large gravitational forces and heating rates acting on the vehicle.

The second type of re-entry is the **gliding entry** (see *b* in figure 2.2) which is performed by winged vehicles with a high lift-to-drag ratio such as the Space Shuttle. The

vehicle enters at a constant shallow angle generating lift at thicker layers of the atmosphere producing a much longer descent time. The shallow angle leads to lower forces and heating rates due to a slower velocity in the denser atmosphere layers.

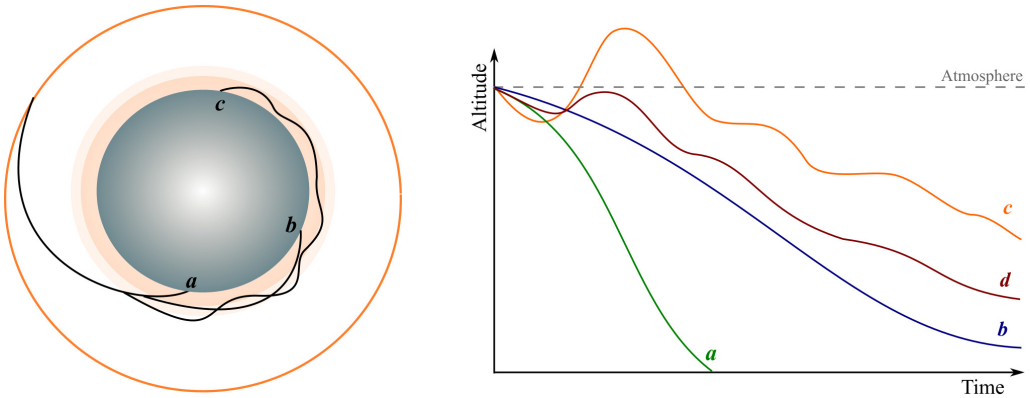

Figure 2.2: Schematic representation of the types of re-entry trajectories: *a*) ballistic entry, *b*) gliding entry, *c*) skipping entry, *d*) lofting entry (adapted from [12]).

The **skipping entry** (see *c* and *d* in figure 2.2) can be performed by both types of vehicles. This type is characterised by a not monotonically decreasing altitude. Therefore, the vehicle skips within or off of the atmosphere without added propulsive force increasing the descent range. Hereby the heating rate and acting forces are portioned into smaller periods than during ballistic entry.
When remaining inside the atmosphere the skips are called *lofts* (see *d* in figure 2.2).

Since not all vehicles can stand the same loads the designed trajectory needs to meet the mission requirements and constraints. Those requirements originate mainly from the payload itself, as it can be manned or unmanned, as well as the structural integrity of the vehicle defining the loads it can withstand. All these requirements and constraints can be converted to trajectory constraints leading to the concept of the **re-entry corridor** (see figure 2.3).

The corridor is defined by an overshoot and undershoot boundary. These boundaries set the limits where on the one hand the vehicle's entry angle is too shallow and it is deflected back into space (*overshoot*) or on the other hand the entry angle is too steep inducing too high loads on the vehicle (*undershoot*). Overall the re-entry corridor is described as the set of trajectories for which aerodynamic capture within the atmosphere can be achieved and for which re-entry trajectories control can be accomplished without violating either flight-crew or vehicle stress limits [12].

The size of this corridor depends on the constraints which stem from the vehicle design. In other words, it depends on the loads and heating rates the vehicle can withstand and directly reflects how sensitive the vehicle reacts to navigational errors. A narrow corridor stands for a small error margin since in this case only a small number of

trajectories lead to a successful re-entry. And correspondingly a wide re-entry corridor leads to a larger error margin. Therefore, a wide re-entry corridor is prefered. The size can be influenced by tackling the undershoot and overshoot boundaries. The boundaries depend on the maximum and minimum deceleration of the vehicle respectively which can be affected by the initial entry angle and entry velocity. But these parameters are predefined by the mission settings. The only parameter that can be influenced here is the ballistic coefficient B_C which directly influences the maximum heating rate of the vehicle. Thus, the corridor and consequently the error margin can only be enlarged by increasing the maximum heating rate and loads the vehicle can withstand.

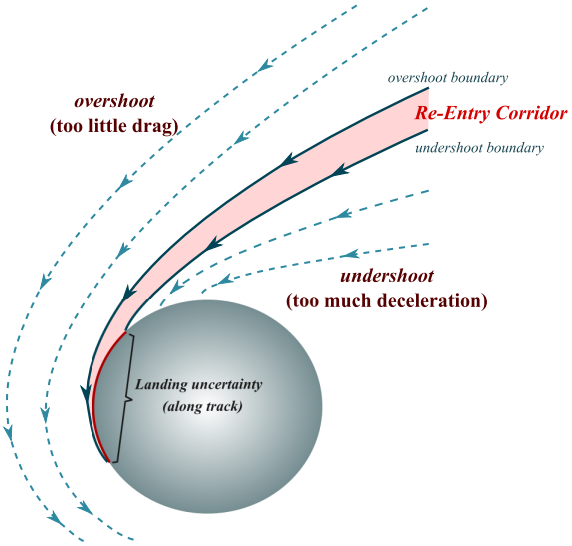

Figure 2.3: Re-Entry Corridor (adapted from [12, 11])

2.2 Environment Modelling

The environmental conditions are defining for a successful landing on celestial bodies since the environment defines the loads the vehicle is subjected to. These loads are crucial for the vehicles motion. Defining for the environment are the atmosphere, the gravitational field and the shape of the body on which the landing takes place [12].

Here main focus is placed on the atmospheres and the gravitational fields of Earth and Mars. Even if the shape of these planets is not a perfect sphere the specific shape is neglected and assumed to be spherical.

2.2.1 Gravity

Gravity is the force that draws the vehicle towards the planet during re-entry. According to Newton's law of gravitation two point masses separated by a distance r exert an attractive force on each other

$$F(r) = G\frac{mM}{r^2}, \tag{2.1}$$

where $G = 6.672591 \cdot 10^{-11} \frac{\mathrm{m}^3\,\mathrm{kg}}{\mathrm{s}^2}$ is the universal gravity constant, M and m are the masses of the bodies.
To calculate the gravitational field and accordingly the acceleration due to gravity the equation in (2.1) is set equal to the elementary formula of the weight force depending on the gravitational acceleration g of the planet and the mass m of a body the force is acting on. From this follows a formula for the gravitational field of a planet depending on the gravitational constant denoted by GM (see table A.1 in appendix A.1) and the distance r from the body.

$$F = mg = G\frac{mM}{r^2} \tag{2.2}$$

$$\Rightarrow g = \frac{GM}{r^2} = \frac{GM}{(R_0 + h)^2} \tag{2.3}$$

To calculate the gravitational acceleration depending on the altitude of the re-entry vehicle r is replaced with $r = R_0 + h$. In this case R_0 represents the radius of the corresponding planet and h the altitude above the planet.

In figure 2.4 the acceleration due to gravity of Earth and Mars is presented as a function of the altitude h. The gravity on the surface of Mars is about one third of the gravity on the surface of Earth.

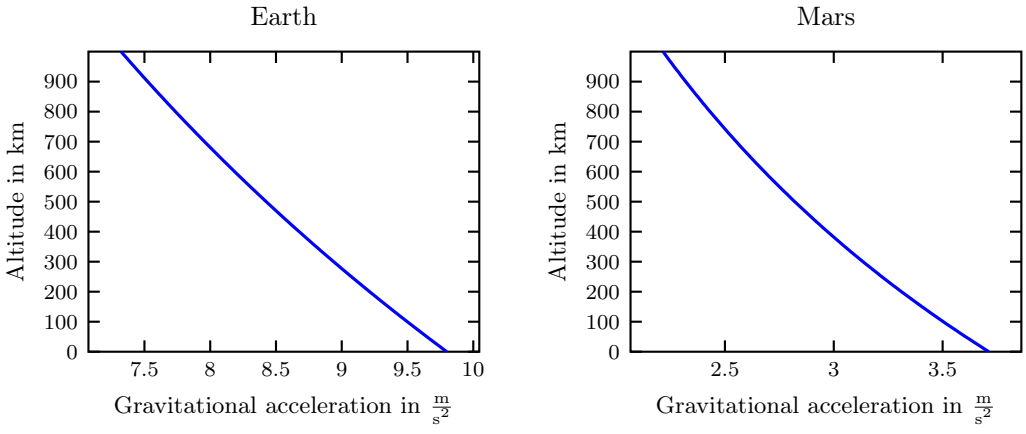

Figure 2.4: Gravitational field of Earth and Mars as a function of altitude h.

2.2.2 Atmosphere

The difference between landing on an asteroid or comet and landing on a planet is the presence of an atmosphere. Due to this thin layer of gas, the re-entry vehicle experiences the aerodynamic forces lift and drag which cause it to decelerate or lift even higher as well as aerodynamic heating caused by friction with the atmosphere. These aspects are critical for a successful mission and need to be known over the whole trajectory. Therefore, an atmospheric model is used to determine the aerodynamic forces acting on the vehicle.

The dependent properties of the atmosphere, temperature and pressure, change over time and altitude due to solar activity throughout the day. These changes are difficult to model. All atmosphere models regardless of which planet are very complex and only approximations. For the re-entry dynamics in section 2.4 the density ρ in dependence of the altitude h is taken into account since the density is influencing the aerodynamic drag and correspondingly the deceleration of the vehicle. In figure 2.5 three different atmosphere density profiles of Earth and Mars are shown respectively.
The models used in this thesis for Earth are the US Standard Atmosphere from 1976 (US76), the MSISE-00 empirical model and the Earth Atmospheric Model (EAM) by NASA Glenn Research Centre given in A.2. For Mars the model established by Noton in [19], the Mars Atmospheric Model (MAM) by NASA Glenn Research Centre and the Mars Global Reference Atmospheric Model (GRAM) also given in A.2 are used.

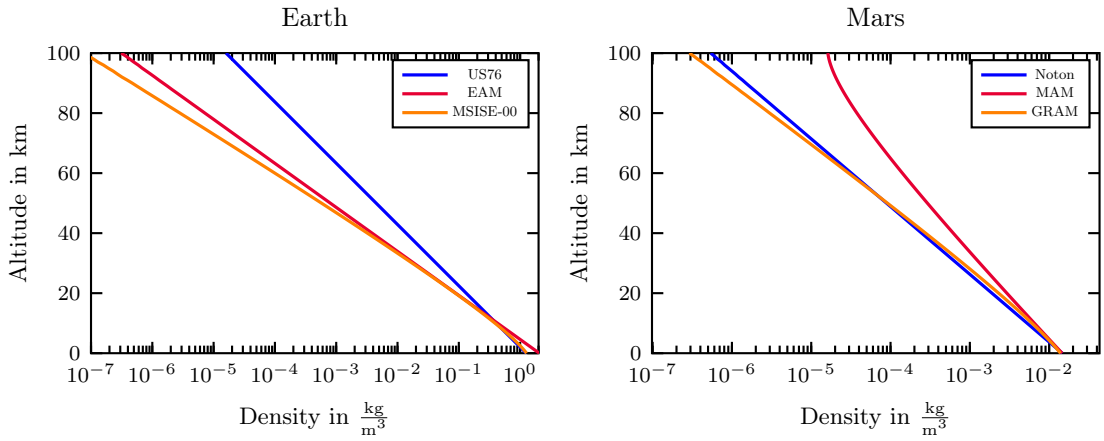

Figure 2.5: Comparison of different Earth and Mars Atmosphere Models with a logarithmic x-axis

The atmosphere of Earth consists of nitrogen and oxygen and can be devided into three layers (troposphere, stratosphere and mesosphere). In comparison, the atmosphere of Mars is much thinner, consists mainly of carbon dioxide and can be seperated into two layers [49]. This difference leads to a different number of aerodynamic loads whether the vehicle is entering the atmosphere of Mars or Earth.

2.3 Aerodynamics

In re-entry trajectory design the variable parameters besides the initial conditions are the vehicle parameters: *ballistic coefficient* B_C and *lift-to-drag ratio* $\frac{C_L}{C_D}$. These aerodynamic characteristics depend on the vehicles shape and size, the air conditions and the flight velocity.

Ballistic Coefficient

The ballistic coefficient characterises the intensity of a vehicle's deceleration due to drag of the atmosphere. This property depends on the mass m and the cross-sectional area A and the drag coefficient C_D of the vehicle.

$$B_c = \frac{m}{C_D A} \tag{2.4}$$

The drag coefficient C_D is a dimensionless measure for drag or flow resistance of objects in fluid flow. It depends on the cross-sectional area A, the density ρ, the velocity v of the fluid and the drag force F_D.

$$C_D = \frac{F_D}{\frac{1}{2}\rho A v^2} = \frac{D}{qA}, \tag{2.5}$$

In most cases this value is measured in wind tunnels using a vehicle model or approximated with numerical flow simulation.

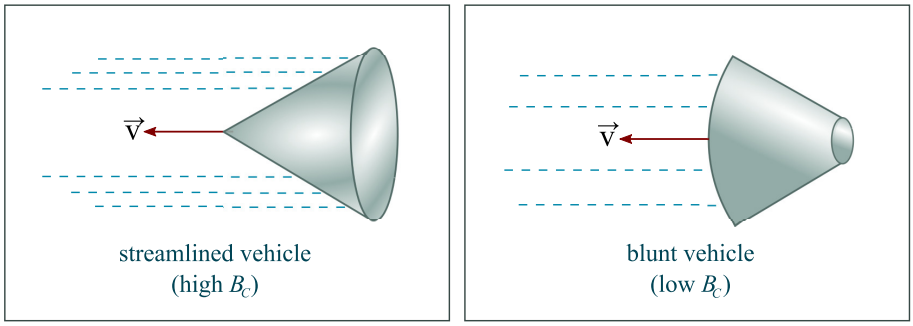

Figure 2.6: Ballistic Coefficient (adapted from [11]).

The ballistic coefficient varies with the vehicle shape and the entry angle. A blunt vehicle has a lower B_C than a more streamlined vehicle (see figure 2.6). The streamlined vehicle will reach the ground faster than the blunted one and it will experience its maximum deceleration much lower in the atmosphere [11].

Lift-to-Drag Ratio

The ratio between lift and drag is an indication for the aerodynamic efficiency of a vehicle. The drag force is oriented along the flight path but contrary to the direction of motion and the lift force is perpendicular to it [56], see figure 2.1.

The lift coefficient characterises the amount of lift a vehicle can generate in a fluid medium. As well as the drag coefficient C_D it depends on the cross-sectional area A, the density ρ and the velocity v of the fluid. But in contrast to the drag coefficient C_D the lift coefficient depends on the lift force F_L.

$$C_L = \frac{F_L}{\frac{1}{2}\rho v^2 A} = \frac{F_L}{qA} \tag{2.6}$$

Similar to the drag coefficient the lift coefficient is usually measured in wind tunnel experiments or approximated from numerical flow simulations.
The lift coefficient divided by the drag coefficient is the lift-to-drag ratio. The higher the ratio the greater the distance a vehicle can travel across the ground.

$$\frac{C_L}{C_D} = \frac{F_L}{F_D} \tag{2.7}$$

A ratio $\frac{C_L}{C_D} < 1$ is characteristic for low lift vehicles like capsules while a ratio $\frac{C_L}{C_D} > 1$ is typical for high lift vehicles like planes or the Space Shuttle. As an overview some examples for the aerodynamic coefficients accompanied by the corresponding missions are given in the following table 2.1. For example, an airplane possesses a high amount of lift but only a small amount of drag which results in a high lift-to-drag ratio. The higher the amount of drag a vehicle produces the smaller the lift-to-drag ratio and vice-versa.

	B_C [kg/m^2]	$\frac{C_L}{C_D}$
Capsules		
Small unmanned	72.8	0.3
Apollo	280	0.3
Mercury	268.44	N/A
Winged		
Space Shuttle (hypersonic phase)	432.1	1.0
Space Shuttle (approach)	432.1	4.5

Table 2.1: Mission examples for ballistic coefficient and lift-to-drag ratios (from [13, 19])

In figure 2.7 the correlation of the ballistic coefficient and the lift-to-drag ratio and the shapes of the re-entry vehicles is shown.

Aside from lift and drag another load acting on the vehicle during re-entry is the heating due to friction between the vehicle and the atmosphere. The heating is also critical for the mission but this aspect is not part of the thesis work and is not dealt with further.

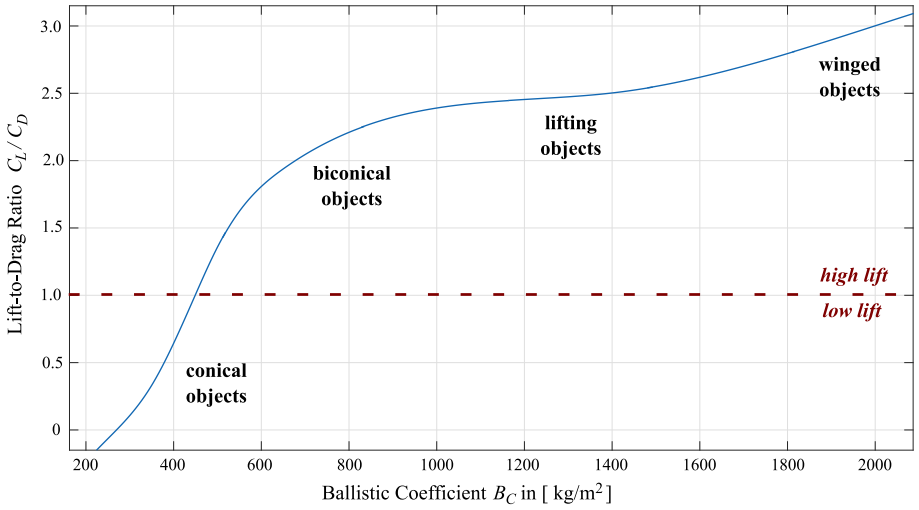

Figure 2.7: Lift-to-drag ratio compared to the ballistic coefficient denoted with corresponding vehicle shapes (adapted from [14]).

2.4 Re-Entry Dynamics

All the above discussed aspects of re-entry are modelled in the re-entry dynamics. The dynamics used in this thesis are taken from [1, 3]. Two models will be presented: a three state and a six state model. Main focus is placed on the three state model. For simulation results of the six state model refer to appendix C.
The presented models govern the trajectory of the centre-of-mass of a non-thrusting, lifting vehicle entering a planetary atmosphere and are solved using the `ode23` solver of MATLAB.

2.4.1 Three State Model

The three state model presents the simplified scenario given in figure 2.1. In this case, the vehicle's trajectory is contained in the longitudinal plane and is described by the variables altitude h, velocity v and flight path angle γ.

$$\begin{aligned} \dot{h} &= v \sin\gamma \\ \dot{v} &= -\frac{\rho}{2B_c} v^2 - g \sin\gamma \\ \dot{\gamma} &= \frac{\rho}{2B_c}\frac{C_L}{C_D} v + \cos\gamma \left(\frac{v}{R_0 + h} - \frac{g}{v} \right) \end{aligned} \tag{2.8}$$

where g as in (2.2) and ρ is the atmosphere model as described in 2.2.2. In this model, the bank angle is set to zero and the rotation of the planet is neglected.

For a descent on celestial bodies without atmosphere the dynamics of the three

state model can be reduced to

$$\begin{aligned} \dot{h} &= v \sin\gamma \\ \dot{v} &= -g \sin\gamma \\ \dot{\gamma} &= \cos\gamma \left(\frac{v}{R_0 + h} - \frac{g}{v} \right) \end{aligned} \tag{2.9}$$

where $\rho(h) = 0$. In this case only the gravity is the operating force drawing the re-entry vehicle towards the planet. In figure 2.8 the descent onto Earth and Mars without lift and drag of the atmosphere is shown exemplarily. The initial values for the states were set as

$$\begin{aligned} h_0 &= 80\text{km} \\ v_0 &= 3.5 \frac{\text{km}}{\text{s}} \\ \gamma_0 &= -2^\circ = -0.0349\text{rad} \end{aligned} \tag{2.10}$$

The radiuses of Earth and Mars are taken as stated in table A.1.

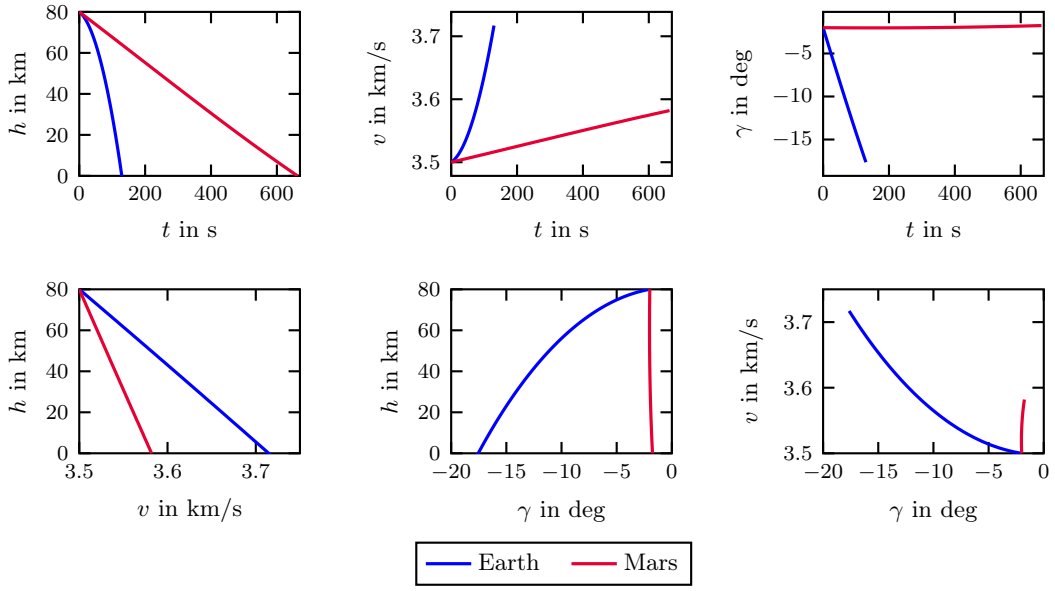

Figure 2.8: Descent onto Earth and Mars without consideration of the atmospheres.

Due to the higher mass and planetary radius of Earth and thus the higher gravity (see figure 2.4) compared to Mars, the vehicle hits the ground with a higher velocity and after a shorter amount of time. The velocity of the vehicle increases since no aerodynamic forces interfere and thus it is not decelerating.
This changes when the atmosphere is considered. In this case, the aerodynamic parameters are set as

$$\begin{aligned} B_C &= 78.2 \frac{\text{kg}}{\text{m}^2} \\ \frac{C_L}{C_D} &= 0.3 \end{aligned} \tag{2.11}$$

The initial conditions for the entry altitude h_0, the entry velocity v_0 and the entry angle γ_0 are the same as given in (2.10). For modelling the atmosphere the models mentioned in section 2.2.2 are used. In figure 2.9 the entry trajectories for each atmosphere model are presented for Earth and Mars, respectively.

Compared to the descent without atmosphere the re-entry takes much longer due to the aerodynamic loads. Also, the velocity is decreasing with time. In case of re-entry onto Earth the vehicle is decelerating faster and earlier than the vehicle re-entering onto Mars as a result of the much denser atmosphere. For Mars, it is noticeable that for every state the trajectory utilising the atmosphere model by Noton is almost congruent with the one using GRAM.

In figure 2.10 the re-entry into Earth and Mars atmosphere is shown respectively. Additionally the initial velocity is varied for the values $v_0 \in \{3.0\frac{\text{km}}{\text{s}},\ 3.5\frac{\text{km}}{\text{s}},\ 4.0\frac{\text{km}}{\text{s}}\}$. In this case for Mars the atmosphere model developed by Noton [19], see (A.5), and for Earth the EAM from NASA Glenn Research Center, see (A.1), is used to model the atmosphere.

In case of re-entry onto Earth it is noticeable that for any of the three different initial velocities the trajectories do not change much. In addition, the descent times t_f are also almost the same, see table 2.2. Regarding the entry into Mars' atmosphere the different initial velocities have a high impact on the trajectory. On the one hand the descent time varies with the different velocities more recognisable than in case of Earth, see table 2.2. But even more striking: at the entry velocity of $v_0 = 4.0\frac{\text{km}}{\text{s}}$ the altitude is first decreasing until about 72km and then increasing again. This means that the vehicle bounces of off the atmosphere and travels back into space. With this entry velocity and the aerodynamic parameters as in (2.11) the vehicle overshoots and violates the upper boundary of the re-entry corridor.

		v_0 in km/s		
		3.0	3.5	4.0
Earth	t_f	612s	630s	648s
Mars	t_f	580s	824s	-

Table 2.2: Descent times of re-entry onto Earth and Mars for different entry velocities.

When varying the entry velocity, it is also possible to vary the aerodynamic properties the lift-to-drag ratio and the ballistic coefficient. These coefficients have an even larger impact on the re-entry trajectory. The initial values for h, v and γ are the same as given in (2.10). The parameters are set as the combinations in table 2.3. Combinations I, II and III, IV are typical for capsules and winged vehicles respectively. In cases I and III the vehicles are unmanned and correspondingly in cases II and IV the vehicles are manned. These values are taken from [19, 13].

This combination of initial values and parameters results in two different types of

	I	II	III	IV
B_C [kg/m^2]	72.8	280	72.8	280
C_L/C_D	0.3	0.3	1.0	1.0

Table 2.3: Combinations of ballistic coefficient B_C and lift-to-drag ratio $\frac{C_L}{C_D}$ for different re-entry scenarios.

re-entry trajectories. Concerning a ratio $\frac{C_L}{C_D} = 1.0$ the re-entry leads to skipping or lofting trajectories in case of Mars as well as Earth, for $\frac{C_L}{C_D} = 0.3$ the re-entry leads to ballistic trajectories, where the altitude decreases over time. Consequently also the descent times depend on the combination of parameters as stated in table 2.4. It can be recognised that for Earth the descent times are wide spread. But for Mars the trajectories can be clearly separated between the ones with $\frac{C_L}{C_D} = 1.0$ and $\frac{C_L}{C_D} = 0.3$ depending on the descent time.

		I	II	III	IV
Earth	t_f	630s	399s	1154s	782s
Mars	t_f	824s	838s	2220s	2205s

Table 2.4: Descent times of re-entry onto Earth and Mars for different aerodynamic properties B_C and $\frac{C_L}{C_D}$.

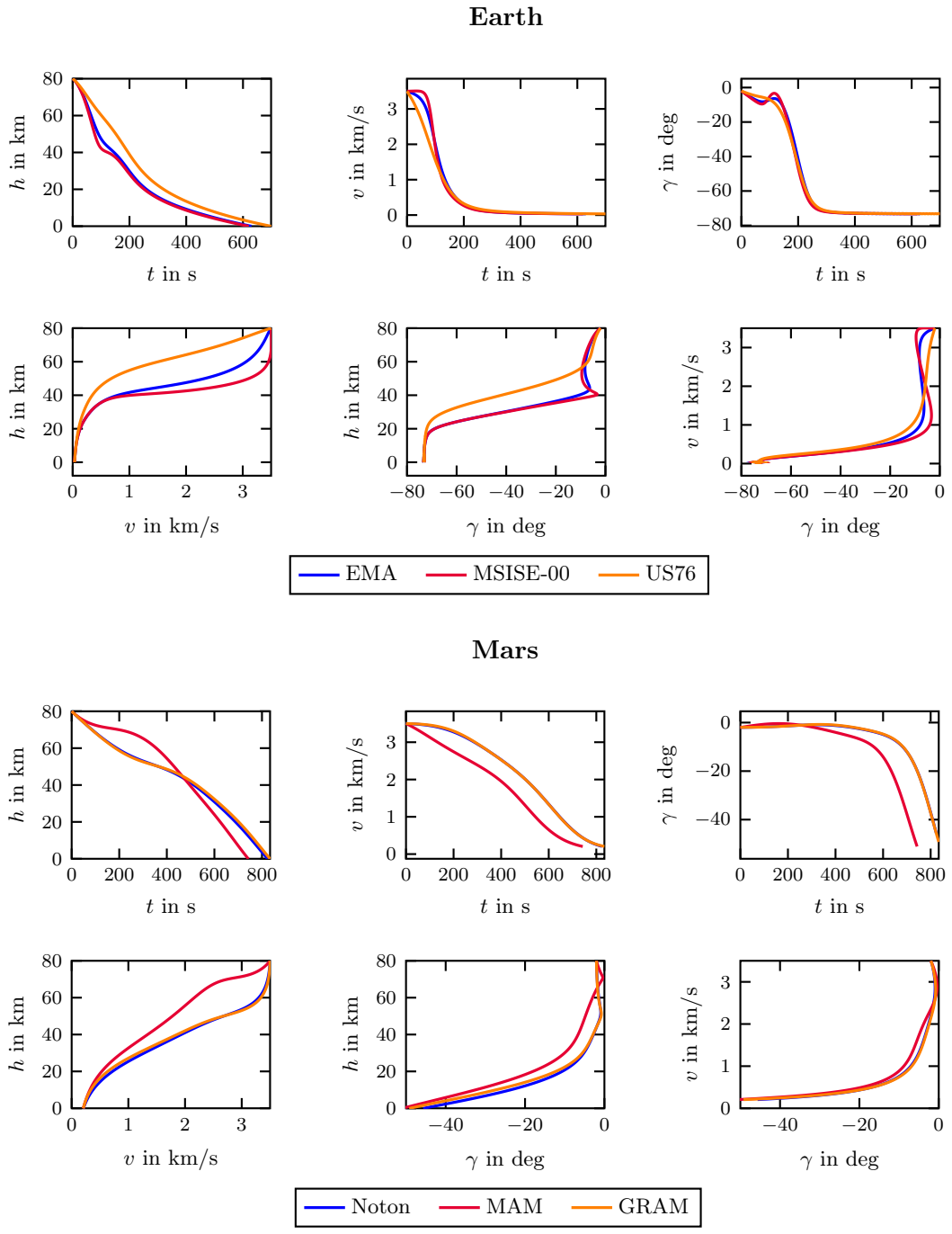

Figure 2.9: Re-Entry onto Earth (top) and Mars (bottom). For each three different atmosphere models are used with the initial conditions $h_0 = 80\text{km}$, $v_0 = 3.5\frac{\text{km}}{\text{s}}$ and $\gamma_0 = -2°$. The parameters are set as $B_C = 72.8\frac{\text{kg}}{\text{m}^2}$ and $\frac{C_L}{C_D} = 0.3$.

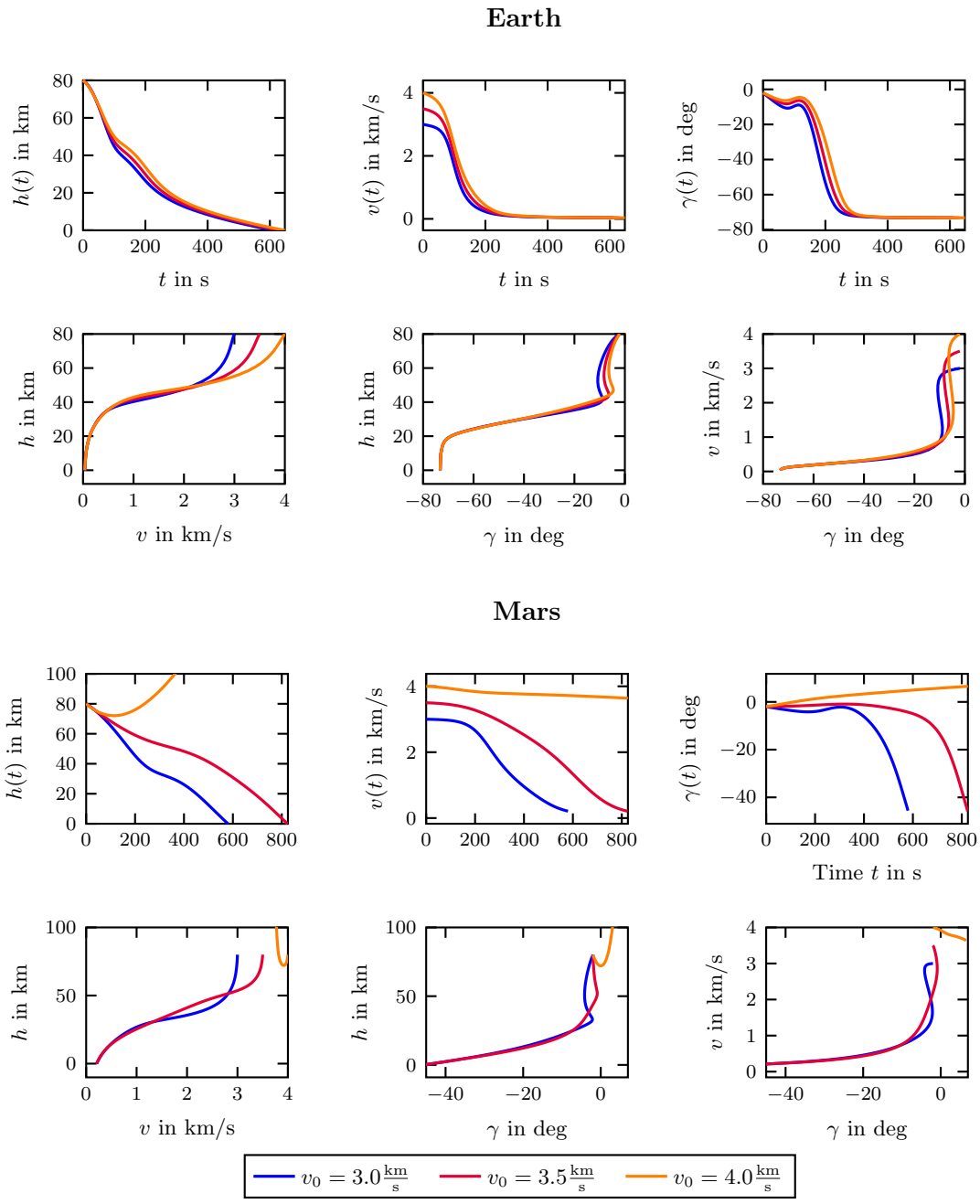

Figure 2.10: Re-Entry onto Earth (top) and Mars (bottom) at different entry velocities. For Earth the Earth Atmosphere Model (EAM) by NASA and for Mars the model established by Noton is used. The remaining initial conditions are set as $h_0 = 80\text{km}$ and $\gamma_0 = -2°$. The parameters are set as $B_C = 72.8\frac{\text{kg}}{\text{m}^2}$ and $\frac{C_L}{C_D} = 0.3$.

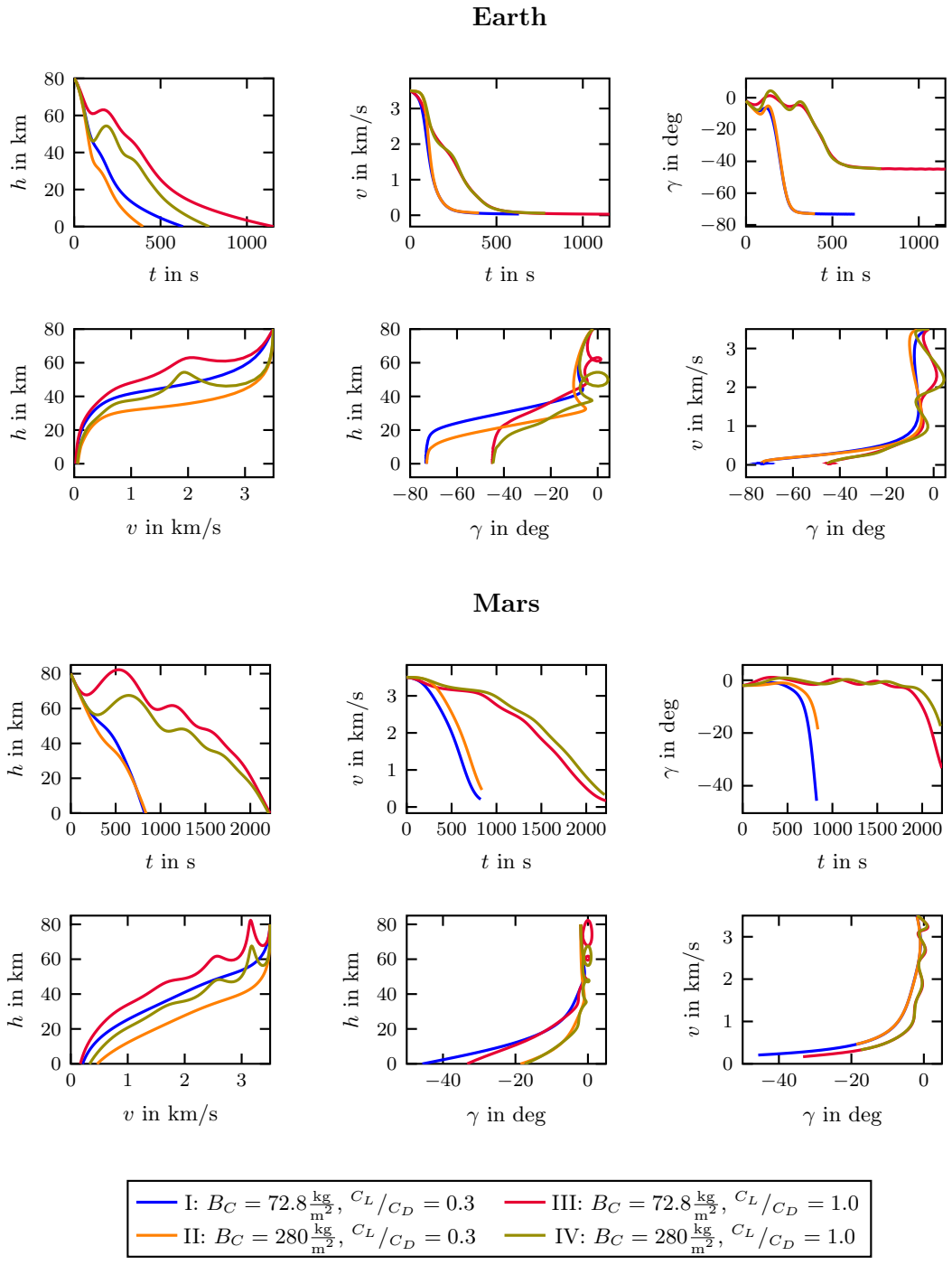

Figure 2.11: Re-Entry onto Earth (top) and Mars (bottom) for different B_C and $\frac{C_L}{C_D}$ combinations. For Earth the Earth Atmosphere Model (EAM) by NASA and for Mars the model established by Noton is used. Again the initial conditions are set as $h_0 = 80\text{km}$, $v_0 = 3.5\frac{\text{km}}{\text{s}}$ and $\gamma_0 = -2°$.

2.4.2 Six State Model

With the six state model the rotation of the planet and a possible bank angle of the vehicle are considered. In addition to the states (h, v, γ) the longitude θ, latitude ϕ and velocity azimuth angle (VAA) ψ of the vehicle are included in the differential equations, see figure 2.12.

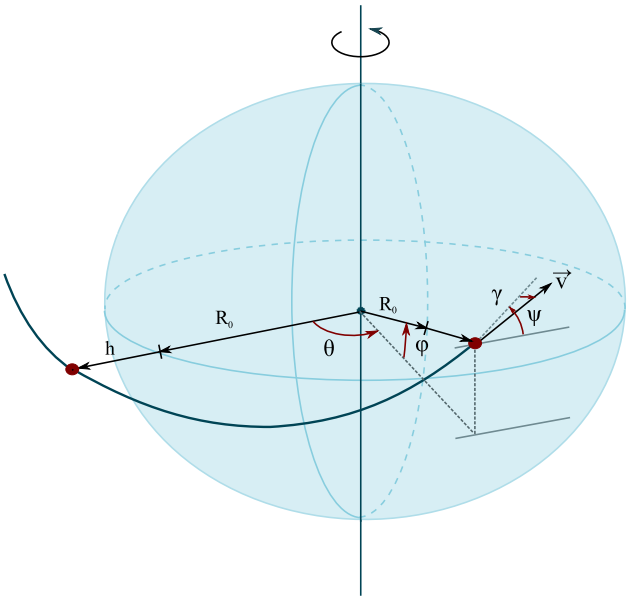

Figure 2.12: The re-entry scenario of the six state model considering the planetary rotation (adapted from [3]).

The flight path angle γ is measured positive when pointing upward from the local horizon (see also figure 2.1). The azimuth angle ψ of the velocity is measured positive towards North. The bank angle is taken such that the vehicle is turning to the left for a positive angle [3].

$$
\begin{aligned}
\dot{h} &= v \sin\gamma, \\
\dot{\theta} &= \frac{v \cos\gamma \cos\psi}{(R_0 + h)\cos\phi}, \\
\dot{\phi} &= \frac{v \cos\gamma \sin\psi}{(R_0 + h)}, \\
\dot{v} &= -\frac{\rho}{2B_c} v^2 - g \sin\gamma + \omega^2 (R_0 + h)\cos\phi(\sin\gamma\cos\phi - \cos\gamma\sin\phi\sin\psi), \\
\dot{\gamma} &= \frac{\rho}{2B_c}\frac{C_L}{C_D} v \cos(\alpha) + \cos\gamma\left(\frac{v}{R_0 + h} - \frac{g}{v}\right), \\
\dot{\psi} &= \frac{\rho}{2B_c}\frac{C_L}{C_D}\frac{v\sin\alpha}{\cos\gamma} - \frac{v\cos\gamma}{R_0 + h}\tan\phi\cos\psi + 2\omega(\tan\gamma\cos\phi\sin\psi - \sin\phi) \\
&\quad - \frac{\omega^2 (R_0 + h)}{v\cos\gamma}\sin\phi\cos\phi\cos\psi,
\end{aligned}
\tag{2.12}
$$

where α is the bank angle and ω is the rotational angular velocity of the planet (see table A.1). The first three equations describe the kinematic relations and the remaining equations display the momentums [3]. The terms in connection with ω in the equations $\dot{v}$ and $\dot{\psi}$ model the planetary rotation.

At this point the six state model is not examined further. For simulation results of the re-entry onto Earth and Mars in course of the six state model refer to appendix C.

Chapter 3

Uncertainty Dispersion Analysis

To ensure a safe and reliable entry, descent and landing (EDL) of a re-entry vehicle one must predict the system performance in presence of uncertainties. These uncertainties thrive from navigational errors, inaccurately predicted aerodynamic parameters as well as the approximated atmosphere model, which lead to off-nominal trajectories during the mission. Instead of simulating thousands of trajectories with random initial conditions as it is done for the Monte-Carlo (MC) analysis, this study outlines methods to investigate how a given distribution of initial conditions and parameters evolve over time. An advantage of this method is that all statistical moments can be derived from the probability density. [1]

First the necessary stochastical terms based on [22, 23, 24] are defined. Afterwards the method to analyse the uncertainty dispersion of a dynamic system is deduced as established in [1, 2, 6, 7]. In the end the three state model is analysed and the procedure to derive the landing dispersion based on the covariance matrix [4, 5] is laid out.

3.1 Fundamentals of Stochastics

The following explanations and definitions shall give an overview and understanding of the stochastical terms used in the upcoming sections.

Probability theory and statistics compose the mathematical domain of stochastics, which main subjects are occasional events and stochastic processes. This domain encompasses the description of coincidental occasions and their modelling. These occasions can arise discrete as in gambling like lottery or while tossing a dice. In contrast, the continuous occasions can be found in the natural sciences, for example fluctuations of the temperature in the course of a day in the lower atmosphere of Earth.

All stochastic processes are based on so-called random variables.

Definition 3.1 (Random Variable) *Let Ω be a probability space, so that every mapping $X : \Omega \to \mathbb{R}$ is called a* random variable *on Ω.*

A random variable is a function that maps possible outcomes x to a specific value. Each outcome has a specific probability by which it occurs.

Definition 3.2 (Probability) *The* probability *of an outcome $x \in \Omega$ is a function on the probability space Ω, denoted by $P(x)$ and holds the conditions*

(i) $P(\Omega) = 1$,

(ii) $0 \leq P(x) \leq 1$,

(iii) $P\left(\sum_{i=1}^{n} x_i\right) = \sum_{i=1}^{n} P(x_i)$, *if* $x_1, \ldots, x_n$ *pairwise disjoint,* $x_i \in \Omega$.

For a random variable X the expected value states the average value of all possible outcomes x_i weighted with the associated probabilities $P(x_i)$.

Definition 3.3 (Expected Value) *For a random variable $X : \Omega \to \mathbb{R},\ \Omega \subset \mathbb{R}$ and the probability P*

$$E(X) := \sum_{i \in \Omega} x_i \cdot P(x_i) = \mu \tag{3.1}$$

is the expected value *for a discrete random variable X.*

Based on the expected value it is possible to calculate the variance of a random variable.

Definition 3.4 (Variance and Standard Deviation) *The* variance *of a random variable $X : \Omega \to \mathbb{R},\ \Omega \subset \mathbb{R}$ is calculated from the expected value* (3.1)

$$Var(X) = V(X) := E(X - E(X))^2, \tag{3.2}$$

which can also be written as $\sigma^2(X)$.
The standard deviation *is the positive square root of the variance*

$$\sigma(X) := \sqrt{V(X)}. \tag{3.3}$$

The variance is a measure of the intensity of the dispersion around the expected value of a random variable. In case of two random variables X and Y the covariance is a measure for the relation between these random variables.

Definition 3.5 (Covariance) *The* covariance *of two random variables X and Y is given as*

$$Cov(X, Y) := E((X - E(Y)) \cdot (Y - E(Y))) \tag{3.4}$$

It states if a greater value for the random variable X goes along with greater values of Y or on the contrary goes along with smaller values of Y.
The covariance of a random vector $X = (X_1, \ldots, X_n)^\top$ can be written as a covariance matrix.

Definition 3.6 (Covariance Matrix) *For a random vector $X : \Omega \to \mathbb{R}^n$ the covariance matrix is given as*

$$C(\boldsymbol{X}) = \begin{pmatrix} Cov(X_1, X_1) & Cov(X_1, X_2) & \dots & Cov(X_1, X_n) \\ Cov(X_2, X_1) & Cov(X_2, X_3) & \dots & Cov(X_2, X_n) \\ \vdots & \vdots & \ddots & \vdots \\ Cov(X_n, X_1) & Cov(X_n, X_2) & \dots & Cov(X_n, X_n) \end{pmatrix}, \tag{3.5}$$

where $Cov(X_i, X_i) = Var(X_i)$ for $i = 1, \dots, n$.
This matrix is positive definite and symmetrical.

On the main diagonal, the variances of each random variable are given.

All the above explanations hold for discrete random variables. With the probability density function the probability dispersion of a continuous random variable is displayed.

Definition 3.7 (Probability Density Function (PDF)) *The function $f : \mathbb{R} \to \mathbb{R}$ is a* probability density function *for a continuous random variable X if*

(i) f is not negative, $f \geq 0 \ \forall x \in \mathbb{R}$

(ii) f is integrable

(iii) f is normalised, so that holds $\int_{-\infty}^{\infty} f(x)\,dx = 1$ (normalization condition)

The probability density function is defined by the probability

$$P(X \in [a, b]) := \int_a^b f(x)\,dx. \tag{3.6}$$

For continuous random variables, the expected value and the variance can be estimated from a PDF.

Definition 3.8 (Expected Value) *For a continuous random variable X and a probability density function f*

$$E(X) = \int_{-\infty}^{\infty} x f(x)\,dx = \mu \tag{3.7}$$

is the expected value.

Likewise, for a discrete random variable the variance follows from the expected value.

Definition 3.9 (Variance) *For a continuous random variable X and a probability density function f*

$$Var(X) = E((X - \mu)^2) = \int_{-\infty}^{\infty} (x - \mu)^2 f(x)\,dx \tag{3.8}$$

or alternatively by displacement law

$$Var(X) = E(X^2) - E(X)^2 = \int_{-\infty}^{\infty} x^2 f(x)\, dx - \mu^2 \tag{3.9}$$

is the variance.

A common continuous probability distribution is the normal or gaussian distribution. In statistics, this distribution is often used to model real-valued random variables with unknown distributions in natural or social sciences. The probability density of the normal distribution is given as

Definition 3.10 (Probability Density of the Normal Distribution) *The random variable* $X : \Omega \to \mathbb{R}$ *possesses the* normal distribution *with parameters* μ *and* σ^2*, if* x *has the density*

$$\varphi_{\mu,\sigma}(x) = \frac{1}{\sigma\sqrt{2\pi}} \cdot \exp\left(-\frac{(x-\mu)^2}{2\sigma^2}\right). \tag{3.10}$$

It is denoted with $X \sim \mathcal{N}(\mu; \sigma^2)$.

In figure 3.1 the normal distributions for different expected values and variances are displayed. A larger value of the variance yields a wider spread normal distribution.

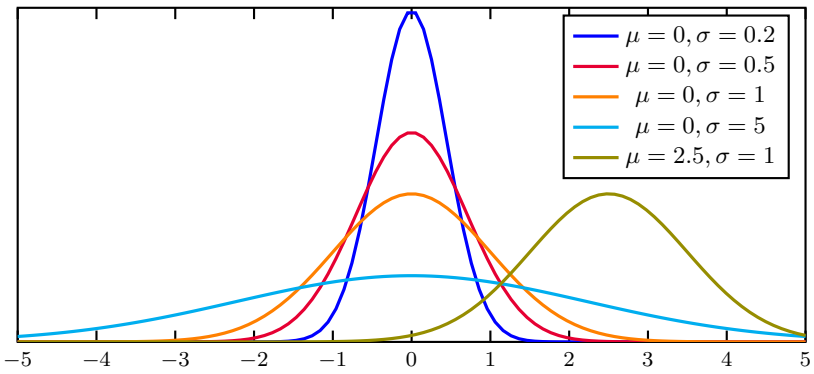

Figure 3.1: Density function of the normal distribution $\mathcal{N}(\mu; \sigma^2)$ for different expected values μ and standard deviations σ

The 1-, 2-, or 3-σ neighbourhood around the mean value μ denotes that the random variable reaches a specific value with 68%, 95% or 99% probability, see figure 3.2, this is also called the 3-sigma-rule.

In case of a n-dimensional random vector the normal distribution can be extended to a multivariate normal distribution depending on the vectorial expected value and the $n \times n$-dimensional covariance matrix.

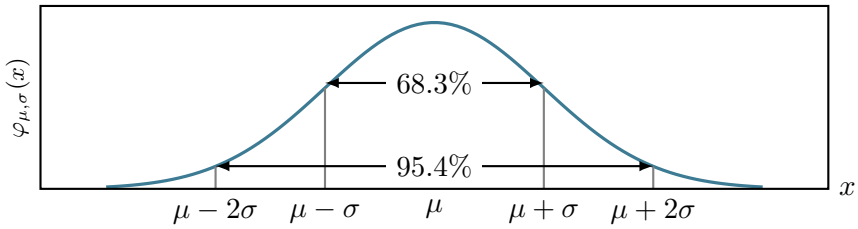

Figure 3.2: Density function of the normal distribution and 1- and 2-σ neighbourhood around the mean value μ.

Definition 3.11 (Probability Density of the Multivariate Normal Distribution) *A n-dimensional real random vector $X : \Omega \to \mathbb{R}^n$ is normal distributed with the expected value $\mu \in \mathbb{R}^n$ and the positive definite and symmetric covariance matrix $C \in \mathbb{R}^{n \times n}$, if the variable holds a density function of the form*

$$\varphi_{\mu,C}(x) = \frac{1}{\sqrt{(2\pi)^n det(C)}} \exp\left(-\frac{1}{2}(x-\mu)^\top C^{-1}(x-\mu)\right). \tag{3.11}$$

This multivariate distribution *is denoted with* $X \sim \mathcal{N}_n(\mu; C)$.

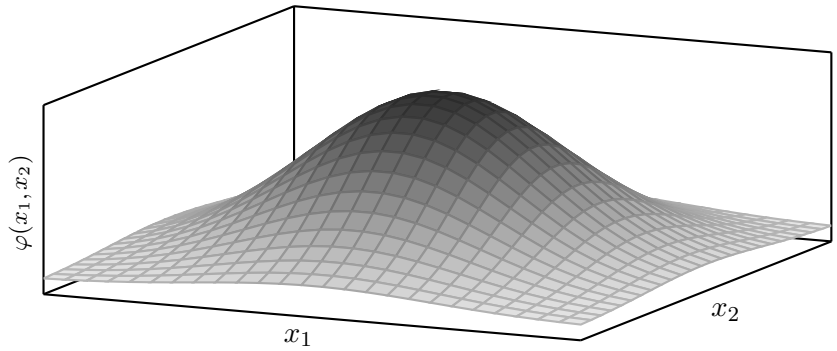

Figure 3.3: Probability density of a multivariate normal distribution for two random variables X_1 and X_2.

From this multidimensional probability distribution, also called joint probability distribution, the *marginal probability distribution* of each random variable x_i can be derived by integration. For two random variables X_1 and X_2 a possible joint probability distribution is given in figure 3.3. The marginal probability distribution of the random variable X_1 yields to

$$\varphi_{\mu,C}(x_1) = \int_{-\infty}^{\infty} \varphi_{\mu,C}(x_1, x_2)\, dx_2.$$

Since for the uncertainty dispersion analysis the continuous case is of importance, only the explanations and definitions for continuous random variables are of interest in the next sections.

3.2 Uncertainty Propagation

The uncertainty analysis method presented here is a direct method which aims to solve a PDF transport equation directly. The temporal evolution of a joint PDF over the state space, which changes with respect to the underlying dynamics, can be derived from the general formulation of the continuity equation for probability - the Liouville Equation [6].

For the next considerations, a non-linear state space model is required, since it governs specific system dynamics.

Definition 3.12 (State Space Model) *Let $f : \mathbb{R}^{n_x} \times \mathbb{R}^{n_p} \to \mathbb{R}^{n_x}$ be continuous differentiable and partially differentiable related to the states $x(t) \in \mathbb{R}^{n_x}$ and the parameters $p \in \mathbb{R}^{n_p}$, for all $t \in [t_0, t_f]$. The state x acts corresponding to the differential equation*

$$\dot{x} = f(x, p). \tag{3.12}$$

The system dynamics are governed by f, $t_0 \in \mathbb{R}$ denotes the starting time and $t_f \in \mathbb{R}$ the ending or final time.

This state space model can be put in an augmented form

$$\dot{\tilde{x}} = F(\tilde{x}), \tag{3.13}$$

where $\tilde{x} = (x, p)^\top \in \mathbb{R}^{n_x+n_p}$ is the extended state space.
The equation that governs the temporal evolution of probabilistic uncertainty in the initial conditions and parameters is given by the *Stochastic Liouville Equation* (SLE) which governs the probabilistic continuity equation.

$$\frac{\partial \varphi(\tilde{x}, t)}{\partial t} + \sum_{i=1}^{n_x} \frac{\partial}{\partial \tilde{x}_i}[\varphi(\tilde{x}, t) F_i(\tilde{x})] = 0 \tag{3.14}$$

This is a quasi linear partial differential equation (PDE) depending on the joint PDF $\varphi(\tilde{x}, t)$.
Using the Method of Characteristics (MOC) the PDE can be reduced along the trajectory to an ordinary differential equation (ODE) (see [2])

$$\frac{\mathrm{d}\varphi(\tilde{x}, t)}{\mathrm{d}t} = -\varphi(\tilde{x}, t)\Psi(\tilde{x}) \tag{3.15}$$

where $\Psi(\tilde{x}) = \sum_{i=1}^{n_x} \frac{\partial F_i}{\partial \tilde{x}_i}$ is the trace of the Jacobian of the dynamics (3.13) which evolves with time. With the initial state and parametric uncertainties specified in terms of a joint PDF $\varphi_0 = \varphi(\tilde{x}_0, t_0)$ the solution of (3.15) yields to

$$\varphi(\tilde{x}, t) = \varphi_0 \ \exp\left(-\int_0^t \Psi(\tau)\,\mathrm{d}\tau\right), \tag{3.16}$$

depending on the time t and the states $\tilde{x}$.
The marginal PDFs can be calculated by integrating out the states over the respective domains

$$\varphi(\tilde{x}_i, t) = \int_{\mathcal{D}_1} \cdots \int_{\mathcal{D}_{i-1}} \int_{\mathcal{D}_{i+1}} \cdots \int_{\mathcal{D}_{n_x}} \varphi(\tilde{x}, t)\, d\tilde{x}_1 \ldots d\tilde{x}_{i-1} d\tilde{x}_{i+1} \ldots d\tilde{x}_{n_x} \tag{3.17}$$

with $\mathcal{D}_i$ domain of the i^{th} state variable at time t, for $i = 1, \ldots, n_x$.

Analytical Formulation and Numerical Implementation of a One Dimensional Example

As a first one-dimensional example consider

$$\dot{x} = -x^2 \ , \text{ where } x(0) = x_0 \tag{3.18}$$

which in this case can be solved analytically. The solution of this initial value problem is given by

$$x(x_0, t) = \frac{x_0}{1 + t x_0}. \tag{3.19}$$

From this follows for the trace of the Jacobian

$$\Psi(\dot{x}) = -2x(t) = -\frac{2x_0}{1 + t x_0}$$
$$\Rightarrow \exp\left(-\int_0^t \Psi(x(\tau))\, \mathrm{d}\tau\right) = \exp\left(2x_0 \int_0^t \frac{1}{1 + \tau x_0}\, \mathrm{d}\tau\right) = (1 + t x_0)^2$$

and inserted into the solution of the Stochastic Liouville Equation (SLE) (3.16)

$$\varphi(x, t) = \varphi_0(x_0)(1 + t x_0)^2. \tag{3.20}$$

With the PDF the evolution of the initial conditions over time is described. Thus, the solution $x_0 = x_0(x, t)$ is needed. From (3.19) results

$$x_0 = \frac{x}{1 - tx}, \tag{3.21}$$

substituting to (3.20) yields

$$\varphi(x, t) = \varphi_0\left(\frac{x}{1 - tx}\right)\left(1 + \frac{x}{1 - tx}\right)^2, \tag{3.22}$$

where φ_0 is chosen as $\mathcal{N}(0; 1)$ the standard normal distribution.

In figure 3.4 the evolution of $\varphi(x, t)$ is presented. It is noticeable that for $t \to \infty$ the PDF of this one-dimensional example becomes a dirac delta distribution. The unique equilibrium ($f(t, x) = 0, \ \forall t$) of the dynamics in the asymptotic limit being the origin explains this behaviour. All probability mass moves to the origin.[2]

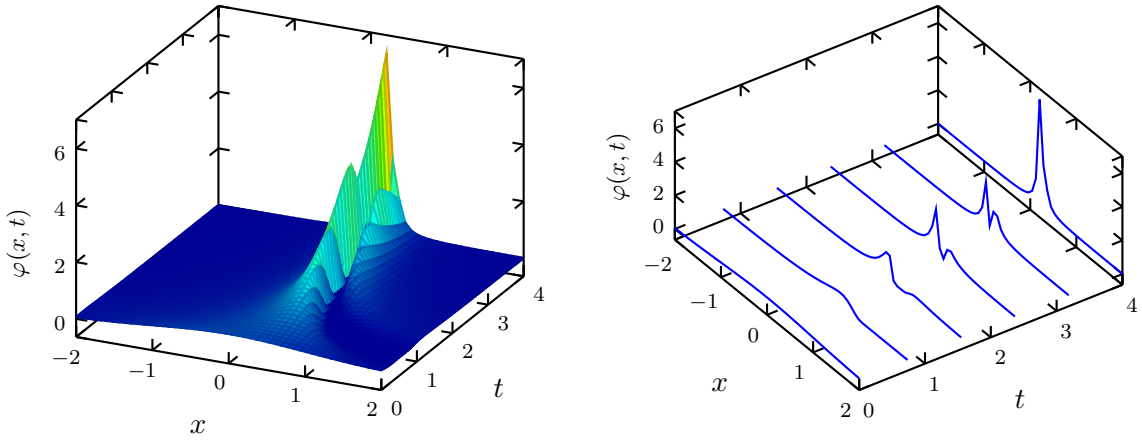

Figure 3.4: Evolution of the PDF of the one-dimensional example starting with the normal distribution $\mathcal{N}(0;1)$ at $t_0 = 0$. Over time the PDF tends towards the asymptotic limit of the impulse function (see [2]).

According to theory the from the SLE resulting PDF satisfies the criteria for a probability density function, see Definition 3.7. To ascertain this it is sufficient to check the normalization condition for each time step t_i, $i = 0, \ldots, n-1$.

$$\varepsilon_i = \int_{-\infty}^{\infty} \varphi(x, t_i)\, dx = 1 \tag{3.23}$$

To get a better overview if the estimated PDF violates the condition above the absolute error is observed

$$\Delta_{\varepsilon_i} = |1 - \varepsilon_i|. \tag{3.24}$$

In figure 3.5 this error Δ_ε is visualised for all time steps. The error fluctuates in an acceptable range.

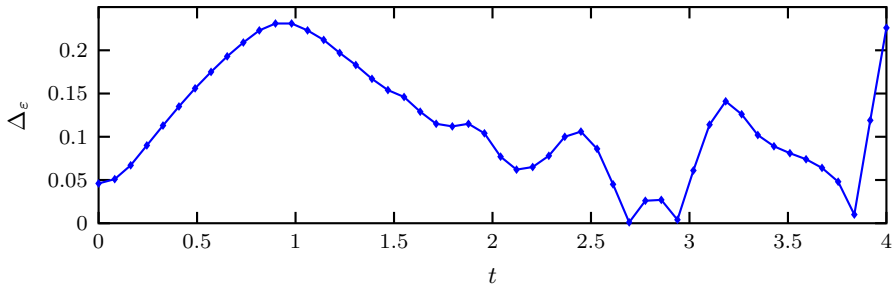

Figure 3.5: Error of the PDF of the one-dimensional example

Not all ODE's can be solved analytically. In this event, the ODE needs to be solved numerically with a suitable method. Since the SLE estimates the temporal evolution of

uncertainties in the initial conditions and a numerical solution depends on the chosen initial conditions, the ODE needs to be solved backwards in time to find $x_0(x,t)$. For a dispersion of the initial conditions the ODE is solved forward in time. The final values of this set of solutions is then used as initial conditions for the backward integration. The resulting $x_0(x,t)$ together with the analytically estimated trace of the Jacobian are used to predict the temporal evolution of uncertainties in the initial conditions using the solution of the Stochastic Liouville Equation. For a detailed view of this process see the flow chart in figure 3.6.

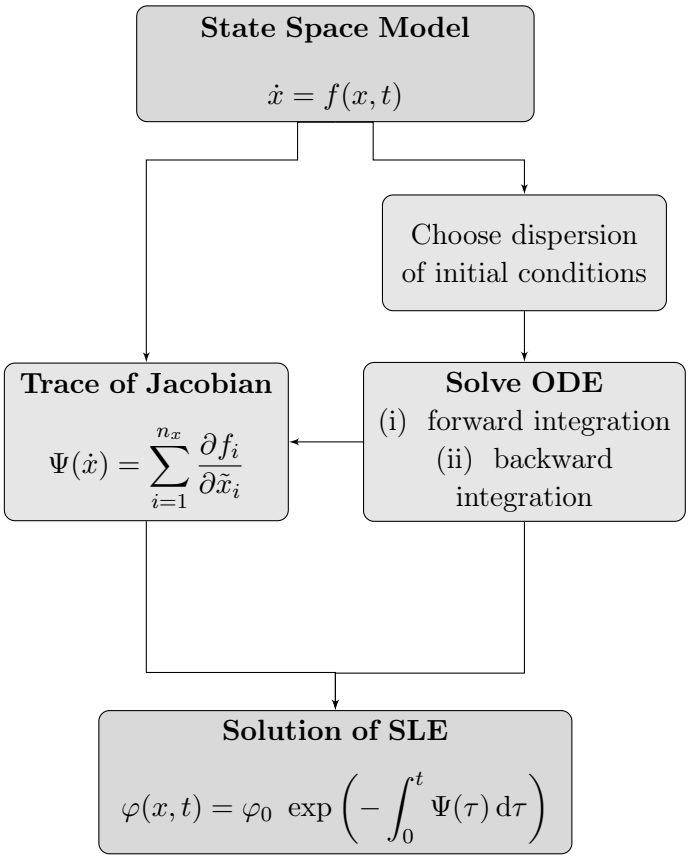

Figure 3.6: Flow chart of the process to numerically estimate the temporal evolution of a probability density function using the Stochastic Liouville Equation.

3.3 Analysis of the Three State Model

With the uncertainty dispersion analysis method explained in theory, different cases of the three state model are examined. In the following cases uncertainties in the states $x = (h,\ v,\ \gamma)^\top$ are considered. The used atmosphere models for Earth and Mars are the EAM by NASA Glenn Research Centre and the model taken from Noton, as presented in section 2.2.2.

3.3.1 Horizontal Flight

The first case examined at this point represents a horizontal movement of the re-entry vehicle. This can be conducted by a constant zero flight path angle and a constant altitude. For $\gamma \approx 0$ and $h = \text{const.}$ the three state model reduces to a one state model and only the second equation of (2.8) remains

$$\dot{v} = -\frac{\rho R_0}{2B_c} v^2. \tag{3.25}$$

This one state model can be solved analytically since it is similar to the one-dimensional example mentioned before. Note that ρ is depending on h, but since h is constant the same holds for ρ. This reduction leads to a horizontal movement at a constant altitude of the re-entry vehicle. The solution of (3.25) is given by

$$\begin{aligned} &\Rightarrow \int_{v_0}^{v} \frac{1}{v^2}\,\mathrm{d}v = \int_0^t -\frac{\rho R_0}{2B_c}\,\mathrm{d}t \\ &\Rightarrow v(t) = \frac{v_0}{1 + \frac{\rho R_0}{2B_c} v_0 t} \end{aligned} \tag{3.26}$$

The trace of the jacobian adds up to

$$\begin{aligned} &\Psi(\dot{v}) = -\frac{\rho R_0}{B_c} v(t) \\ &\Rightarrow \exp\left(-\int_0^t \Psi(v(\tau))\,\mathrm{d}\tau\right) = \left(1 + \frac{\rho R_0}{2B_c} v_0 t\right)^2. \end{aligned}$$

Inserting this into the solution of the Stochastic Liouville Equation (SLE) (3.16) results to

$$\varphi(v,t) = \varphi_0(v_0)\left(1 + \frac{\rho R_0}{2B_c} v_0 t\right)^2. \tag{3.27}$$

Solving (3.26) for v_0 and inserting the result into (3.27) yields

$$\begin{aligned} v_0 &= \frac{v}{1 - \frac{\rho R_0}{2B_c} v t} \\ \Rightarrow\ \varphi(v,t) &= \varphi_0\left(\frac{v}{1 - \frac{\rho R_0}{2B_c} v t}\right) \frac{1}{\left(1 - \frac{\rho R_0}{2B_c} v t\right)^2}. \end{aligned} \tag{3.28}$$

In this case hence, that given an initial PDF describing the initial uncertainties the PDF can be estimated at any time and velocity.
For the specific case of horizontal flight on Earth and Mars the constant altitude is set at $h_0 = 80\text{km}$. For an initial velocity of $v_0 = 3.5\frac{\text{km}}{\text{s}}$ the temporal evolution of the PDF in (3.28) is displayed for Earth and Mars in figure 3.7 for an initial uniform dispersion of 5% and 15% in v_0.

In both cases of dispersions, it can be observed that for Mars the velocity remains almost constant over time. In contrast for Earth the velocity decreases slightly over time for both dispersions. As expected for a wider dispersion the range of the velocity is wider as well.

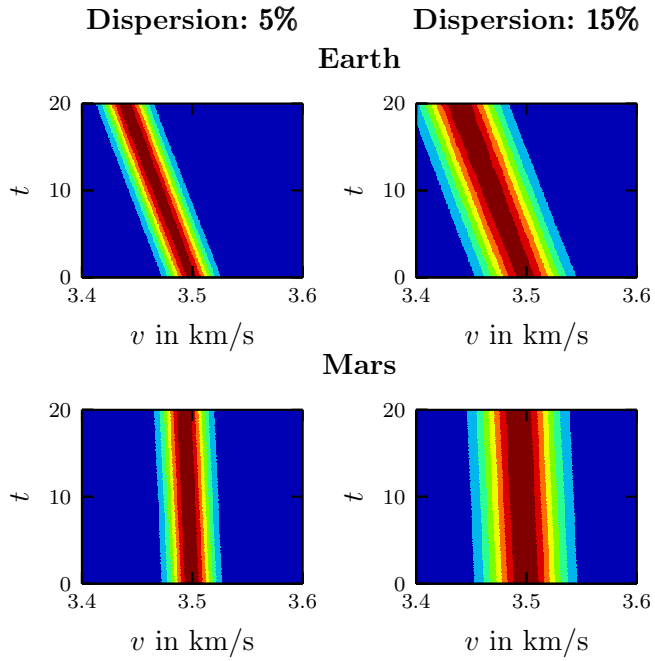

Figure 3.7: Temporal evolution of the PDF for horizontal flight of Earth (top) and Mars (bottom) for 5% (left) and 15% (right) uniform dispersion in v_0 at an altitude $h = 80\text{km}$.

Again to make sure that the calculated PDF in (3.28) is a PDF as characterised in Definition 3.7 the normalisation condition *(iii)* needs to be verified for every time step (see also (3.23)). In figure 3.8 the absolute error as introduced in (3.24) is presented. For both Earth and Mars the error rises monotonically with time for both dispersions. The error for Earth is ten times greater compared to Mars. In both cases the error is in an acceptable range.

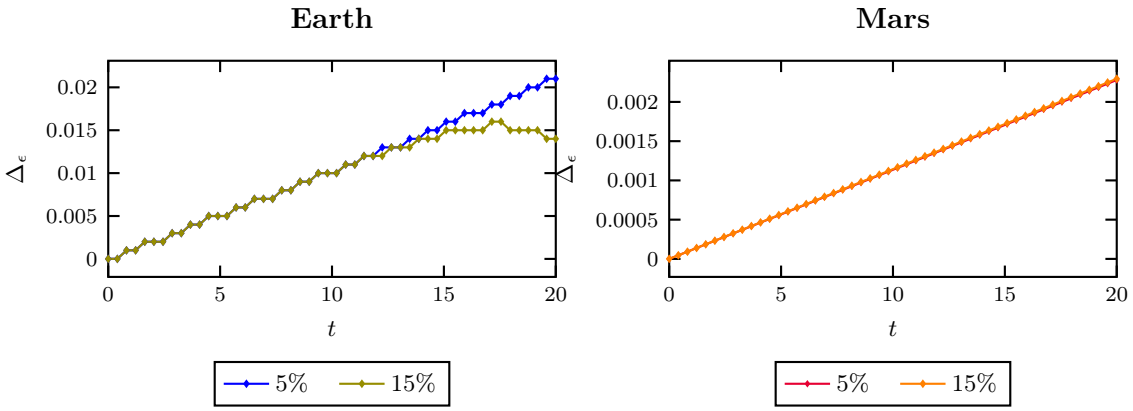

Figure 3.8: Absolute error of the violation of the normalisation condition of the PDF in case of horizontal flight for Earth and Mars for 5% and 15% dispersion.

3.3.2 Vertical Flight

The next case to be examined illustrates a vertical descent of the re-entry vehicle. This is ensured when the vehicles flight path angle points directly downwards ($\gamma = -\frac{\pi}{2} = -90°$) and the vehicle produces no lift. For a constant flight path angle γ the three state model reduces to a two state model

$$\dot{x} = \begin{pmatrix} \dot{h} \\ \dot{v} \end{pmatrix} = \begin{pmatrix} -v \\ -\frac{\rho}{2B_C} v^2 + g \end{pmatrix}. \tag{3.29}$$

In this case, the ODE system cannot be solved analytically and needs to be solved numerically. With the trace of the Jacobian given as

$$\Psi(\dot{x}) = -\frac{\rho}{B_C} v \tag{3.30}$$

the temporal evolution of the PDF can be estimated. In figure 3.9 the numerically calculated PDF for 5% and 15% uniform dispersion in the initial conditions $h_0 = 80\text{km}$ and $v_0 = 3.5\frac{\text{km}}{\text{s}}$ for Earth and Mars are displayed for the starting time t_0, midway during the descent t_{mid} and the end time t_f.
As expected the velocity and the altitude are decreasing over time. The same holds for the dispersions. The more time passes the smaller is the range of the bivariate PDF for altitude and velocity.

Likewise in the case before the estimated PDF for each time step is verified using the absolute error mentioned in (3.24), see figure 3.10. For Earth the error remains constant at about 0.06 and 0.12 for 5% and 15% dispersion. Also for Mars the error remains almost constant in case of 5% dispersion and increases monotonically with 15% dispersion in v_0. In contrast to the error of the PDF of the horizontal flight the deviation from the normalisation condition for Earth and Mars are of same order of magnitude.

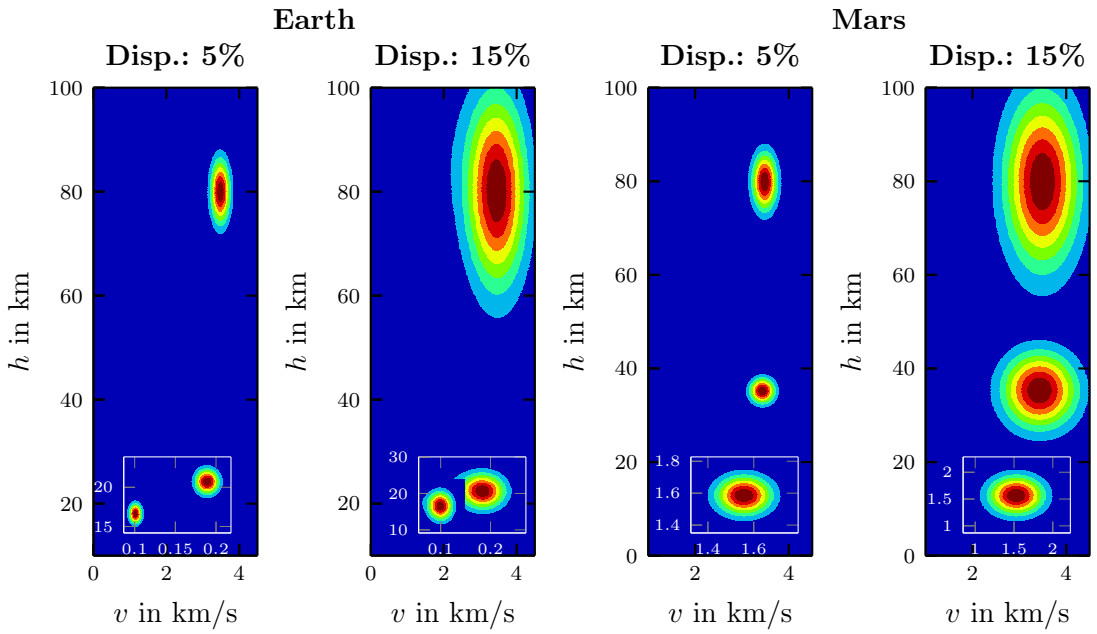

Figure 3.9: Temporal evolution of the PDF for vertical flight towards Earth and Mars for 5% and 15% uniform dispersion in v_0 and h_0 respectively. The PDFs are taken at time steps $t_0 = 0$s, t_f and midway t_{mid} during the descent. These times are $t_{mid} = 32.5$s and $t_f = 65$s for Earth and $t_{mid} = 12.5$s and $t_f = 25$s for Mars.

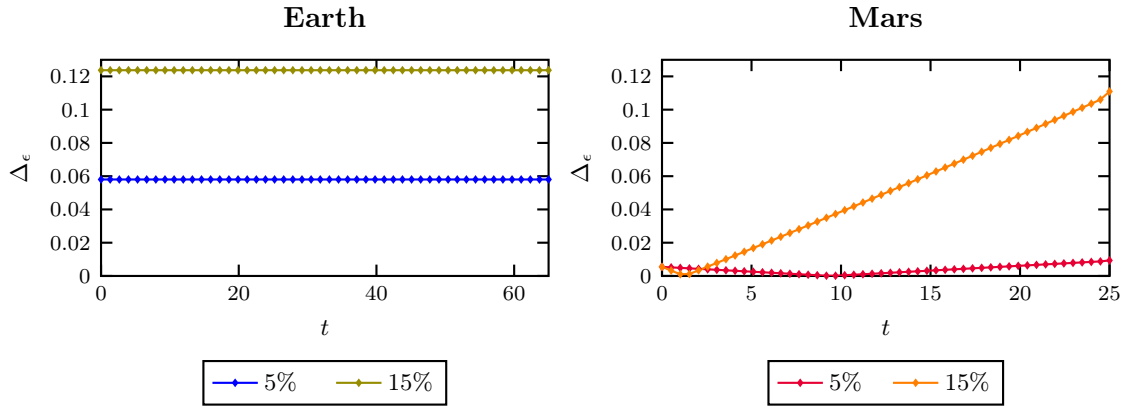

Figure 3.10: Absolute error of the violation of the normalisation condition of the PDF in case of vertical flight for Earth and Mars for 5% and 15% dispersion.

3.3.3 Re-Entry

In the last case the complete three state model is examined observing uncertainty dispersions in the initial states $(h_0,\ v_0,\ \gamma_0)^\top$. For the use in the Stochastic Liouville Equation the three state model is formulated as

$$\dot{x} = \begin{pmatrix} \dot{h} \\ \dot{v} \\ \dot{\gamma} \end{pmatrix} = \begin{pmatrix} v \sin\gamma \\ -\frac{\rho}{2B_C} v^2 - g \sin\gamma \\ \frac{\rho}{2B_C} \frac{C_L}{C_D} v + \cos\gamma \left(\frac{v}{R_0+h} - \frac{g}{v} \right) \end{pmatrix}. \tag{3.31}$$

The trace of the jacobian adds up to

$$\Psi(\dot{x}) = -\frac{\rho}{B_C} v - \sin\gamma \left(\frac{v}{R_0 + h} - \frac{g}{v} \right). \tag{3.32}$$

Likewise before, the complete three state model cannot be solved analytically. Therefore, the PDF is estimated numerically. The temporal evolution of the estimated PDF for 5% and 15% uniform dispersion in the inital conditions $h_0 = 80\text{km}$, $v_0 = 3.5\frac{\text{km}}{\text{s}}$ and $\gamma_0 = -2°$ is presented for Earth and Mars in figures 3.13 and 3.14 for three different time steps t_0, t_{mid} and t_f.

A dispersion in the initial conditions of 1% leads to a smaller over all range of the PDFs over time compared to the PDFs for a dispersion of 5%. For all cases the altitude and the velocity as well as the range of the dispersion is decreasing over time.
While descending onto Earth it is observable that the simulation stops at an altitude of $\approx 12\text{km}$. Due to numerical instabilities, the ODE adapted for Earth cannot be integrated further than $t_f = 350\text{s}$. Nevertheless, the estimated PDFs give a good impression of the temporal evolution of uncertainties in the initial conditions. In addition, the final touchdown executed by parachutes or descent thrusters is not considered here.

In case of Mars it is striking that for a dispersion of 1% the re-entry vehicle hits the ground, while for a dispersion of 5% the mean values of the PDFs remain at an altitude of $\approx$ 65km to $\approx$ 70km after decreasing from $h_0 = 80\text{km}$. The range of the initial dispersion induces that the vehicle skips off of the atmosphere. This behaviour is examined in more detail in section 3.4, when estimating a most probable trajectory from the temporal evolution of the PDFs.

In figure 3.11 the absolute error for each time step of the violation of the normalisation condition is displayed. In comparison to the error of the PDF of vertical flight towards Mars the error in this case increases monotonically in the same range of deviation. This changes in case of Earth. The error increases dramatically due to numerical instabilities. This problem already occurred during the numerical esaimation of the PDF. The ODE system adapted for Earth could not be solved further than 350s. This becomes more apparent when determining a most probable trajectory in section 3.4.
Doing further investigations it strikes that the magnitude of the absolute error depends on the atmosphere model. The atmosphere of Earth is denser than the atmosphere of Mars.

When scaling the atmosphere model of Earth down by a hundredth to match with the magnitude of Mars the absolute error decreases to the same magnitude as in case of Mars. In contrast, scaling the atmosphere model of Mars up by a hundredth the error increases dramatically, see figure 3.12.

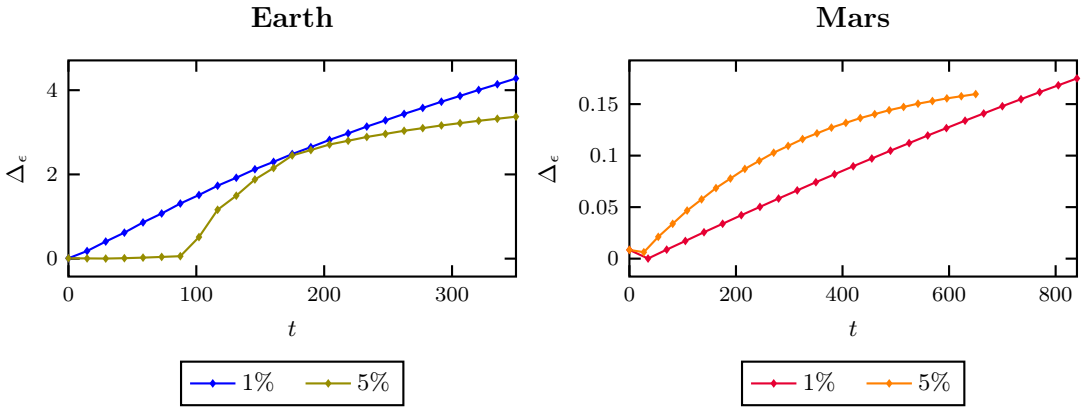

Figure 3.11: Absolute error of the violation of the normalisation condition of the PDF of the three state model for Earth and Mars for 1% and 5% uniform dispersion.

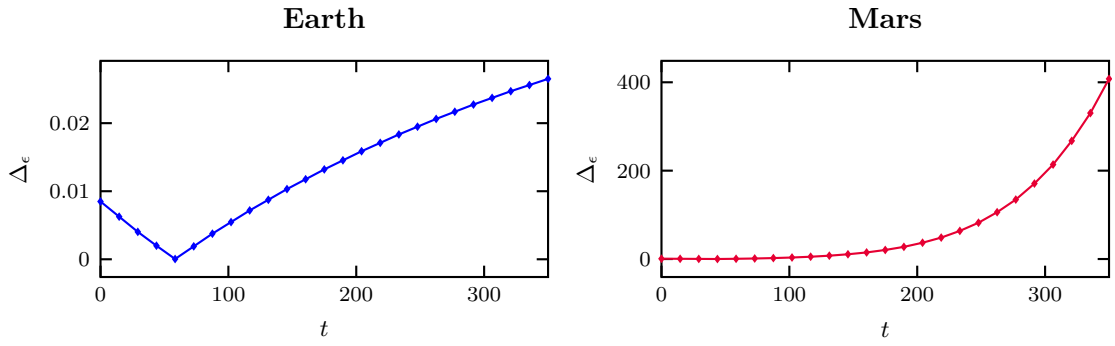

Figure 3.12: Absolute error of the violation of the normalisation condition of the PDF of the three state model for Earth and Mars for 5% uniform dispersion with scaled atmosphere models.

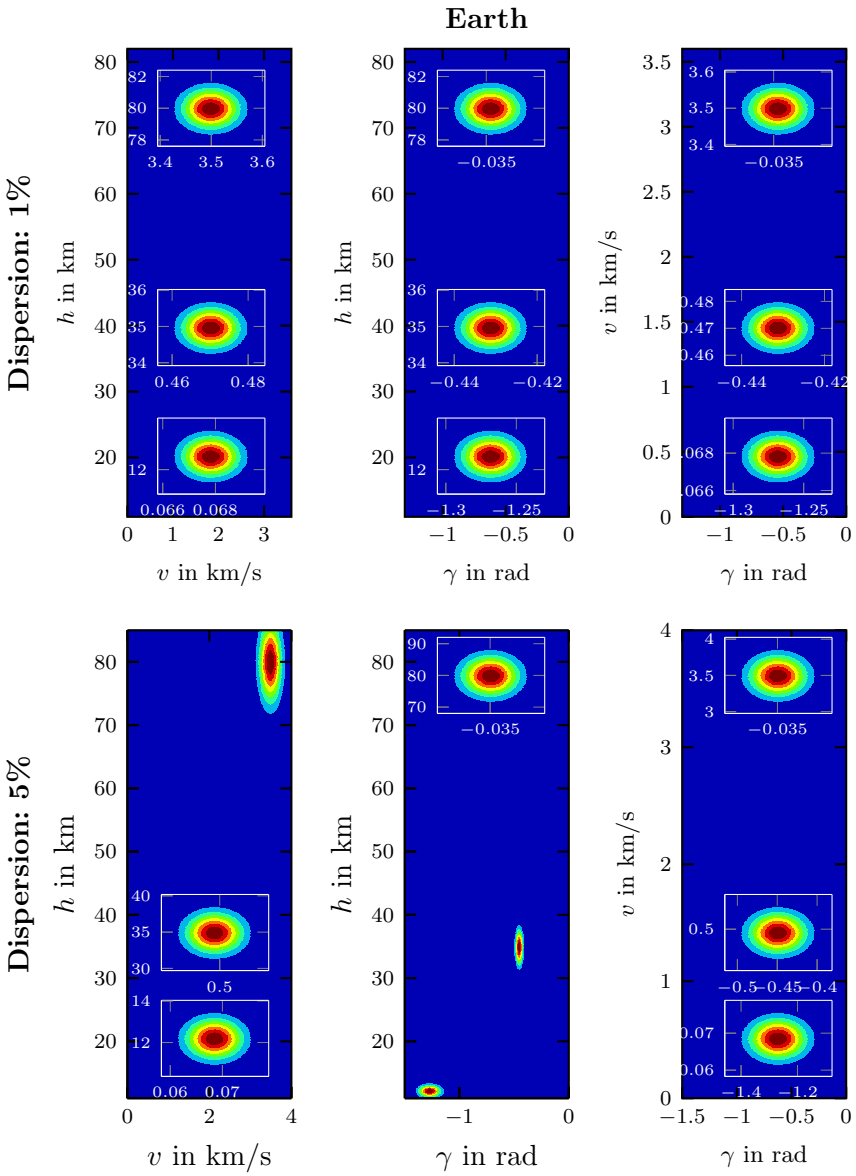

Figure 3.13: Temporal evolution of the PDF for re-entry onto Earth for 1% and 5% uniform dispersions in h_0, v_0 and γ_0. The PDFs are taken at time steps $t_0 = 0s$, $t_f = 350$s and midway $t_{mid} = 175$s during the descent.

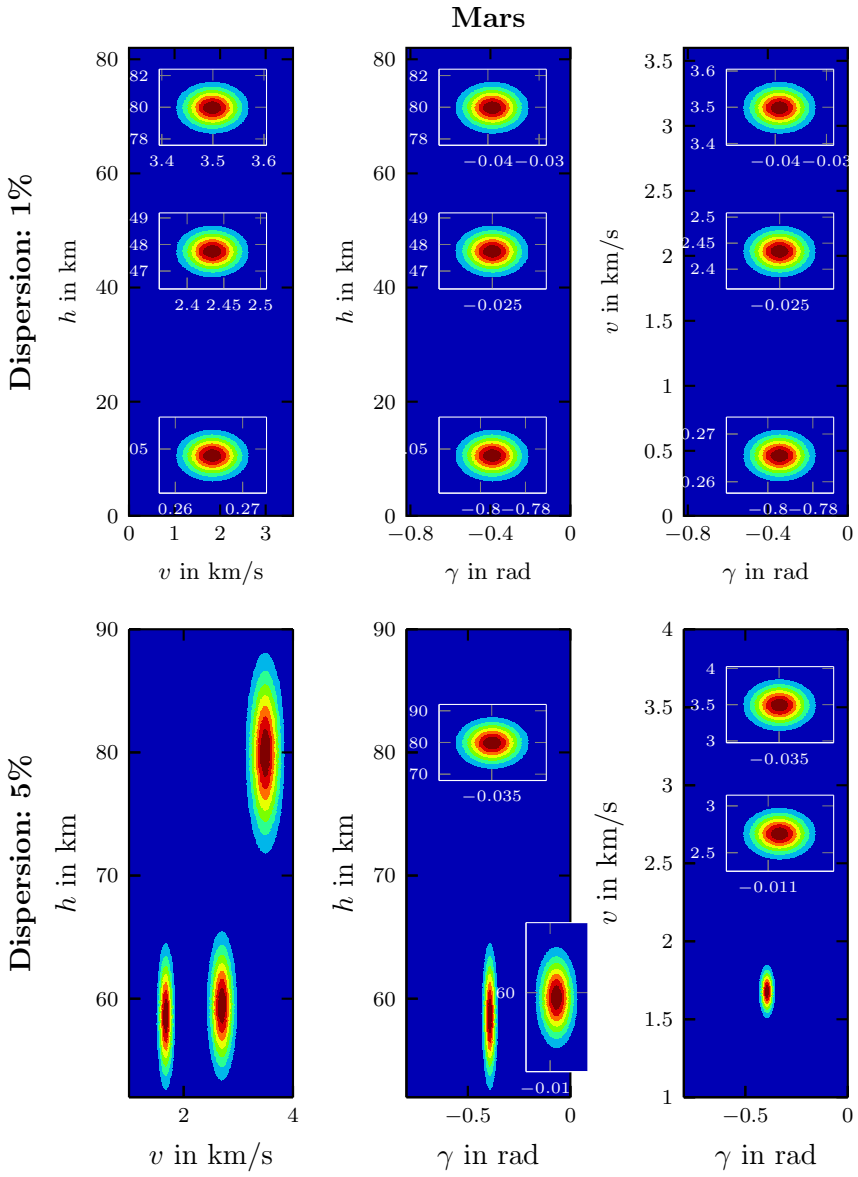

Figure 3.14: Temporal evolution of the PDF for re-entry onto Mars for 1% and 5% uniform dispersions in h_0, v_0 and γ_0. For the 1% dispersion the PDFs are taken at time steps $t_0 = 0s$, $t_f = 840$s and midway $t_{mid} = 420$s during the descent. For the 5% dispersion the time steps are $t_0 = 0$s, $t_{mid} = 325$s and $t_f = 650$s.

3.4 Most Probable Trajectory

From the temporal evolution of the joint PDFs a most probable trajectory can be estimated. For this purpose, the values of the states corresponding to the maxima of the marginal PDFs in each time step are merged into a trajectory. Additionally, error bars for the 1-σ and 3-*sigma* neighbourhood around the most probable trajectory are added. This procedure is done to analyse the three state model in the cases of vertical flight and re-entry further.

Vertical Flight

As explained in section 3.3.2 the trajectory depends only on altitude h and velocity v. The most probable trajectory (MPT) surrounded by error bars for the 1-σ and 3-σ neighbourhood is shown in figure 3.15. As before it is noticeable that the dispersion shrinks in range with proceeding time. The dispersion at the end of the simulations can be found in table 3.1.

		h_{end} in km				
	Disp.	**-3σ**	**-1σ**	**MPT**	**$+1\sigma$**	**$+3\sigma$**
Erde	**5%**	14.22	15.89	16.72	17.56	19.22
	15%	9.31	14.30	16.80	19.29	24.29
Mars	**5%**	1.35	1.51	1.59	1.67	1.83
	15%	0.85	1.32	1.56	1.79	2.27

Table 3.1: Dispersion at end time t_f for the altitude during vertical flight towards Earth and Mars for 5% and 15% initial dispersion.

Re-Entry

The most probable trajectories for Earth as well as Mars for dispersions of 1% and 5% are presented in figure 3.16 together with error bars for the 1-σ and 3-σ neighbourhood.

In case of 5% dispersion the re-entry vehicle does not hit the surface of Mars, but remains at an altitude of $h \approx 60$km. This thrives from the range of the dispersion. On Mars, initial conditions of $h_0 \geq 84$km with $v_0 \geq 3.675\frac{\text{km}}{\text{s}}$ result into trajectories where the vehicle bounces off of the atmosphere and wanders back into space leading to an altitude which first decreases but increases again after some time. This behaviour generates a most probable trajectory where the altitude remains almost constant and is not decreasing as one would expect. This is not surprising since the PDF is estimated using the expected value of the solution of the system dynamics in each time step. The expected value in each state by each time step is calculated as presented in (3.1). Since at some point in each trajectory with $h_0 \geq 84$km the altitude starts increasing again result in expected values where the lower altitude compensates the higher altitudes producing a MPT which first decreases and then remains almost constant at $h \approx 60$km from the point where some of

the trajectories started to bounce off of the planet's atmosphere.

For Earth this problem does not occur. With a dispersion of 5% around $h_0 = 80\text{km}$, $v_0 = 3.5\frac{\text{km}}{\text{s}}$ and $\gamma_0 = -2°$ the re-entry vehicle is able to land. This would change with different initial conditions but is not analysed further.
The MPT is decreasing and the vehicle is descending onto Earth but is not hitting its surface as seen in case of 1% dispersion for Mars. Due to numerical instabilities the three state model adpated for re-entry onto Earth cannot be integrated further than 350s with the set of initial conditions given by the 5% dispersion. Nevertheless, the analysis shows useful results for Earth as well as Mars. In table 3.2 the variation at t_f are gathered.

		h_{end} in km				
	Disp.	**-3σ**	**-1σ**	**MPT**	**$+1\sigma$**	**$+3\sigma$**
Erde	**1%**	11.76	12.01	12.12	12.25	12.49
	5%	10.36	11.58	12.19	12.81	14.02
Mars	**1%**	0.0521	0.0532	0.0537	0.0542	0.0553
	5%	49.83	55.69	58.62	61.55	67.41

Table 3.2: Dispersion at end time t_f for the altitude during re-entry onto Earth and Mars for 1% and 5% initial dispersion.

As mentioned before, the final touchdown (last $\approx$ 10km in case of Earth and last $\approx$ 1.5km in case of Mars) is not considered here. In particular, the effects of parachutes or descent thrusters are not included in the three state model.
Usually the vehicles are also controllable in their flight path angle to control the flight direction but also altering the FPA leads to changes in the vehicle's velocity. The controlled re-entry is observed further in section 4.2.

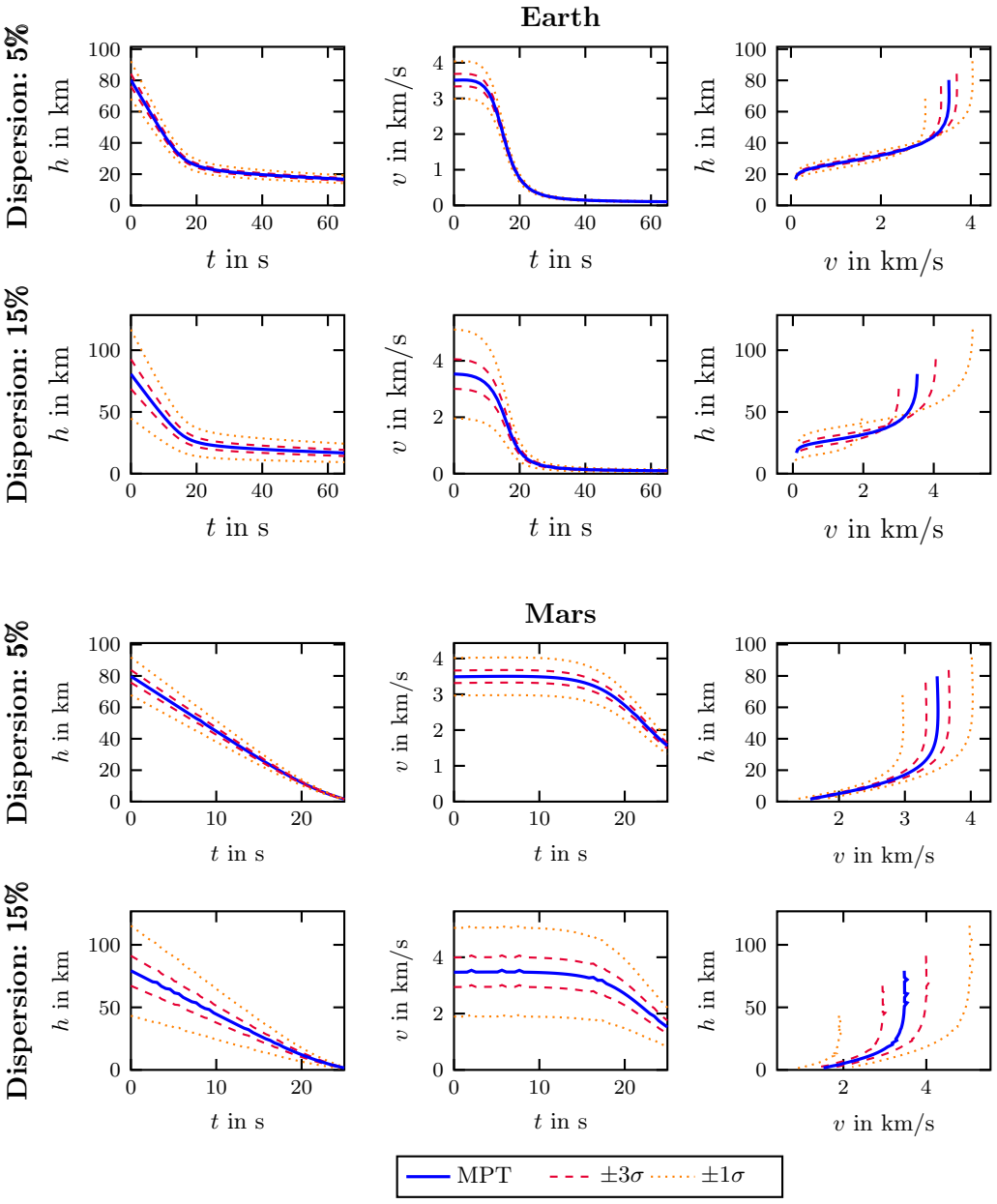

Figure 3.15: Most probable trajectory for vertical flight onto Earth (top) and Mars (bottom) with 5% and 15% uniform dispersion in v_0 and h_0 respectively.

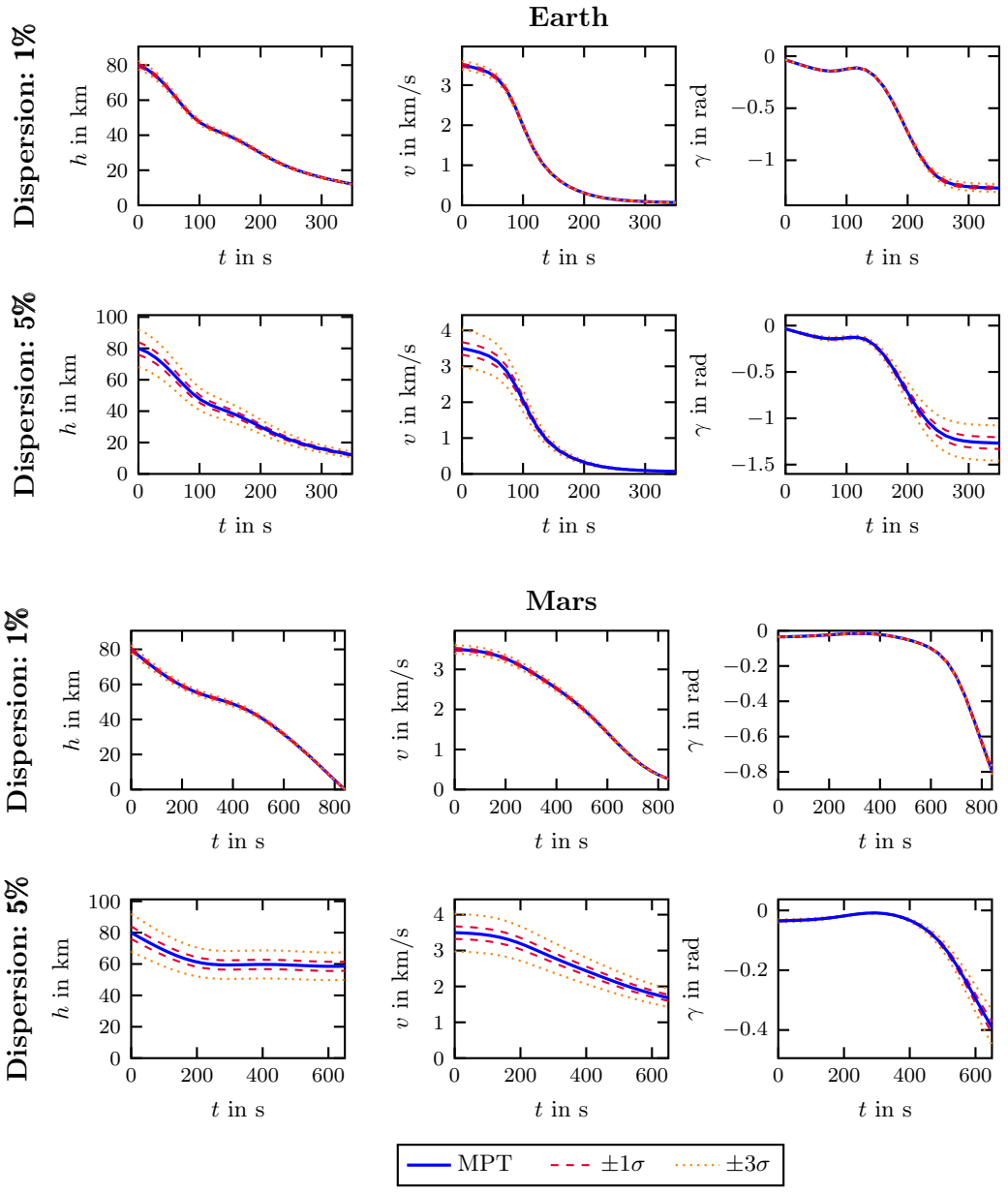

Figure 3.16: Most probable trajectory for re-entry onto Earth (top) and Mars (bottom) with 1% and 5% uniform dispersion in v_0, h_0 and γ_0 respectively.

3.5 Landing Dispersion from Covariance Matrix

The main focus when analysing uncertainties and their evolution throughout the entry, descent and landing sequence is laid on landing dispersions and landing footprints. The resulting landing dispersions influence the landing site selection and give an impression on the range across the landing site and possible hazards.

To estimate the landing dispersion from the calculated PDFs the covariance matrix is needed. This matrix as well as the expected value and the variance can be computed from a PDF.

Definition 3.13 (Covariance Matrix from PDF) *For a continuous random vector $X : \Omega \to \mathbb{R}^n$ and a probability density function $\varphi_x(x,t) \in \mathbb{R}^{n_x}$ with $x \in \mathbb{R}^{n_x}$ and $t \in [t_0, t_f]$*

$$\begin{aligned} C(X) &= E((X - E(X)) \cdot (X - E(X))^\top) \\ &= \int (x - E(X)) \cdot (x - E(X))^\top \varphi_x(x)\,\mathrm{d}x \\ &= \int x x^\top \varphi_x(x)\,\mathrm{d}x - E(X) \cdot E(X)^\top \end{aligned} \tag{3.33}$$

with the expected value

$$E(X,t) = \int x \varphi_x(x,t)\,\mathrm{d}x.$$

This gives a covariance matrix for the random vector X as in (3.5).

Theorem 3.14 *A covariance matrix C of a random vector X has the properties*

(i) C is symmetric

$$C^{ij} = C^{ji}.$$

(ii) C is definite non-negative for any $x \in \mathbb{R}^{n_x}$

$$x^\top C^{-1} x \geq 0.$$

(iii) If C is positive definite, then, for any $x \in \mathbb{R}^{n_x}$

$$\|x\| = (x^\top C^{-1} x)^{\frac{1}{2}}$$

has the properties of a norm.

with the notation $C^{ij} = C(x_i, x_j)$, for $i, j = 1, \ldots, n_x$.

Proof. A proof of this theorem can be found in [26]. □

The variance, given on the diagonal of the covariance matrix C, and the covariance, given by the non-diagonal entries of the covariance matrix C, define the spread and the distribution of X. With this a covariance ellipse or covariance ellipsoid[1] can be generated depending on the dimensions of the covariance matrix. In case of two-dimensional data the covariance matrix gives an ellipse and for three-dimensional data it results in an ellipsoid.

To deduce the covariance ellipse or ellipsoid from the covariance matrix the eigenvectors and eigenvalues are necessary. The eigenvectors define the orientation in each dimension. The square root of the corresponding eigenvalues defines the semi-axis of the ellipsoid.

The uncertainty dispersion analysis of the three state re-entry dynamics propagates probability densities $\varphi_x(x,t)$ for each time step $t_i \in [t_0, t_f]$, for $i = 0, \ldots, m$. For each time step a covariance matrix $C(x,t_i)$ can be derived and with the procedure above a covariance ellipsoid in the state space $x = (h, v, \gamma)^\top$ can be generated. In figure 3.17 the covariance ellipsoid at time step $t_f = 840$s for the re-entry onto Mars with 1% dispersion is displayed. Since the six state model is not analysed concerning the temporal evolution of uncertainties a landing ellipse cannot be deduced here.

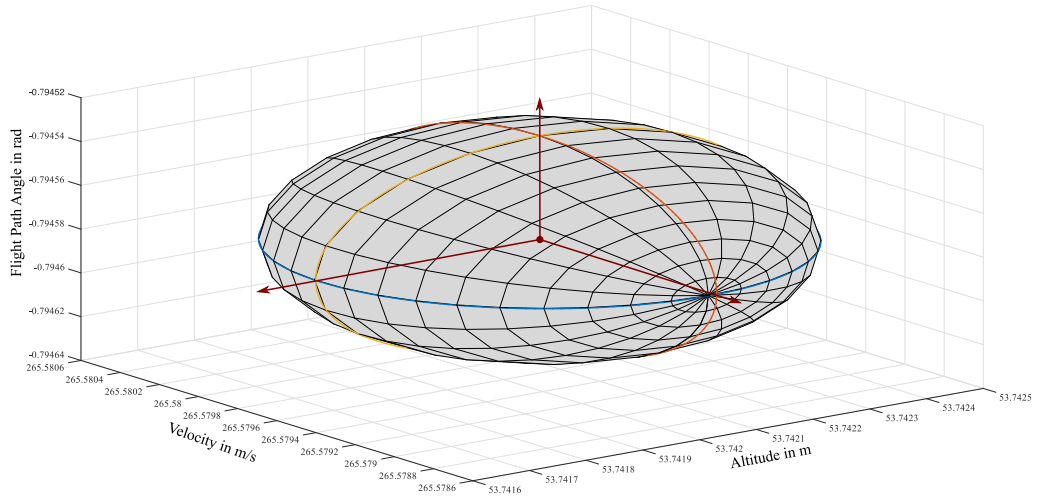

Figure 3.17: 1-σ Covariance ellipsoid for re-entry onto Mars estimated from the PDF with 1% uniform dispersion at $t_f = 840$s.

When analysing the six state model the covariance matrix of latitude and longitude at time t_f of the touch down can be deduced to a landing ellipse. In figure 3.18 a schematic view of a landing ellipse is presented. The ellipse evolves around the nominal trajectory. The maximum and minimum downrange trajectories mark the length and the maximum and minimum cross range trajectories the width of the landing ellipse.

The range and orientation of the landing dispersion depends on different contributing factors. These are navigation uncertainties, atmosphere model uncertainties, spacecraft

[1] also called error ellipse or error ellipsoid

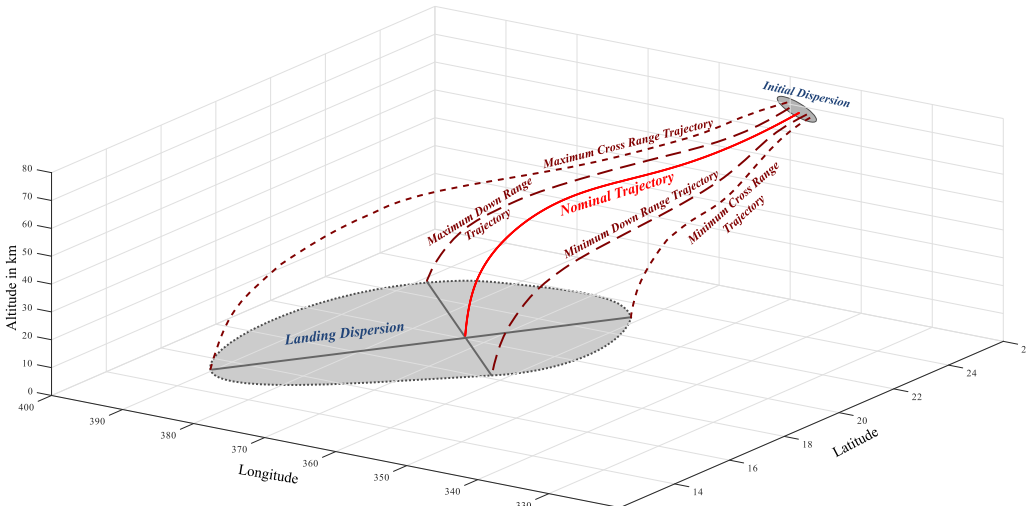

Figure 3.18: Schematic explanation of the landing dispersion when analysing the six state model.

modelling uncertainties, winds and EDL margins. The main influence on the geometry of the landing ellipse emerges from the atmosphere density uncertainties and the spacecraft modelling uncertainties. The atmospheric uncertainties are caused by the atmosphere measurements and the resulting model. For example low densities cause the vehicle to go further down-track, while high densities cause the vehicle to move up-track of the mean [45].
The spacecraft modelling uncertainties strive from the aerodynamic coefficients. Since the aerodynamic behaviour of the re-entry vehicle is mainly measured or simulated and the coefficients are then calculated from these measurements, the aerodynamic coefficients the lift-to-drag ratio $\frac{C_L}{C_D}$ and the ballistic coefficient B_C are subjected to a range of inaccuracies. In figure 3.19 first estimations of landing ellipses for the Mars Exploration Rover Spirit are given for each contributing factor [45].

Another possible method to estimate the landing dispersion is presented in [9]. Here the covariance matrix is directly derived from the system dynamics. In contrast to the method presented in this thesis, this so called *Linear Covariance Analysis* uses linearized system dynamics and utilises a beforehand calculated nominal trajectory to develop covariance propagation and update equations. The covariance equations are used to propagate statistics on navigation error, trajectory position as well as velocity and attitude error. See [9, 10] for further details.

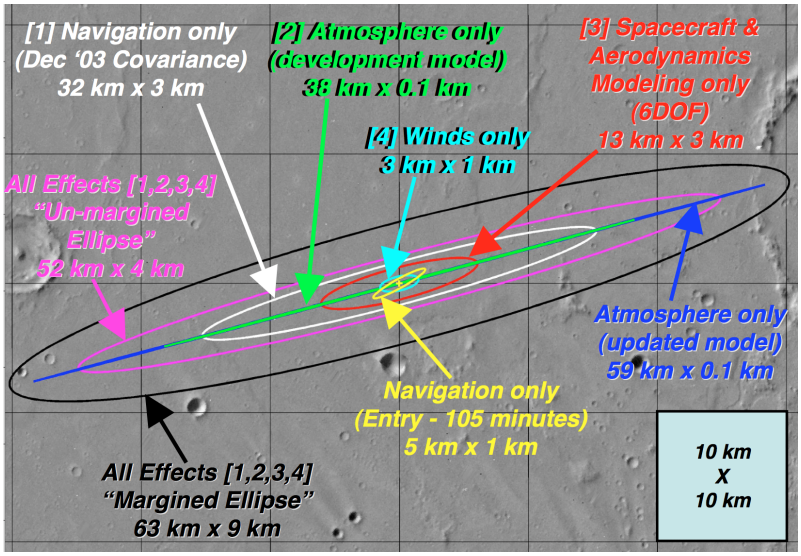

Figure 3.19: First propagations of the landing dispersion and its contributors of the Mars Exploration Rover Spirit [45]

Chapter 4

Optimal Control of Re-Entry Trajectories

Usually re-entry, descent and landing is executed by manoeuvrable vehicles which means that the re-entry vehicle itself can control the trajectory it takes towards the planet. In some cases, it is not only necessary to control the vehicle actively but it is also advantageous since it enlarges the re-entry corridor and gives the possibility to reach a predefined target from each entry point. One possible way to manoeuvre a re-entry vehicle is to use flaps. With flaps the performances of the vehicle can be influenced directly since the aerodynamic properties change. In figure 4.1 a concept of a manoeuvrable re-entry vehicle with flaps is shown [63].

Figure 4.1: Concept of a controllable re-entry vehicle with flaps [63].

When examining controlled re-entry, it is of interest to find the optimal trajectory concerning for example the descent time or the loads acting on the vehicle. And in order to manoeuvre the vehicle along the optimal trajectory the angles of attack of the flaps while descending need to be estimated.

The optimal controlled descent onto Earth and Mars is examined in this chapter.

At first the necessary fundamentals in optimization and optimal control are presented. Afterwards the three state model is optimized. At last the optimized trajectories are analysed concerning the dispersion of uncertainties using the method presented in section 3.2.

4.1 Fundamentals in Optimization and Optimal Control

Optimization can be found in different fields of research in science, engineering and even in economics. Typical examples are the minimization of costs or the maximization of profit in trading, the minimization of emissions or the minimization of energy consumption in automotive or aviation industry.
When optimising processes those are often exposed to certain system dynamics. Those optimization problems are denoted as *optimal control problems*, since most often these dynamics can be affected or controlled extraneous. Those processes could be for example optimal ascent of a sounding rocket, optimal path-planning or other branches of aerospace. But not just there, also in robotics or in the automotive industry those optimal control problems are common.

First the fundamentals in nonlinear optimization are presented starting with the standard optimization problem and the necessary and sufficient conditions for an optimum. A numerical solution method and a solver which utilises this method is introduced afterwards. These illustrations are based on [35, 40, 41].
Later the optimal control problem is laid out and a solution procedure is presented. These fundamentals in optimal control are based on [31, 40, 42, 43].

4.1.1 Nonlinear Optimization

In optimization one strives to find an optimal solution of an objective function with regard to specific constraints.

Definition 4.1 (Nonlinear Programm (NLP)) *Let $n, m \in \mathbb{N}$ with $m = m_1 + m_2$, $0 \leq m_1 < m_2$, $x \in \mathbb{R}^{n_x}$, $f : \mathbb{R}^{n_x} \to \mathbb{R}$ and $g : \mathbb{R}^{n_x} \to \mathbb{R}^m$ be continuously differentiable, then*

$$\begin{aligned} &\min_x \ f(x) \\ \textit{subject to} \quad &g_i(x) = 0, \quad i = 1, \ldots, m_1 \\ &g_i(x) \leq 0, \quad i = m_2, \ldots, m \end{aligned} \tag{4.1}$$

is called a nonlinear optimization problem depending on the objective function f *and* constraints g. *The constraints can occur as* equality *or* inequality *constraints.*

Since a maximization problem can be easily converted to a minimization problem and vice versa

$$\max_x f(x) = \min_x -f(x)$$

only minimization problems are examined.
A solution of the objective function is only feasible, if it meets the constraints.

Definition 4.2 (Feasible Point) *A $x \in \mathbb{R}^{n_x}$ is called* feasible*, if*

$$g_i(x) = 0, \quad i = 1, \ldots, m_1,$$
$$g_i(x) \leq 0, \quad i = m_2, \ldots, m.$$

All feasible points are gathered in the *active set.*

Definition 4.3 (Active Set) *The constraint $g_i(x) \leq 0$ is called* active *if $g_i(x) = 0$ and elsewise inactive. Therefore, equality constraints are always active. The set*

$$\mathcal{A}(x) := \{i \in \{1, \ldots, m\} |\ g_i(x) = 0\}$$

is called the index set of active constraints.

The minimum of a constrained minimization problem is subjected to necessary and sufficient conditions. To present these conditions in a more compact manner, the Lagrange function is introduced.

Definition 4.4 (Lagrange Function) *The Lagrange function is defined as*

$$L(x, \lambda) := f(x) + \sum_{i=1}^{m} \lambda_i g_i(x) \tag{4.2}$$

with $L : \mathbb{R}^{n_x \times m} \to \mathbb{R}$ and Lagrange multipliers *$\lambda \in \mathbb{R}^m$.*

In order to guarantee the validity of the necessary conditions, the constraints g of the optimization problem must hold the regularity conditions.

Definition 4.5 (Regularity Conditions) *The constraints g satisfy the LICQ[1] regularity conditions in $x \in \mathbb{R}^{n_x}$, if $\nabla_x g_i(x)$ are linearly independent for $i \in \mathcal{A}(x)$.*

The necessary conditions of first order are gathered in the KKT-conditions, named after Karush, Kuhn and Tucker.

Theorem 4.6 (KKT-Conditions) *Let $x^* \in \mathbb{R}^{n_x}$ be a local minimum of the nonlinear optimization problem (4.1). Furthermore let f and g be continuously differentiable and let g meet the LICQ-regularity conditions in x^*. Then there exist unique defined multipliers $\lambda^* \neq 0$, so that applies*

(i) Optimality condition:

$$\nabla_x L(x^*, \lambda^*) = \nabla_x f(x^*) + \sum_{i=1}^{m} \lambda_i^* \nabla_x g_i(x^*) = 0$$

[1] LICQ: Linear Independence Constraint Qualification.

(ii) Primal Feasibility:

$$g_i(x^*) = 0, \quad i = 1, \dots, m_1$$
$$g_i(x^*) \leq 0, \quad i = m_2, \dots, m$$

(iii) Dual Feasibility:

$$\lambda_i^* \geq 0, \quad i = m_2, \dots, m$$

(iv) Complementary Slackness:

$$\lambda_i^* g_i(x^*) = 0, \quad i = 1, \dots, m \tag{4.3}$$

The pair (x^*, λ^*) *is called a* KKT point.

Proof. A proof of this theorem can be found in [33]. □

With the strict complementarity condition, redundancy of the constraints with regard to the objective function is postulated. If for one side condition holds $g_i(x) = \lambda_i = 0$, it has no influence on the objective function.

Definition 4.7 (Strict Complementary Slackness) *A KKT-point* (x^*, λ^*) *satisfies the* strict complementary slackness *condition if in addition to* (4.3)

$$\lambda_i + g_i(x^*) \neq 0, \quad i = m_2, \dots, m$$

holds. Which means that the Lagrange multipliers of active constraints do not vanish.

To decide if a KKT-point is an optimum sufficient conditions are necessary. First the search directions can be restricted since a constrained optimality problem is examined here.

Definition 4.8 (Critical Cone) *The* critical cone *is defined for a feasible point in* (4.1) *as*

$$\mathcal{K}(x) := \ ker\ \nabla g^a(x) = \{d \in \mathbb{R}^n |\ \nabla_x g_i(x)^\top d = 0, \forall i \in \mathcal{A}\}.$$

Here $\nabla g^a(x)$ *denotes the Jacobian matrix of the active constraints.*

With the second derivative also known as *Hessian matrix* of the Lagrange function the sufficient optimality condition can be formulated.

Definition 4.9 (Sufficient Optimality Condition) *Let* (x^*, λ^*) *be a KKT-point satisfying the LICQ regularity condition and the strict complementary slackness condition. Let* f *and* g *be sufficiently often continuously differentiable. The point* (x^*, λ^*) *is a strict local minimum of* (4.1) *if*

$$d^\top \nabla^2_{xx} L(x^*, \lambda^*) d > 0, \quad \textit{for all } d \in \mathcal{K}(x^*),\ d \neq 0.$$

Proof. A proof of this theorem can be found in [33]. □

With all conditions for an optimal solution of nonlinear optimization problems presented the next step is to find such optimal solutions.
Since optimality problems in the form of 4.1 are challenging and extensive to solve analytically, the process to find an optimum analytically is not discussed here. Therefore, one possible numerical method to find optimal solutions is presented. With the *SQP-method*[2] one strives to approximate the optimal solution using a quadratic sub problem.

Definition 4.10 (Quadratic Optimization Problem (QP)) *Let* $Q \in \mathbb{R}^{n_x \times n_x}$, $A \in \mathbb{R}^{m_1 \times n_x}$, $B \in \mathbb{R}^{m-m_1 \times n_x}$, $c \in \mathbb{R}^{n_x}$, $v \in \mathbb{R}^{m_1}$, $w \in \mathbb{R}^{m-m_1}$. *With* $x \in \mathbb{R}^{n_x}$ *the* quadratic problem *is of the form*

$$\begin{aligned} \min_{x} \quad & \frac{1}{2} x^\top Q x + c^\top x \\ \textit{subject to} \quad & Ax - v = 0, \\ & Bx - w \leq 0. \end{aligned} \tag{4.4}$$

The SQP-method attempts to iteratively generate a sequence $x^{[0]}$, $x^{[1]}$, ... towards the optimum x^*. The basic algorithm (taken from [41]) is presented below.

i. Check whether $x^{[k]}$ satisfies a termination criterion. If it does, terminate.

ii. Approximate the nonlinear problem by a quadratic sub problem in $x^{[k]}$ and use its solution $d^{[k]}$ as the search direction.

iii. Determine a step size β_k by applying a line search method to a merit function.

iv. Update the iterate $x^{[k+1]} = x^{[k]} + \beta_k d^{[k]}$, increment k and go to 1.

The QP approximates the NLP using the Taylor-series expansion. The Lagrange function L is approximated up to second order and the constraints g up to first order. This yields the quadratic auxiliary problem.

Definition 4.11 (Quadratic Auxiliary Problem) *Let* L *be the Lagrange function as in* (4.2), f *and* g *as in* (4.1). *For* $d^{[k]} \in \mathbb{R}^n$ *a quadratic sub problem is expressed as*

$$\begin{aligned} \min_{d^{[k]}} \quad & {d^{[k]}}^\top \nabla^2_{xx} L(x^{[k]}, \lambda^{[k]}) d^{[k]} + \nabla F(x^{[k]})^\top d^{[k]} \\ \textit{subject to} \quad & g_i(x^{[k]}) + \nabla g_i(x^{[k]})^\top d^{[k]} = 0, \quad i = 1, \ldots, m_1, \\ & g_i(x^{[k]}) + \nabla g_i(x^{[k]})^\top d^{[k]} \leq 0, \quad i = m_2, \ldots, m. \end{aligned} \tag{4.5}$$

A possible termination criterion could be illustrated by the optimality condition of the KKT-conditions. But checking this is challenging when using a numerical method due to inaccuracies. A more reasonable termination criterion could be

$$\|\nabla_x L(x^*, \lambda^*)\|_\infty < \epsilon_{\text{opt}},$$

[2] SQP stands for Sequential Quadratic Programming

with a specific bound $\epsilon_{\text{opt}} > 0$.

The SQP-method is used in the NLP-solver WORHP.

WORHP

The library WORHP (*"We Optimize Really Huge Problems"*) is developed by the Centre of Industrial Mathematics of the University of Bremen and is designed to solve nonlinear optimization problems. The SQP method together with the Interior-Point[3] method is used to find locally optimal points. The solver can handle problems with more than 10^6 optimizations variables and exploits sparse structures of the objective function and constraints for more computation efficiency.

4.1.2 Optimal Control

The problem (4.1) can be subjected to a system of differential equations which can be controlled from the outside leading to the theory of optimal control.

Therefore, the dynamics introduced in Definition 3.12 are extended by the control $u(t) \in \mathbb{R}^{n_u}$

$$\dot{x} = f(x, u, t) \tag{4.6}$$

together with the states $x(t) \in \mathbb{R}^{n_x}$. Note that the parameters p are neglected here. As well as in optimization the optimal control problem consists of an objective functional[4] to which an optimal trajectory has to be found.

Definition 4.12 (Objective Functional) *Let $\Phi : \mathbb{R}^{n_x \times n_x} \to \mathbb{R}$ continuously differentiable and $f_0 : \mathbb{R}^{n_x \times n_u} \to \mathbb{R}$ continuous and relating to x and u continuously partially differentiable. The* objective functional *of an optimal control problem is then formulated as*

$$I(x, u) = \Phi(x(t_f)) + \int_0^{t_f} f_0(x(t), u(t), t)\, dt$$

The introduced dynamics underlie initial and final conditions which are gathered in the boundary constraints.

Definition 4.13 (Boundary Constraints) *Let $\xi : \mathbb{R}^{n_x \times n_x} \to \mathbb{R}^r$ be continuously differentiable with $0 \leq r \leq 2n_x$. Then*

$$\xi(x(t_0), x(t_f)) = 0$$

denotes the boundary constraints *of the optimal control problem.*

[3] for further details see [33] or [35].
[4] in some disciplines also called *cost functional*

The optimal control problem is as well as the nonlinear optimization problem subjected to constraints. This can be trivial box constraints or more complex conditions.

Definition 4.14 (Path Constraints) *Let* $g : \mathbb{R}^{n_x \times n_u} \to \mathbb{R}^m$ *be continuously differentiable with* $m \geq 0$. *Then*

$$g(x(t), u(t)) \leq 0, \quad \textit{for all } t \in [t_0, t_f]$$

denotes the general path constraints *of the optimal control problem.*

All above explanations are merged into the *optimal control problem.*

Definition 4.15 (Optimal Control Problem (OCP)) *From the previous definitions, the standard optimal control problem follows as*

$$\begin{aligned} \min_{x,u,p,t_f} \quad & I(x,u) = \Phi(x(t_f)) + \int_0^{t_f} f_0(x(t), u(t), t)\, dt \\ \textit{subject to} \quad & \dot{x} = f(x(t), u(t), t), \\ & \xi(x(0), x(t_f)) = 0, \\ & g(x(t), u(t)) \leq 0, \quad t \in [0, t_f]. \end{aligned} \tag{4.7}$$

The solution of the optimal control problem consists of the optimal trajectory $x^*(t)$, the optimal control $u^*(t)$.

Remark 4.16 *Depending on the properties of* f_0 *and* Φ *in the objective function, the optimal control problem is classified as*

(i) Bolza problem: $f_0 \neq 0$ *and* $\Phi \neq 0$

(ii) Mayer problem: $f_0 \equiv 0$

(iii) Lagrange problem: $\Phi \equiv 0$

All these problems can be transferred into each other. For further details see [40].

There are two different methods to solve such problems: indirect and direct. On the one hand, this problems can be solved using an indirect method where theoretical results of the *minimum principle of Pontryagin* are used to convert the optimal control problem into a boundary value problem, see [40] for further details.
Here, the focus is placed on the direct methods, since the solver used to solve the optimal re-entry problem utilises this second class of possible solution procedures. But also, this method does not need as good and precise initial estimates as in case of indirect methods.

Direct Method

The direct method strives to determine approximate values for the integral and the right-hand site of the differential equations at selective supporting points. By discretising the control and state functions the infinite-dimensional optimal control problem is converted into a finite optimization problem.

Therefore, the continuous time axis $t \in [t_0, t_f]$ is replaced by a set of discrete grid points

$$t \in 0 = t_1 < t_2 < \cdots < t_l = t_f, \quad l \in \mathbb{N}$$

which not necessarily have to be equidistant. Thus, instead of determining a state function $x(t)$ and a control function $u(t)$, only vectors of discrete values $u = (u^1, \ldots, u^l)^\top$ and $x = (x^1, \ldots, x^l)^\top$ remain, where $u^i \approx u(t_i)$ and $x^i \approx x(t_i)$.

A simple approach to approximate the integral of the objective function between two grid points t_i and t_{i+1} is given by

$$\int_{t_i}^{t_{i+1}} f_0(x(t), u(t))\, dt \approx (t_{i+1} - t_i) f_0(x^i, u^i).$$

If the system of differential equations (4.6) is solved with the *Euler's method* the OCP can be be expressed in a discretised form.

Definition 4.17 (Discretised Optimal Control Problem) *With $h_i := t_{i+1} - t_i$, $i = 1, \ldots, j-1$ and free parameters $(u^i)_{i=1,\ldots,l}$ for the control as well as $(x^i)_{i=1,\ldots,l}$ for the states the discretised optimal control problem is given as*

$$\begin{aligned} \min_{x,u,p} \quad & \Phi(x^j) + \sum_{i=1}^{j-1} h_i f_0(x^i, u^i) \\ \textit{subject to} \quad & x^{i+1} = x^i + h_i f(x^i, u^i), \quad i = 1, \ldots, j-1, \\ & \xi(x^1, x^j) = 0, \\ & g(x^i, u^i) \leq 0, \quad i = 1, \ldots, j. \end{aligned} \tag{4.8}$$

Grouping the discretised variables x and u as well as the parameters p as an optimization variable $z = (x, u) \in \mathbb{R}^{n_x + n_u}$ yields an NLP problem as characterised in Definition 4.1 which can be solved with the previous described NLP solver WORHP.

The system dynamics can be integrated using common methods like the Euler's method, the Trapezoidal or the Hermite-Simpson method. For example, the Trapezoidal method can be denoted as

$$0 = x^{i+1} - x^i - \frac{h_i}{2}(f_i + f_{i+1})$$

with $f_i = f(x^i, u^i)$, $i = 1, \ldots, l$.

If the objective functional is of form of the Bolza problem or the Lagrange problem as mentioned in remark 4.16, the Lagrange term f_0 needs to be integrated. This can also be done by the methods described previously. When using the Trapezoidal method, the objective function is given by

$$I[x, u] = \Phi(x^l) + \sum_{i=1}^{l-1} \frac{h_i}{2}(f_0^i + f_0^{i+1})$$

with $f_0^i := f_0(x^i, u^i)$, $i = 1, \ldots, l$.

By transforming the optimal control problem (4.7) to the discretised problem (4.8) solutions are only available at the grid points. To estimate solutions between two grid points, the solutions is interpolated. For further details refer to [40] or [43].

TransWORHP

The library TransWORHP (Transcription for WORHP) is designed and developed by the Centre of Industrial Mathematics of the University of Bremen to solve optimal control problems. It discretises the optimal control problem and provides the arising optimization problem to WORHP (see section 4.1.1).
TransWORHP can work with optimal control problems in form of the Bolza problem where the Lagrange term is then integrated seperately. As integration methods the Euler's method, Trapezoidal and Hermite-Simpson method is available. The optimization process can be observed on a user interface.

This library is used to examine a controlled re-entry onto Earth and Mars.

4.2 Optimal Control of the Three State Model

To model controlled re-entry the three state model is extended by a control function $u(t) \in \mathbb{R}$. This extension is made in the flight path angle which leads to a controllable FPA γ_u of the re-entry vehicle and influences altitude h and velocity v indirectly

$$\dot{\gamma_u} = \left(\frac{\rho(h)}{2B_c} \frac{C_L}{C_D} v + \cos\gamma_u \left(\frac{v}{R_0 + h} - \frac{g}{v} \right) \right) + u. \tag{4.9}$$

Hereby the optimal control problem of controlled re-entry optimising the descent time for $t \in [0, t_f]$ yields to

$$\begin{aligned} \min_{x,t_f} \quad & t_f \\ \text{subject to} \quad & \dot{x} = \begin{pmatrix} \dot{h} \\ \dot{v} \\ \dot{\gamma_u} \end{pmatrix} \\ & h(0) = h_0, \ h(t_f) = 0 \\ & v(0) = v_0 \\ & \gamma_u(0) = \gamma_{u,0} \\ & 0 \leq h \leq h_0 \\ & 0 \leq v \leq v_0 \\ & \gamma_{u,\min} \leq \gamma_u \leq \gamma_{u,\max} \\ & u_{\min} \leq u \leq u_{\max} \end{aligned} \tag{4.10}$$

The box constraints of the flight path angle γ_u are set as

$$-90^\circ \leq \gamma_u \leq 90^\circ.$$

In contrast, the box constraints for the states h and v depend on the initial conditions, which are chosen as

$$\begin{aligned} h_0 &= 80\text{km}, \\ v_0 &= 3.5 \frac{\text{km}}{\text{s}}, \\ \gamma_u &= -2^\circ. \end{aligned}$$

Taken the manoeuvrability of the Space Shuttle into account the box constraints for the control are chosen as $u = \pm 0.1^\circ$ and $u = \pm 1.0^\circ$.

The optimal control problem 4.10 is examined for Earth and Mars for lift-to-drag ratios of $\frac{C_L}{C_D} = 0.3$ and $\frac{C_L}{C_D} = 1.0$ with a ballistic coefficient $B_C = 72.8 \frac{\text{kg}}{\text{m}^2}$. In table 4.1 the optimized end times of re-entry are gathered.

	$c_L/c_D = 0.3$		$c_L/c_D = 1.0$	
	$u = \pm 0.1°$	$u = \pm 1.0°$	$u = \pm 0.1°$	$u = \pm 1.0°$
Erde	626.8s	598.4s	1140.9s	1039.9s
Mars	741.8s	358.7s	2044.6s	2167.7s

Table 4.1: Descent times for Earth and Mars with oscillating control.

At the top of figures 4.3 to 4.6 the optimized trajectories for the above mentioned cases are displayed. Especially in figures 4.4 and 4.5 it is observable that the controlled flight path angle is exposed to unrealistic changes. Hence, this oscillating control needs to be smoothed. This is obtained by a regularization term

$$\kappa \|u(t)\|_2^2 = \kappa \int_0^{t_f} u^2(t)\, dt, \quad \kappa > 0 \tag{4.11}$$

which is added to the objective function. With this term the discontinuous oscillating control is smoothed and the optimal control problem in (4.10) becomes

$$\min_{x,t_f} \quad t_f + \kappa \int_0^{t_f} u^2(t)\, dt. \tag{4.12}$$

The dynamics, box constraints and boundary constraints remain unchanged.
The weighting factor κ influences the smoothness of the control u. The greater κ the more importance is laid on the smoothness of the control and the less importance is laid onto the minimization of the descent time t_f. Figure 4.2 gives an idea of how to choose the weighting factor κ, to find a balance between minimising the descent time t_f and smoothing the control $u(t)$.

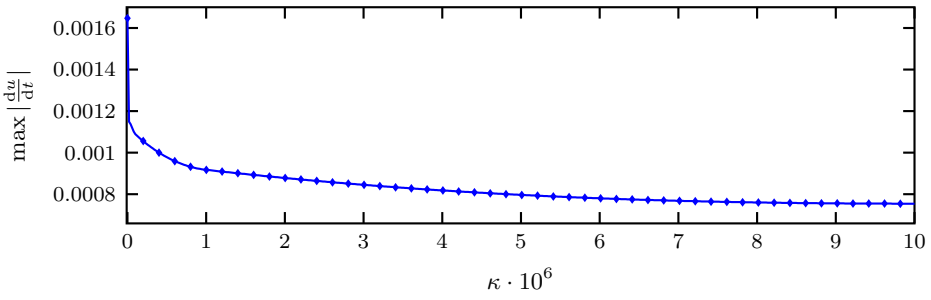

Figure 4.2: Influence of the weighting factor κ on the control $u(t)$.

With a suitable weighting factor κ the descent times of the re-entry onto Earth and Mars change in comparison to the times obtained by the oscillating control, see table 4.2. Compared to the descent times in case of the oscillating control it is conspicuous that these are not as minimal and only somewhat lower than in the uncontrolled case. This is due to the weighting factor.

	$c_L/c_D = 0.3$		$c_L/c_D = 1.0$	
	$u = \pm 0.1°$	$u = \pm 1.0°$	$u = \pm 0.1°$	$u = \pm 1.0°$
Erde	628.26s	628.36s	1152.88s	1152.83s
Mars	810.94s	809.62s	2190.07s	2200.29s

Table 4.2: Descent times for Earth and Mars with smoothed control.

At the bottom of figures 4.3 to 4.6 the optimized trajectories using the smoothed control for re-entry onto Earth and Mars are presented.

The box constraints for the control $u(t)$ can be varied even further. Examinations for $u = [\pm 10°, \pm 45°, \pm 90°]$ can be found in appendix B.1. Likewise, the optimization of the six state model can be found in appendix C.2.

In table 4.3 all technical details of the optimization using TransWORHP can be found for the case of re-entry onto Mars. All calculations were performed on a computer with the operating system Linux Ubuntu 16.04 utilised with an i7 3.4GHz processor.

	Number of					
$u(t)$	grid points	variables	box constraints	path constraints	iterations	CPU time
oscillating	101	405	801	300	91	38s
smoothed	101	405	801	300	504	211.1s

Table 4.3: Technical details of the optimization using TransWORHP for the case of re-entry onto Mars with $\frac{C_L}{C_D} = 0.3$.

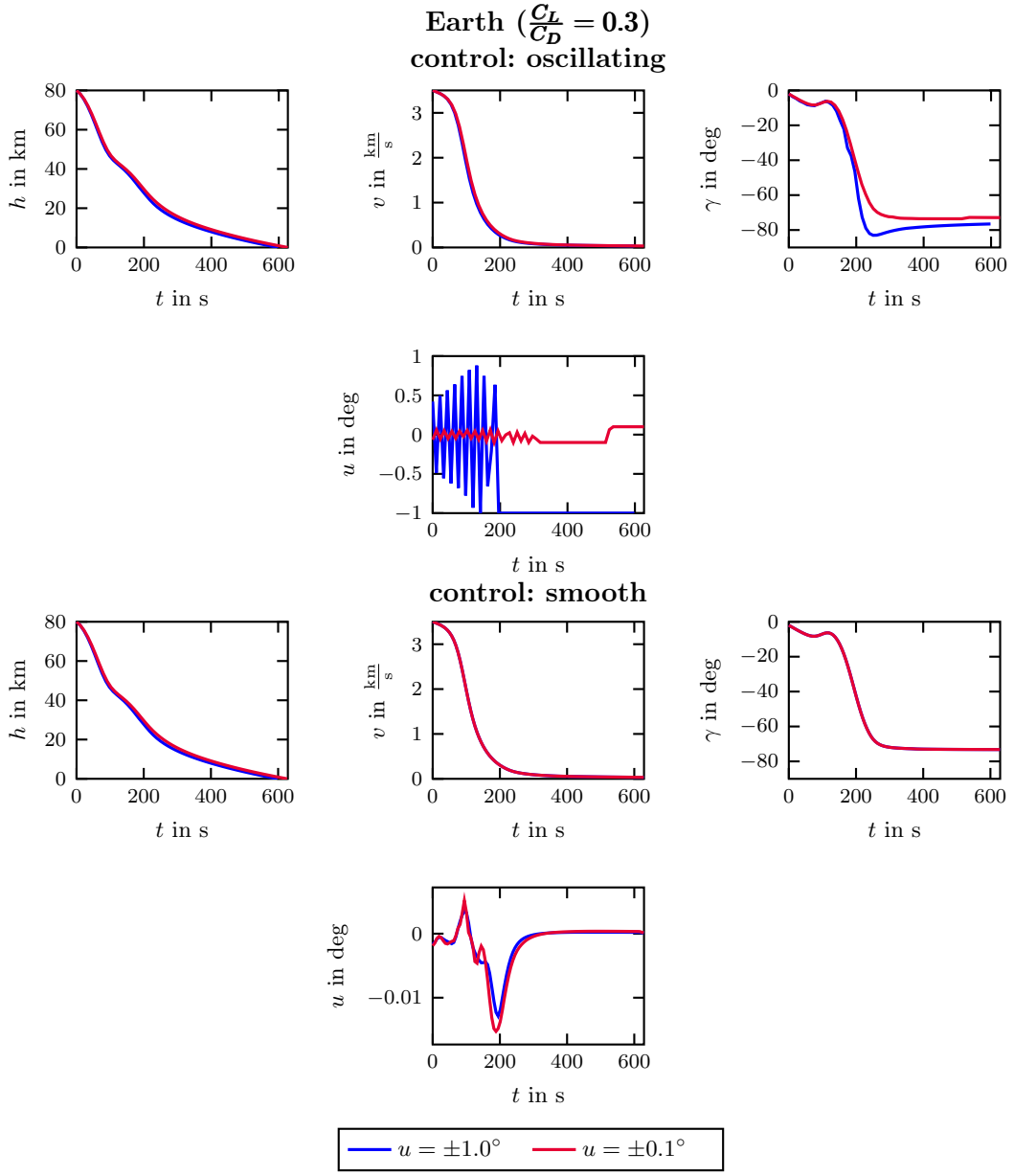

Figure 4.3: Controlled re-entry onto Earth with the aerodynamic parameters $B_C = 72.8 \frac{\text{kg}}{\text{m}^2}$ and $\frac{C_L}{C_D} = 0.3$.

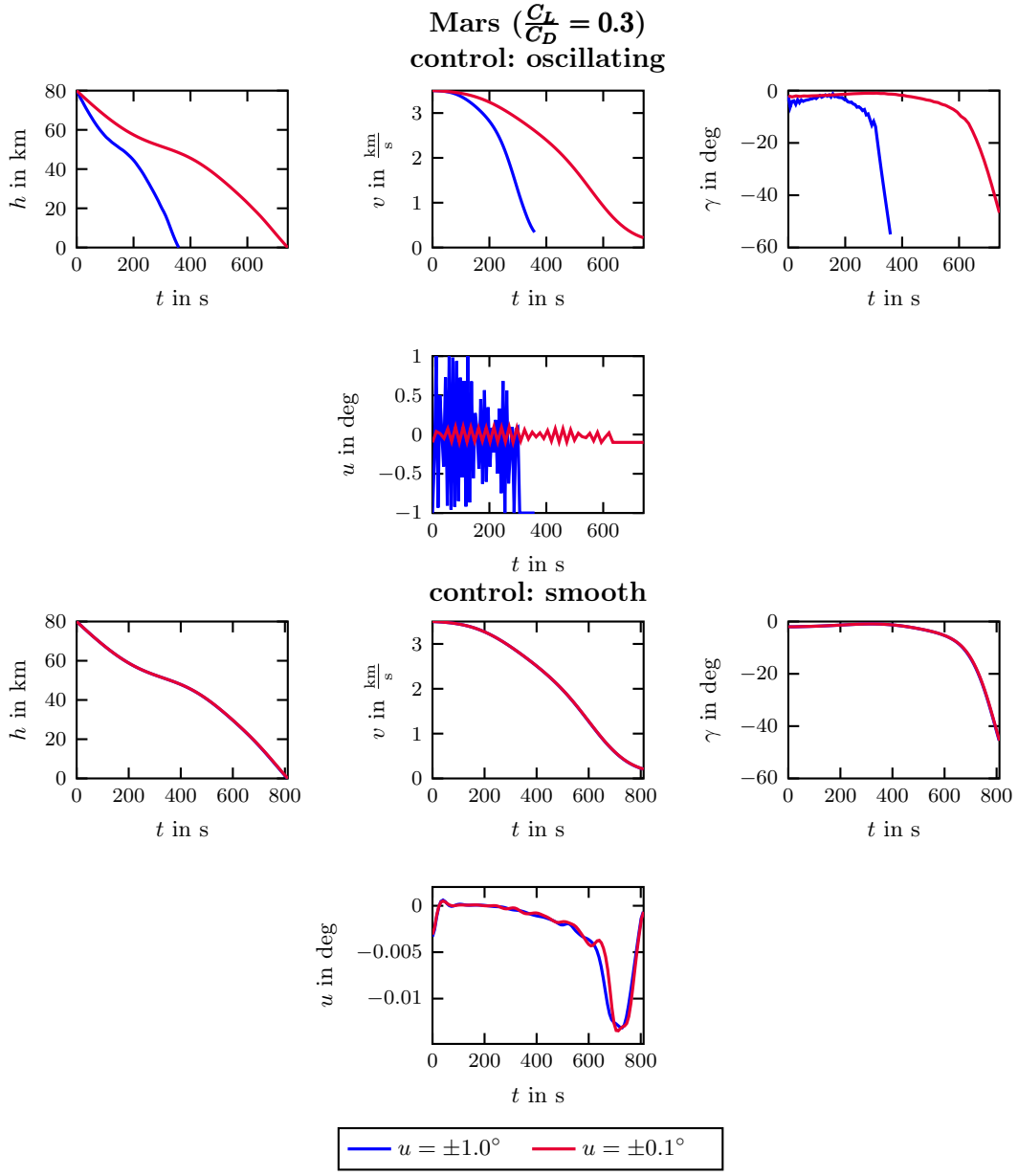

Figure 4.4: Controlled re-entry onto Mars for the aerodynamic parameters $B_C = 72.8 \frac{\text{kg}}{\text{m}^2}$ and $\frac{C_L}{C_D} = 0.3$.

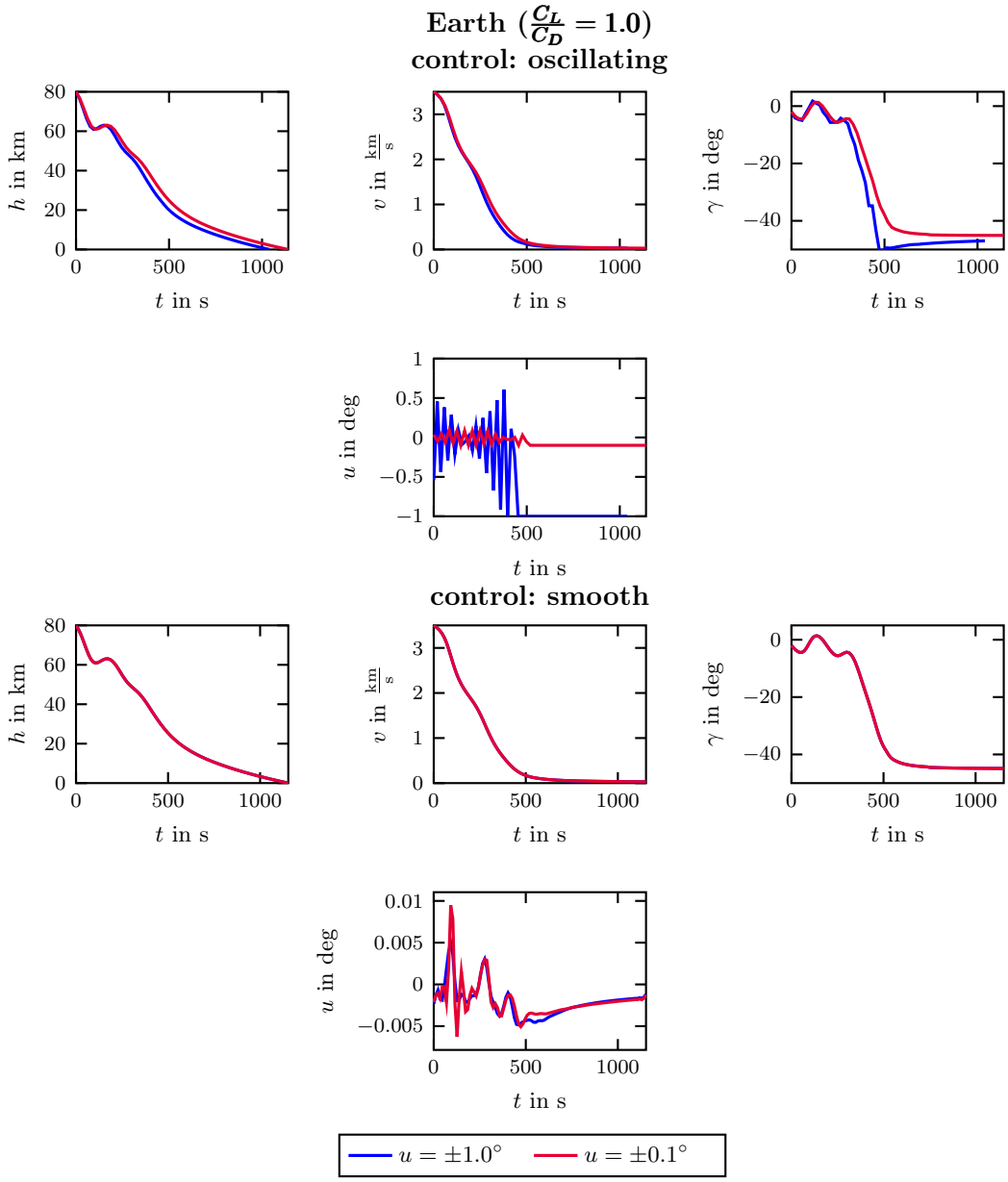

Figure 4.5: Controlled re-entry onto Earth with the aerodynamic parameters $B_C = 72.8 \frac{\text{kg}}{\text{m}^2}$ and $\frac{C_L}{C_D} = 1.0$.

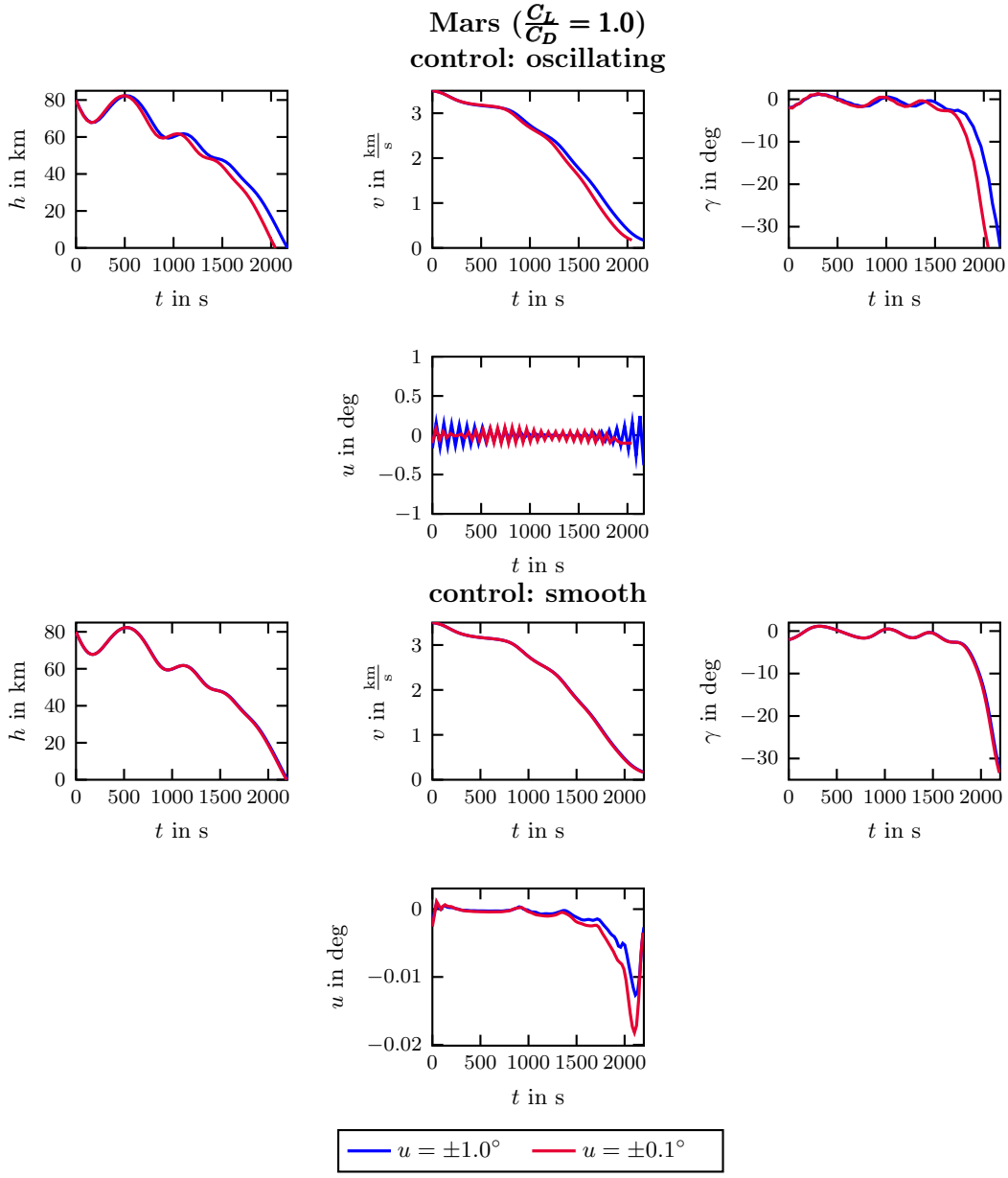

Figure 4.6: Controlled re-entry onto Mars for the aerodynamic parameters $B_C = 72.8 \frac{\text{kg}}{\text{m}^2}$ and $\frac{C_L}{C_D} = 1.0$.

4.3 Uncertainty Dispersion Analysis of Optimized Trajectories

To analyse the temporal evolution of uncertainties in case of controlled re-entry onto Earth and Mars, trajectories are generated for 5% dispersion in the initial conditions. This set of trajectories is used to estimate the temporal evolution of the PDFs. The PDFs are obtained using the Stochastic Liouville Equation introduced in section 3.2. From the PDFs, a most probable trajectory is derived afterwards.

4.3.1 Temporal Evolution of the PDF

In figure 4.9 the estimated PDFs for Earth and Mars with $u = \pm 1.0$ are presented for three consecutive time steps t_0, t_{mid} and t_f. To evaluate the PDFs the mean descent time is estimated from the descent times of the set of optimized trajectories. The optimized descent times for each set of initial conditions are shown table 4.4.

	Initial conditions							
$\boldsymbol{h_0}$	68km	72km	76km	80km	84km	88km	92km	**Mean**
$\boldsymbol{v_0}$	$2.975\frac{\text{km}}{\text{s}}$	$3.1505\frac{\text{km}}{\text{s}}$	$3.325\frac{\text{km}}{\text{s}}$	$3.5\frac{\text{km}}{\text{s}}$	$3.675\frac{\text{km}}{\text{s}}$	$3.85\frac{\text{km}}{\text{s}}$	$4.025\frac{\text{km}}{\text{s}}$	**end**
$\boldsymbol{\gamma_{u,0}}$	$-2.3°$	$-2.2°$	$-2.1°$	$-2.0°$	$-1.9°$	$-1.8°$	$-1.7°$	**time**
Erde	663.73	555.22	574.81	628.36	638.02	605.36	659.32	612.59
Mars	482.89	566.80	612.89	809.62	1200.91	1592.21	1983.50	1011.83

Table 4.4: End times t_f in seconds of the set of optimized trajectories for re-entry onto Earth and Mars and mean end time.

Observing the temporal evolution of the PDFs in figure 3.13 and 3.14 compared to the PDFs in figure 4.9 it stands out that in case of controlled re-entry all trajectories end at $h = 0$km. This is due to the end condition $h(t_f) = 0$. When examining the most probable trajectory in section 4.3.2 this behaviour becomes more apparent.

The absolute error of the PDFs concerning the normalisation condition is shown in figure 4.7. Regarding Mars, the error is of same magnitude as for the PDFs of the re-entry in section 3.3.3. The same holds for the error in case of Earth. Nevertheless, the error is dramatically larger, which is caused by numerical instabilities in the dynamics, especially in the atmosphere model, as pointed out before.

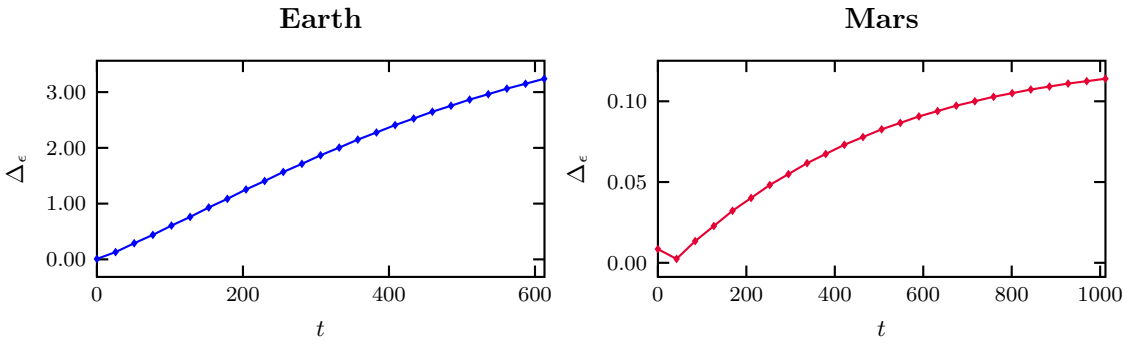

Figure 4.7: Absolute error of the violation of the normalisation condition of the PDF of the optimized trajectories for box constraints $u = 1.0°$ for Earth and Mars.

4.3.2 Most Probable Trajectory

As introduced in section 3.4 a most probable trajectory can be estimated from the PDFs. The most probable trajectory for the optimized re-entry onto Earth and Mars is displayed in figure 4.8. As explained the descent times of each set of initial conditions is averaged to find the most probable trajectory.

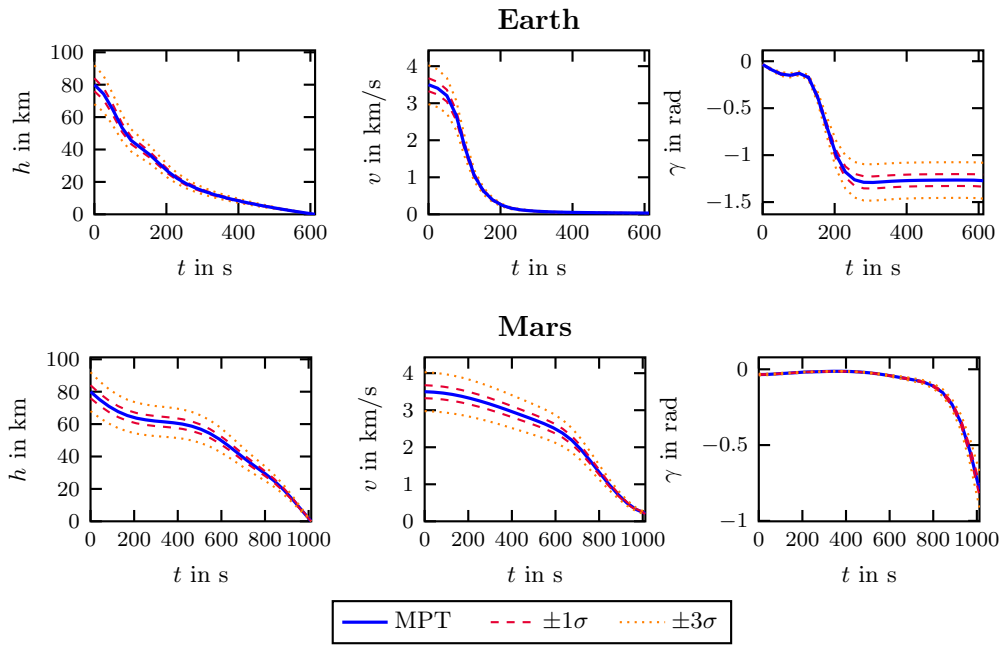

Figure 4.8: Most probable trajectory of optimized trajectories with box constraints $u = \pm1.0°$ for re-entry onto Earth (top) and Mars (bottom) with 5% uniform dispersion in v_0, h_0 and γ_0 respectively.

Compared to the MPT of the uncontrolled re-entry onto Mars in figure 3.16 it occures that due to the controllability the vehicle reaches the ground and is not skipping

off of the atmosphere. The same applies to the most probable trajectory of the controlled re-entry onto Earth. In this case, it is also possible to reach the ground due to the end condition $h(t_f) = 0$.

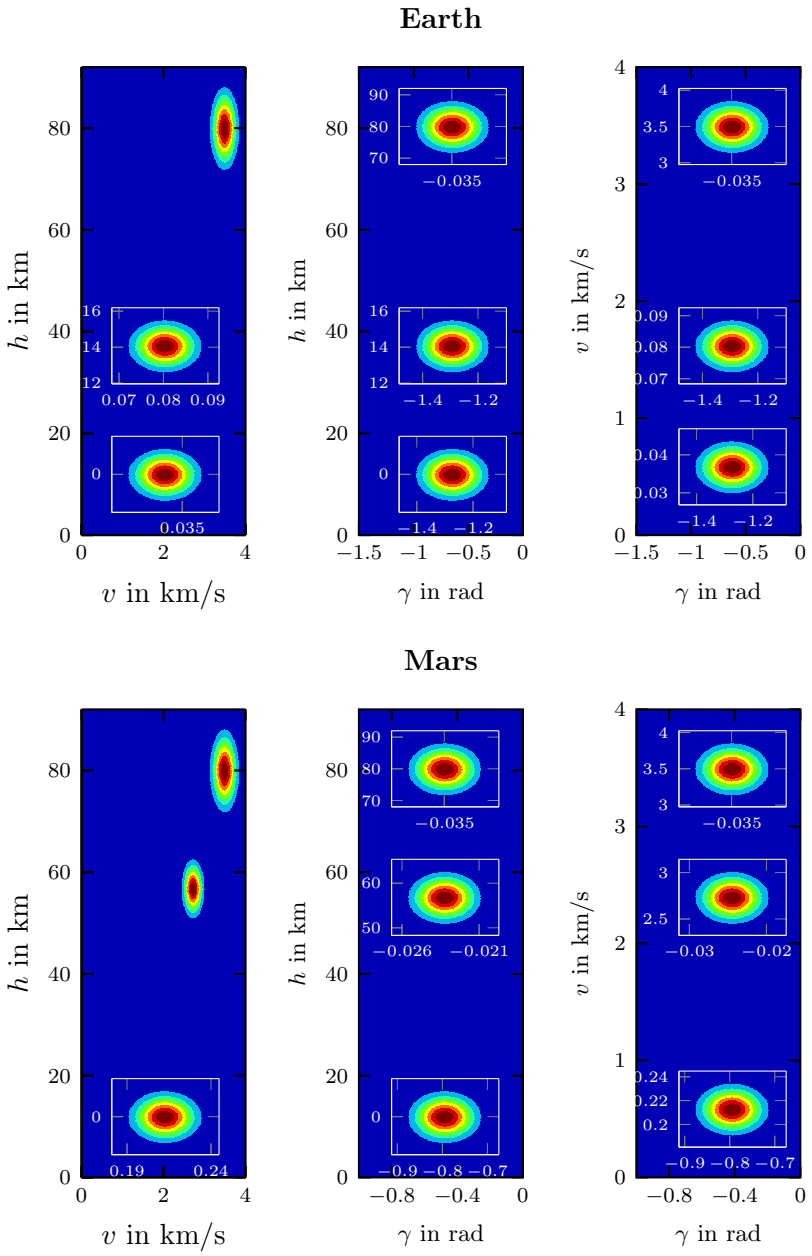

Figure 4.9: Temporal evolution of the PDF for optimized re-entry trajectories of Earth (top) and Mars (bottom) for 5% uniform dispersion in h_0, v_0 and γ_0 with a control $u = \pm 1.0°$. The PDFs are taken at time steps $t_0 = 0$s, $t_{mid} = 306$s and $t_f = 612$s for Earth. For Mars the time steps are $t_0 = 0$s, $t_{\text{mid}} = 506$s and $t_f = 1012$s.

Chapter 5

Conclusion

5.1 Summary

This thesis presented the numerical temporal evolution of the *Stochastic Liouville Equation* as an alternative to the computationally expensive *Monte-Carlo* analysis for the examination of the uncertainty dispersion of atmospheric re-entry onto Earth and Mars. Therefore, the thesis started off with the re-entry problem itself. The environment in which the re-entry takes place was modelled and the aerodynamic characteristics were explained. Two re-entry models, the three state and the six state model, were introduced and resulting trajectories for different aerodynamic properties of the re-entry vehicle and different initial conditions were presented.

The next chapter was dedicated to the uncertainty analysis. This analysis was based on the temporal evolution of probability density functions. Thus, the necessary fundamentals in stochastics were sum up before the *Stochastic Liouville Equation* was derived. On the basis of a first one-dimensional example the analytical and numerical implementation was illustrated. Afterwards the uncertainty analysis was performed for different re-entry cases increasing in complexity for Earth and Mars, which led to multidimensional probability densities for each time step. From the maxima of the probability density functions at each time step most probable trajectories and additionally 1-σ and 3-σ error bars were generated giving an impression of the influence of the uncertainties in the initial conditions.
Since the probability density functions govern all stochastical moments, it was possible to deduce the covariance matrices as first-order approximations. Using these matrices, the procedure to estimate error ellipses was demonstrated. These ellipses govern the landing dispersions for the re-entry if evaluated at the end time of the descent. At every other time step these matrices govern the dispersion during the descent.

After all, a re-entry vehicle is usually manoeuvrable and it was necessary to discuss the case of controlled re-entry. When speaking of controllability of a re-entry vehicle one aims for the optimal re-entry trajectory concerning the minimal descent time or if modelled

the minimal heating of the vehicle. Accordingly, the fundamentals in optimization and optimal control were laid out before the analysis of the controlled re-entry. The vehicle in this case, was controllable in its flight path angle and the trajectories were optimized subjected to the descent time. Using the libraries WORHP and TransWORHP a set of optimal trajectories was generated, which was afterwards analysed using the before introduced Stochastic Liouville Equation.

5.2 Evaluation of Results

Evaluating the results of the previous chapters show that the Stochastic Liouville Equation is an efficient way to analyse not only re-entry dynamics concerning the influence of uncertainties. This equation directly yields probability density functions for every time step showing the temporal evolution of uncertainties.

The first examination of ballistic re-entry gave a good feeling for the influences of the initial conditions and the aerodynamic coefficients on the re-entry trajectory. In contrast, the controlled re-entry avoided skipping off of the atmosphere which was caused by a poor choice of initial conditions. Regardless of which constellation of initial conditions and aerodynamic coefficients the re-entry was successful when considering controlled re-entry and optimizing the trajectory subject to the descent time.
Comparing the results of the uncertainty analysis of controlled and ballistic re-entry onto Earth and Mars it is noticable that for both cases the range of the dispersions decrease with time. The main difference between the controlled and ballistic re-entry is that for controlled re-entry all trajectories end at $h(t_f) = 0$km due to the choice of the end conditions. In table 5.1 the 1-σ neighbourhood of the uncontrolled re-entry onto Mars for 1% uniform dispersion on the initial conditions is displayed for the final time t_f is shown exemplarily.

	-1σ	MPT	$+1\sigma$
$\boldsymbol{h}$ in km	0.0532	0.0537	0.0542
$\boldsymbol{v}$ in $\frac{\text{km}}{\text{s}}$	0.262	0.265	0.268
$\boldsymbol{\gamma}$ in deg	-45.98	-45.52	-45.07

Table 5.1: Resulting 1-σ neighbourhood of Mars for 1% uniform dispersion in the initial conditions at the end time $t_f = 840$s.

Altogether, the uncertainty analysis performed in this thesis is not only computationally efficient but gives a good impression on the influences of uncertainties in the initial conditions throughout the descent. A deeper insight would be given by analysing the re-entry system dynamics regarding the influence of uncertainties in the atmosphere model as well as the aerodynamics coefficients.

5.3 Future Work

The re-entry dynamics examined in this thesis do not reproduce the complete re-entry, descent and landing. The used dynamics modelled ballistic re-entry without the final touchdown and were adapted to illustrate the controlled re-entry. For a real reproduction of the overall re-entry, descent and landing further improvements would be necessary.

To model the re-entry more realistically it would be advantageous to include the heating of the re-entry vehicle due to the friction with the atmosphere into the model. In particular, during the controlled re-entry high heating loads which a re-entry vehicle could not withstand would occur due to the minimization of the descent time. This would necessitate the investigation of objective functions minimizing the heating loads in addition to the descent time.

Besides the heating, the re-entry would also be more accurately modelled when including the deceleration mechanisms, parachutes and descent thrusters, for the last approximately 10km into the model. Even if the uncertainties have a main impact in the initial conditions, modelling the whole sequence of re-entry, descent and landing would give a complete impression of the final and most critical mission phase.

Further investigations in the controlled re-entry are possible especially concerning the realization of the manoeuvrability of the re-entry vehicle. It could be conceivable that the vehicle changes its aerodynamic properties during the descent resulting in changes in the trajectory. For example the *Hypersonic Inflatable Aerodynamic Decelerator* (HIAD) [60], see figure 5.1, is a flexible re-entry vehicle developed by NASA.

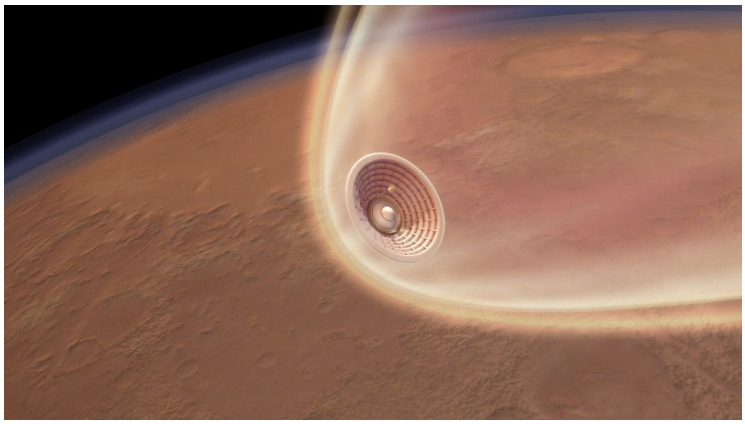

Figure 5.1: The Hypersonic Inflatable Aerodynamic Decelerator (HIAD) controls its trajectory by changing its shape [60].

This vehicle controls its trajectory by changing its shape leading to changes in the aerodynamic properties of the vehicle. It is an inflatable aeroshell designed to enable high mass exploration missions and stowage in a compact space. Compared to rigid re-entry

vehicles this inflatable and flexible design provides the needed decelerations at higher altitude and velocities. See [59] and [60] for further details.

Summing up, the re-entry problem and the investigations of the influence of uncertainties is not only highly relevant when returning to Earth but also for the exploration of other planets and hence, is still a broad field of research.

Appendix A

Planetary Data

A.1 Orbital and Bulk Parameters

In the following table A.1, all in this thesis necessary planetary parameters are collected.

	Unit	**Mars**	**Earth**
Mass	$[10^{24}\text{kg}]$	0.64171	5.9724
Radius	[km]	3396.2	6378.1
GM	$[10^{6}\text{km}^3/\text{s}^2]$	0.042828	0.39860
Siderial rotation period	[h]	24.6229	23.9345
Rotational angular velocity[1]	$[^\circ/\text{s}]$	0.00406	0.0042

Table A.1: Needed planetary facts of Earth and Mars [47]

A.2 Atmosphere Models

The atmosphere models used in this thesis are presented and explained in detail below.

Earth

The first model which is used to model the atmosphere of Earth is the Earth Atmosphere Model (EAM) developed by NASA Glenn Research Centre, see [52]. This model assumes that the atmospheric pressure and temperature change only with altitude. The atmospheric density ρ can then be calculated from temperature T and pressure P.

$$\rho = \frac{P(T)}{0.2869 \cdot (T(h) + 273.1)} \tag{A.1}$$

[1] calculated from siderial rotation period as mentioned in [48]

In this case the atmosphere is separated into three layers, with different relations of temperature and pressure.

$$\begin{aligned} &h < 11000 \text{ m} \qquad \text{(Troposphere)} \\ &\quad T(h) = 15.04 - 6.49 \cdot 10^{-3} h \\ &\quad P(T) = 101.29 \cdot \left(\frac{T(h) + 273.1}{288.08} \right)^{5.256} \end{aligned} \tag{A.2}$$

$$\begin{aligned} &11000 \text{ m} < h < 25000 \text{ m} \qquad \text{(Lower Stratosphere)} \\ &\quad T(h) = -56.46 \\ &\quad P(T) = 22.65 \cdot e^{1.73 - 1.57 \cdot 10^{-4} h} \end{aligned} \tag{A.3}$$

$$\begin{aligned} &h > 25000 \text{ m} \qquad \text{(Upper Stratosphere)} \\ &\quad T(h) = -131.21 + 2.99 \cdot 10^{-3} h \\ &\quad P(T) = 2.488 \cdot \left(\frac{T(h) + 273.1}{216.6} \right)^{-11.388} \end{aligned} \tag{A.4}$$

This equations were developed from a curve fit over averaged atmospheric measurements representing an average day on Earth.

The atmosphere models US Standard Atmosphere 1976 (US76) and MSISE-00 by the US Naval Research Laboratory are only given as data sets, see table A.2.

Mars

The first atmosphere model of Mars is given in [19]. It states that the atmospheres of Mars, Venus and Titan can be approximated with the equation

$$\rho(h) = \rho_0 \exp\left(\frac{h_2 - h}{h_1} \right). \tag{A.5}$$

In case of Mars the parameters are set as $h_1 = 9.8\text{km}, h_2 = 20\text{km}$ and $\rho_0 = 0.0019 \frac{\text{kg}}{\text{m}^3}$. In this thesis this model is refered as the model by Noton.

The second model of Mars' atmosphere is the Mars Atmosphere Model (MAM) developed by NASA Glenn Research Centre, see [49]. Likewise, this model depends on atmospheric pressure and temperature which each depend on the altitude.

$$\rho = \frac{P(T)}{0.1921 \cdot (T(h) + 273.1)} \tag{A.6}$$

(A.7)

The Martian atmosphere can be separated into two layers which results in different equations for each layer.

$$h < 7000 \text{ m}$$
$$\begin{aligned} T(h) &= -31 + 9.98 \cdot 10^{-4} \cdot h \\ P(T) &= 0.699 \cdot e^{-9 \cdot 10^{-5} h}. \end{aligned} \tag{A.8}$$

$$h > 7000 \text{ m}$$
$$\begin{aligned} T(h) &= -23.4 - 2.22 \cdot 10^{-3} h \\ P(T) &= 0.699 \cdot e^{-9 \cdot 10^{-5} h} \end{aligned} \tag{A.9}$$

These equations were developed from measurements made by the Mars Global Surveyor from April 1996.

The Mars Global Reference Model (GRAM) is given as data sets, see table A.3.

US76		**MSISE-00**	
Altitude in km	Density in $\frac{\text{kg}}{\text{m}^3}$	Altitude in km	Density in $\frac{\text{g}}{\text{cm}^3}$
0	1.22500	0.0	$1.293 \cdot 10^{-3}$
1.000	1.11164	5.0	$7.517 \cdot 10^{-4}$
2.000	1.00649	10.0	$3.984 \cdot 10^{-4}$
3.000	$9.09122 \cdot 10^{-1}$	15.0	$1.812 \cdot 10^{-4}$
4.000	$8.19129 \cdot 10^{-1}$	20.0	$8.273 \cdot 10^{-5}$
5.000	$7.36116 \cdot 10^{-1}$	25.0	$3.625 \cdot 10^{-5}$
6.000	$6.59697 \cdot 10^{-1}$	30.0	$1.555 \cdot 10^{-5}$
7.000	$5.89501 \cdot 10^{-1}$	35.0	$6.783 \cdot 10^{-6}$
8.000	$5.25168 \cdot 10^{-1}$	40.0	$3.149 \cdot 10^{-6}$
9.000	$4.66348 \cdot 10^{-1}$	45.0	$1.569 \cdot 10^{-6}$
10.000	$4.12707 \cdot 10^{-1}$	50.0	$8.284 \cdot 10^{-7}$
12.000	$3.10828 \cdot 10^{-1}$	55.0	$4.437 \cdot 10^{-7}$
15.000	$1.93674 \cdot 10^{-1}$	60.0	$2.329 \cdot 10^{-7}$
20.000	$8.80349 \cdot 10^{-2}$	65.0	$1.181 \cdot 10^{-7}$
25.000	$3.94658 \cdot 10^{-2}$	70.0	$5.765 \cdot 10^{-8}$
30.000	$1.80119 \cdot 10^{-2}$	75.0	$2.742 \cdot 10^{-8}$
35.000	$8.21392 \cdot 10^{-3}$	80.0	$1.303 \cdot 10^{-8}$
40.000	$3.85101 \cdot 10^{-3}$	85.0	$6.044 \cdot 10^{-9}$
45.000	$1.88129 \cdot 10^{-3}$	90.0	$2.682 \cdot 10^{-9}$
50.000	$9.77525 \cdot 10^{-4}$	95.0	$1.122 \cdot 10^{-9}$
60.000	$2.88321 \cdot 10^{-4}$	100.0	$4.339 \cdot 10^{-10}$
70.000	$7.42430 \cdot 10^{-5}$		
80.000	$1.57005 \cdot 10^{-5}$		
84.852	$6.95788 \cdot 10^{-6}$		

Table A.2: Atmosphere data of Earth [53, 54]

Mars - GRAM	
Altitude in km	Density in $\frac{\text{kg}}{\text{m}^3}$
2.172	$1.1873 \cdot 10^{-2}$
4.825	$9.5093 \cdot 10^{-3}$
7.408	$7.6223 \cdot 10^{-3}$
9.921	$6.1133 \cdot 10^{-3}$
12.365	$4.9003 \cdot 10^{-3}$
14.744	$3.9253 \cdot 10^{-3}$
17.062	$3.1383 \cdot 10^{-3}$
19.326	$2.5043 \cdot 10^{-3}$
21.540	$1.9953 \cdot 10^{-3}$
23.709	$1.5863 \cdot 10^{-3}$
25.838	$1.2593 \cdot 10^{-3}$
27.931	$9.9823 \cdot 10^{-4}$
29.992	$7.8913 \cdot 10^{-4}$
32.029	$6.2183 \cdot 10^{-4}$
34.048	$4.8813 \cdot 10^{-4}$
36.057	$3.8223 \cdot 10^{-4}$
38.061	$2.9913 \cdot 10^{-4}$
40.051	$2.3443 \cdot 10^{-4}$
42.039	$1.8373 \cdot 10^{-4}$
44.019	$1.4393 \cdot 10^{-4}$
45.987	$1.1293 \cdot 10^{-4}$
47.948	$8.8513 \cdot 10^{-5}$
49.888	$6.9463 \cdot 10^{-5}$
51.825	$5.4463 \cdot 10^{-5}$
53.720	$4.2893 \cdot 10^{-5}$
55.646	$3.3603 \cdot 10^{-5}$
57.546	$2.6363 \cdot 10^{-5}$

Table A.3: Atmosphere data of Mars GRAM [51]

Appendix B

Further Investigations of the Three State Model

B.1 Optimal Control with Larger Box Constraints

In figure B.1 optimized trajectories for controlled re-entry onto Earth and Mars are displayed utilising larger box constraints for the control $u(t)$. The initial conditions and coefficients are set as

$$\begin{aligned} h_0 &= 80\text{km}, \\ v_0 &= 3.5\frac{\text{km}}{\text{s}}, \\ \gamma_0 &= -2^\circ, \\ B_C &= 72.8\frac{\text{kg}}{\text{m}^2}, \\ \frac{C_L}{C_D} &= 0.3. \end{aligned}$$

In table B.1 the optimized descent times t_f are gathered.

	$u = \pm 10°$	$u = \pm 45°$	$u = \pm 90°$
Erde	621.56s	621.62s	621.65s
Mars	813.13s	592.7s	232.7s

Table B.1: Optimized decent times t_f for larger box constraints of the control u.

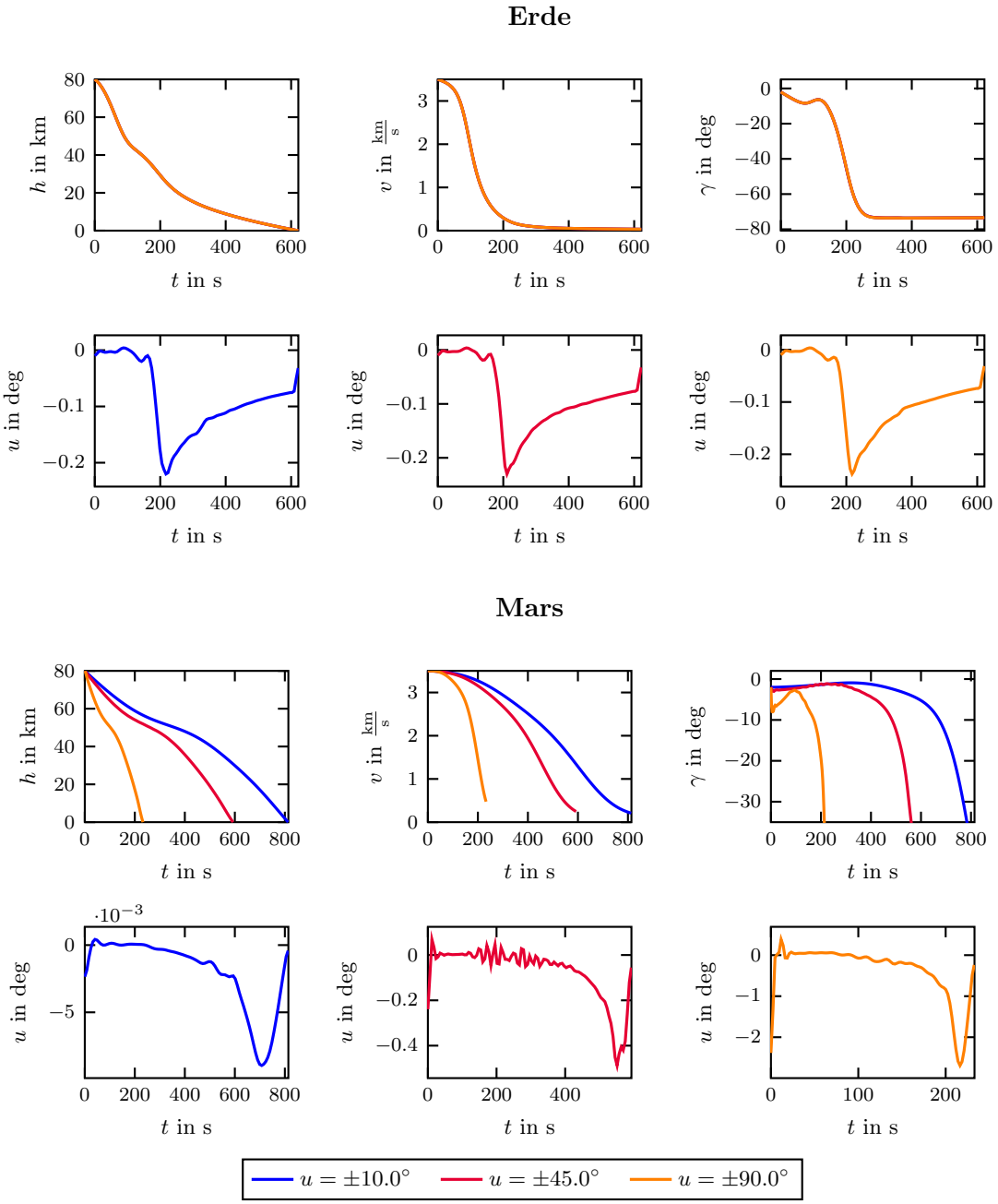

Figure B.1: Controlled Descent onto Earth (top) and Mars (bottom) for larger box constraints for the control u.

B.2 Uncertainty Dispersion Analysis of Optimized Trajectories

In figure B.4 the temporal evolution of uncertainties in the initial conditions of optimized trajectories of re-entry onto Earth and Mars is displayed. In this cases the control is constrainted to $u = \pm 0.1°$. The absolute error of the PDFs in each time step is displayed in figure 4.7. From the PDFs a most probable trajectory is estimated, see figure B.3.
For further explanations see section 4.3.

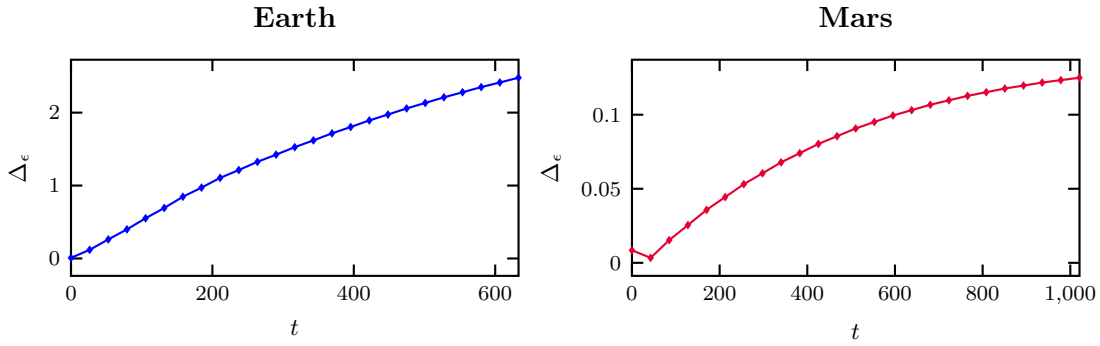

Figure B.2: Absolute error of the violation of the normalisation condition of the PDF of the optimized trajectories for box constraints $u = 0.1°$ for Earth and Mars.

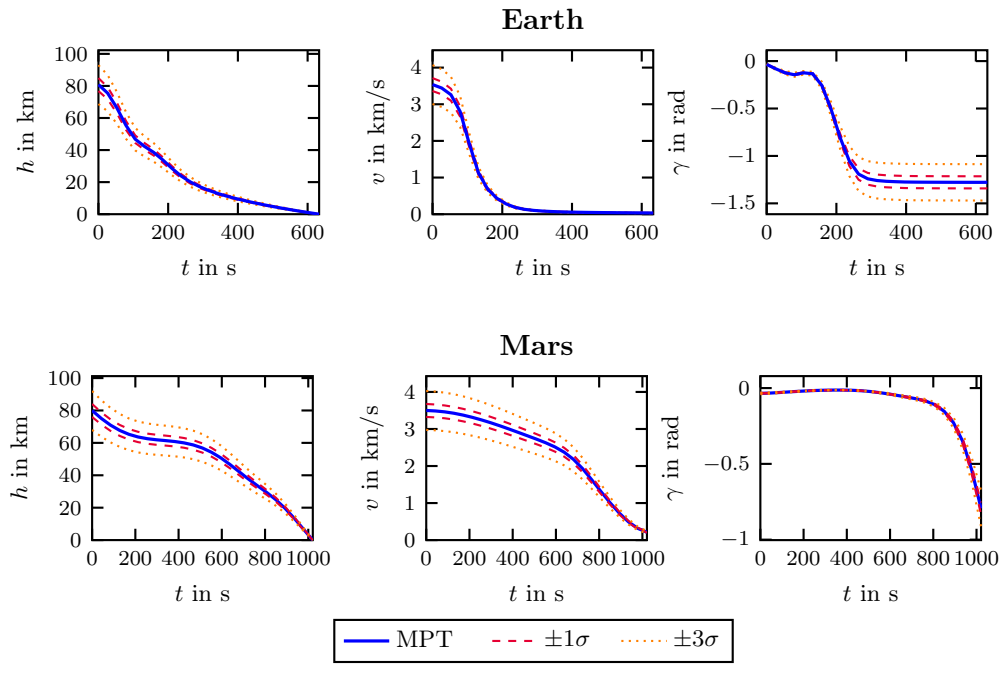

Figure B.3: Most probable trajectory of optimized trajectories with box constraints $u = \pm 0.1°$ for re-entry onto Earth (top) and Mars (bottom) with 5% uniform dispersion in v_0, h_0 and γ_0 respectively.

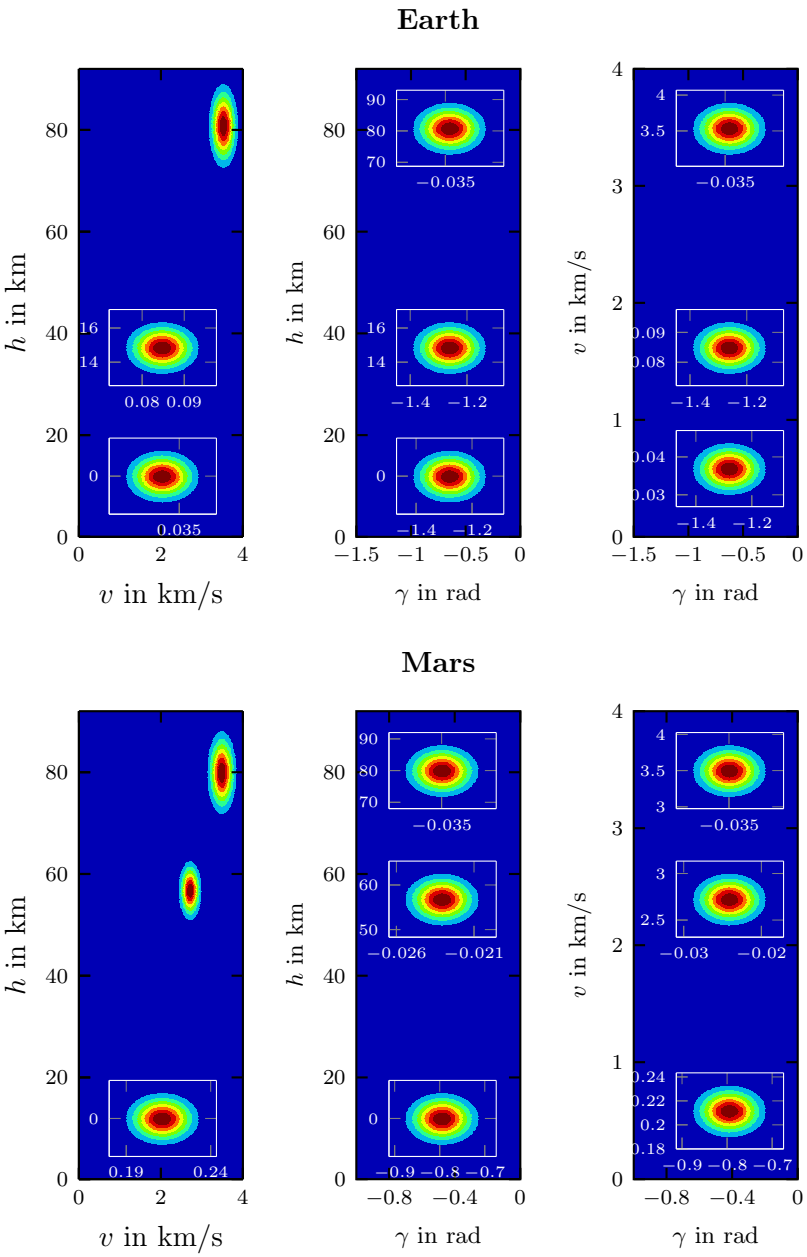

Figure B.4: Temporal evolution of the PDF for optimized re-entry trajectories of Earth (top) and Mars (bottom) for 5% uniform dispersion in h_0, v_0 and γ_0 with a control $u = \pm 0.1°$. For Earth the PDFs are taken at the time steps $t_0 = 0$s, $t_{mid} = 317$s and $t_{end} = 634$s. For Mars these time steps are $t_0 = 0$s,$t_{mid} = 510$s and $t_{end} = 1021$s

Appendix C

Six State Model

In this chapter the six state model as introduced in section 2.4.2 is investigated.

C.1 Re-Entry

For a descent on celestial bodies without atmosphere the dynamics of the six state model can be reduced to

$$\begin{aligned}
\dot{h} &= v \sin\gamma, \\
\dot{\theta} &= \frac{v \cos\gamma \cos\psi}{(R_0 + h)\cos\phi}, \\
\dot{\phi} &= \frac{v \cos\gamma \sin\psi}{(R_0 + h)}, \\
\dot{v} &= -g \sin\gamma + \omega^2 (R_0 + h)\cos\phi(\sin\gamma\cos\phi - \cos\gamma\sin\phi\sin\psi), \\
\dot{\gamma} &= \cos\gamma \left(\frac{v}{R_0 + h} - \frac{g}{v} \right), \\
\dot{\psi} &= -\frac{v\cos\gamma}{R_0 + h}\tan\phi\cos\psi + 2\omega(\tan\gamma\cos\phi\sin\psi - \sin\phi) - \frac{\omega^2(R_0 + h)}{v\cos\gamma}\sin\phi\cos\phi\cos\psi.
\end{aligned} \tag{C.1}$$

where $\rho(h) = 0$. In this case only the gravity is the operating force drawing the re-entry vehicle towards the planet. In figure C.1 the descent onto Earth and Mars without lift and drag of the atmosphere is shown exemplarily. The initial values for the states were set as

$$\begin{aligned}
h &= 80\text{km}, \\
\theta &= 341.03^\circ = 5.9521\text{rad}, \\
\phi &= 24.01^\circ = 0.4191\text{rad}, \\
v &= 3.5\frac{\text{km}}{\text{s}}, \\
\gamma &= -2^\circ = -0.0349\text{rad}, \\
\psi &= 0.0573^\circ = 0.0010\text{rad},
\end{aligned}$$

The radius of Earth and Mars are taken as stated in table A.1.

As seen in section 2.4.1, the vehicle landing on Earth hits the ground with a higher

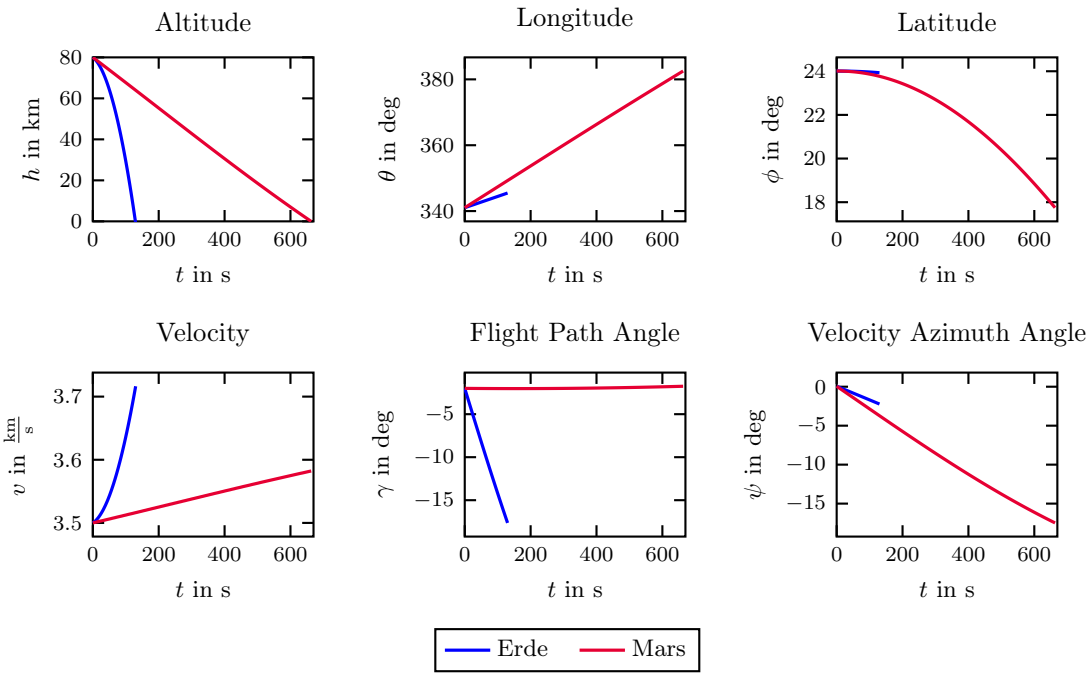

Figure C.1: Descent onto Earth and Mars without consideration of the atmospheres using the six state model.

velocity and after a shorter amount of time than the vehicle landing on Mars. The velocity of the vehicle increases since no aerodynamic forces interfere and thus it is not decelerating.

Again, this changes in the presence of drag and lift due to the atmosphere, see figure C.2. Varying the entry velocities shows, that for Mars the vehicle bounce off the atmosphere with a velocity $v_0 = 4.0\frac{\text{km}}{\text{s}}$, see figure C.3. In figure C.4 the aerodynamic parameters are varied. The descent times are the as mention in section 2.4.1 when simulating the three state model.

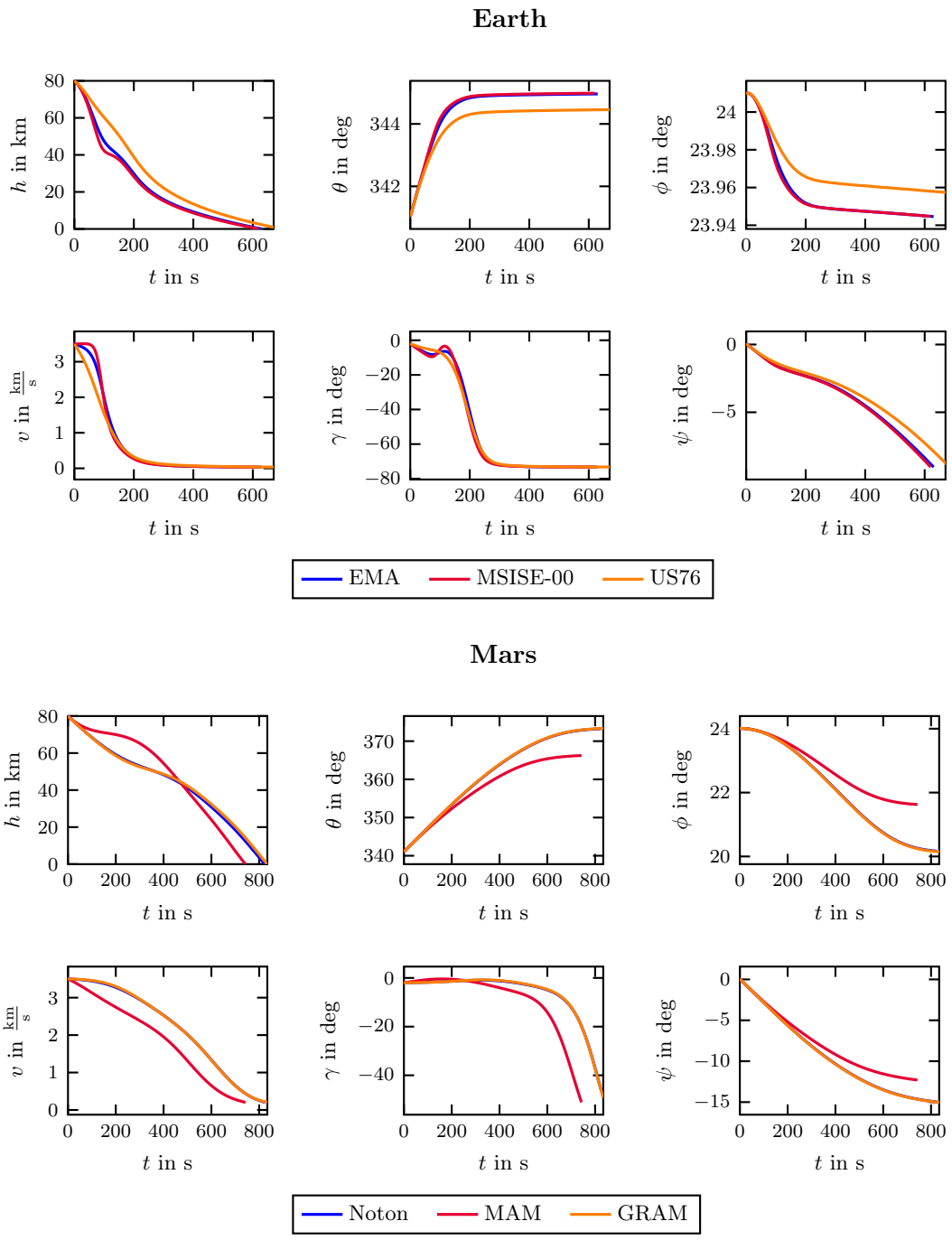

Figure C.2: Re-Entry onto Earth (top) and Mars (bottom) using the six state model. For each three different atmosphere models are used with the initial conditions $h_0 = 80\text{km}$, $\theta_0 = 341.03°$, $\phi_0 = 24.01°$, $v_0 = 3.5\frac{\text{km}}{\text{s}}$, $\gamma_0 = -2°$ and $\psi_0 = 0.05°$. The parameters are set as $B_C = 72.8\frac{\text{kg}}{\text{m}^2}$ and $\frac{C_L}{C_D} = 0.3$.

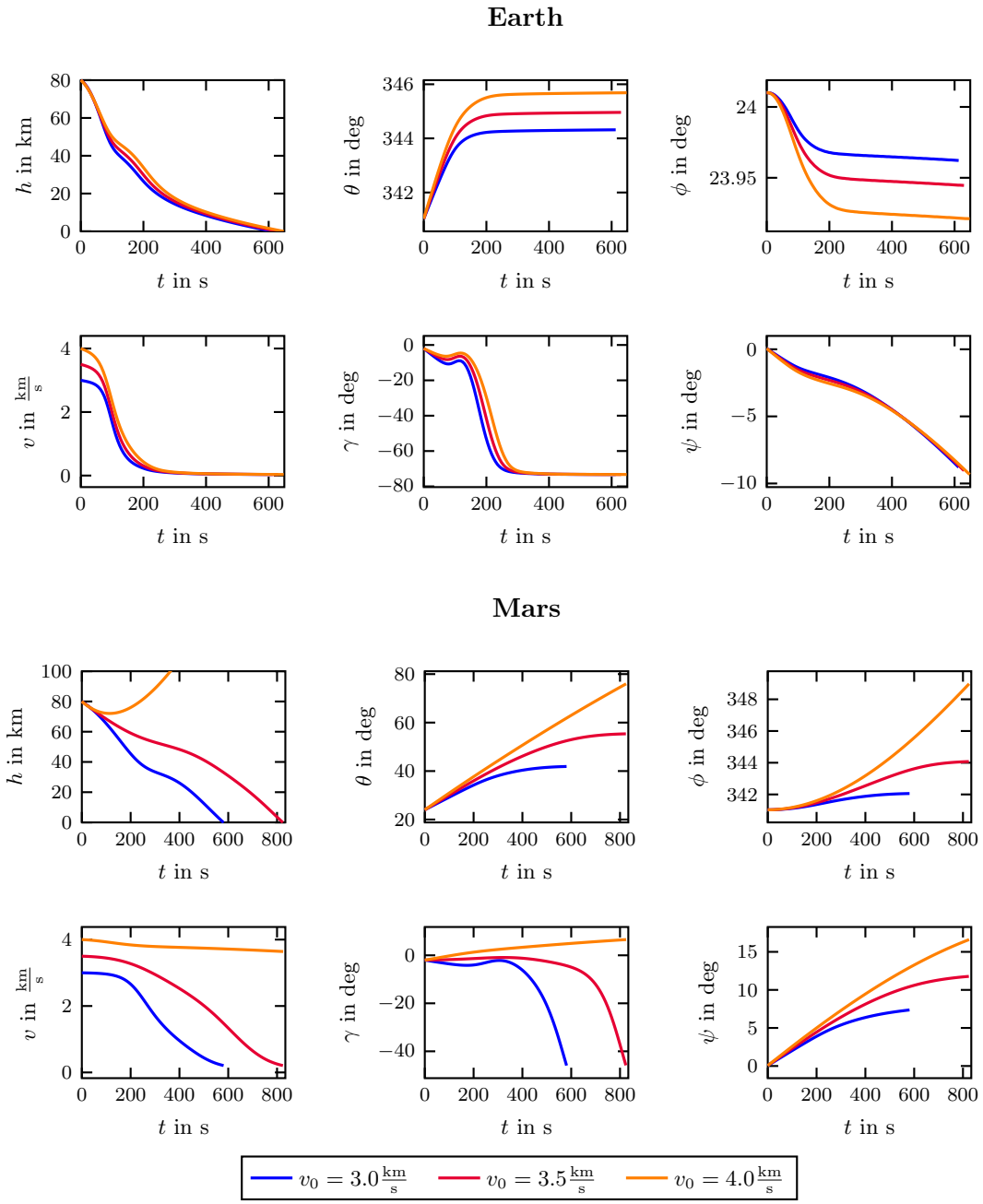

Figure C.3: Re-Entry onto Earth (top) and Mars (bottom) at different entry velocities using the six state model. For Earth the Earth Atmosphere Model (EAM) by NASA and for Mars the model established by Noton is used. The remaining initial conditions are set as $h_0 = 80\text{km}$, $\theta_0 = 341.03°$, $\phi_0 = 24.01°$, $\gamma_0 = -2°$ and $\psi_0 = 0.05°$. The parameters are set as $B_C = 72.8\frac{\text{kg}}{\text{m}^2}$ and $\frac{C_L}{C_D} = 0.3$.

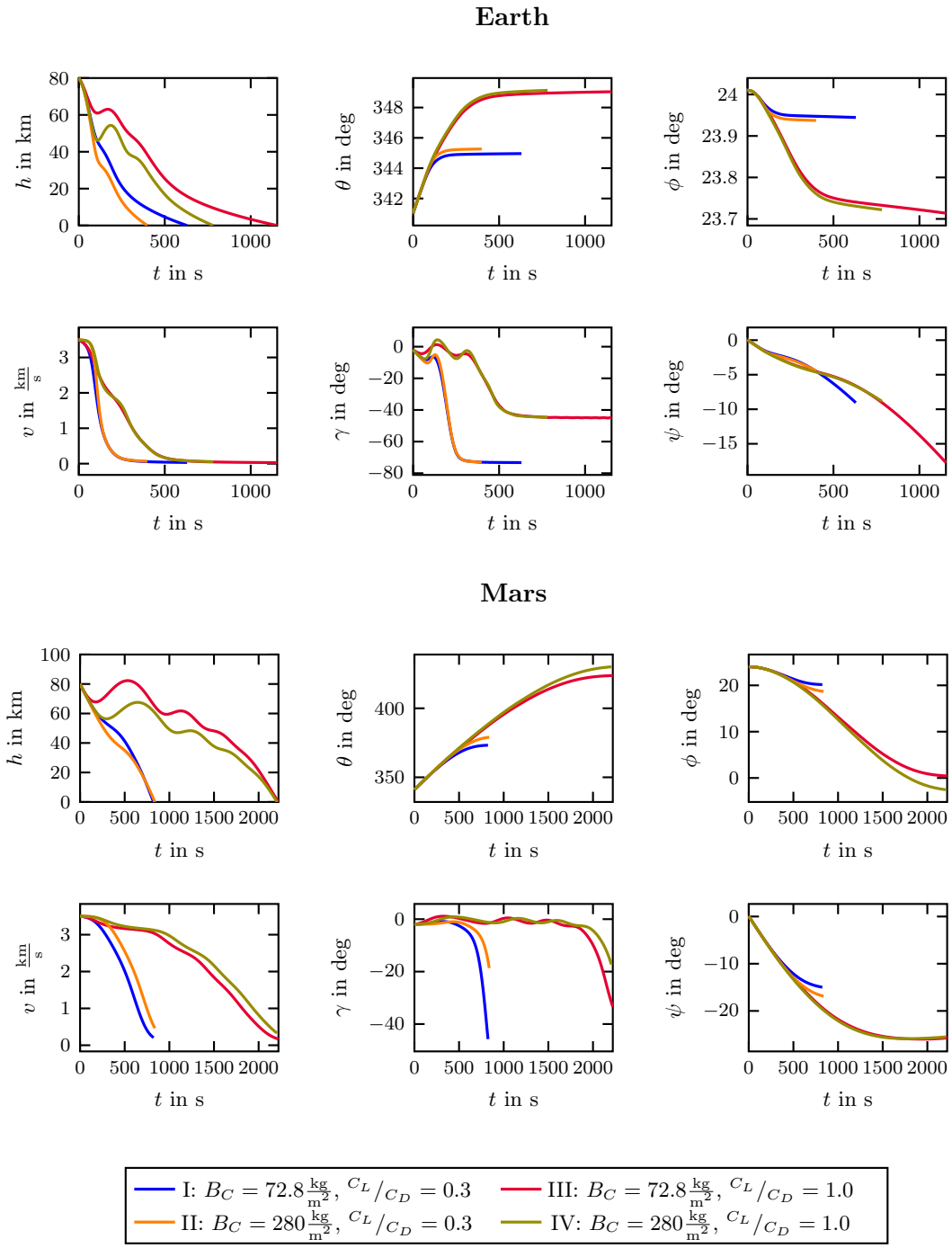

Figure C.4: Re-Entry onto Earth (top) and Mars (bottom) for different B_C and $\frac{C_L}{C_D}$ combinations of the six state model.For Earth the Earth Atmosphere Model (EAM) by NASA and for Mars the model established by Noton is used. Again the initial conditions are set as $h_0 = 80\text{km}$, $\theta_0 = 341.03°$, $\phi_0 = 24.01°$, $v_0 = 3.5\frac{\text{km}}{\text{s}}$, $\gamma_0 = -2°$ and $\psi_0 = 0.05°$.

C.2 Optimal Control Problem

In dependence of the controlled three state model in (4.10) the optimal controlled six state for $t \in [0, t_f]$ yields to

$$\min_{x,t_f} \; t_f + \kappa \int_0^{t_f} u^2(t)\, dt$$

$$\text{subject to} \quad \dot{x} = \begin{pmatrix} \dot{h} \\ \dot{\theta} \\ \dot{\phi} \\ \dot{v} \\ \dot{\gamma_u} \\ \dot{\psi} \end{pmatrix}$$

$$\begin{aligned}
&h(0) = h_0, \;\; h(t_f) = 0, \\
&\theta(0) = \theta_0, \\
&\phi(0) = \phi_0, \\
&v(0) = v_0, \\
&\gamma(0) = \gamma_0, \\
&\psi(0) = \psi_0, \\
&0 \leq x_1 \leq h_0 \\
&\theta_{min} \leq x_2 \leq \theta_{max} \\
&\phi_{min} \leq x_3 \leq \phi_{max} \\
&0 \leq x_4 \leq v_0 \\
&\gamma_{min} \leq x_5 \leq \gamma_{max} \\
&\psi_{min} \leq x_6 \leq \psi_{max} \\
&u_{min} \leq u \leq u_{max}
\end{aligned}$$

The FPA γ_u is influenced directly by the control $u(t)$.

$$\dot{\gamma_u} = \left(\frac{\rho}{2B_c} \frac{C_L}{C_D} v \cos(\alpha) + \cos\gamma \left(\frac{v}{R_0 + h} - \frac{g}{v} \right) \right) + u$$

The second term in the objective function is a regularisation term and smoothes the control $u(t)$ as explained in section 4.2. The box constraints for the latitude, longitude, FPA and VAA are set as

$$\begin{aligned}
0 \leq \theta \leq 360^\circ, \\
0 \leq \phi \leq 180^\circ, \\
-90^\circ \leq \gamma_u \leq 90^\circ, \\
-180^\circ \leq \psi \leq 180^\circ.
\end{aligned}$$

The initial conditions for re-entry onto Earth and Mars are set as

$$\begin{aligned} h_0 &= 80\text{km}, \\ \theta_0 &= 341.03^\circ, \\ \phi_0 &= 24.01^\circ, \\ v_0 &= 3.5\frac{\text{km}}{\text{s}}, \\ \gamma_0 &= -2^\circ, \\ \psi_0 &= 0.0573^\circ. \end{aligned}$$

In figures C.5 to C.8 optimized trajectories for re-entry onto Earth and Mars are displayed for two different lift-to-drag ratios $\frac{C_L}{C_D}$. As atmosphere model the EAM is used for Earth, the model derived by Noton is used for Mars.

In table C.1 all technical details of the optimization using TransWORHP can be found for the case of re-entry onto Mars. All calculations were performed on a computer with the operating system Linux Ubuntu 16.04 utilised with an i7 3.4GHz processor.

	Number of					
***u*(*t*)**	**grid points**	**variables**	**box constraints**	**path constraints**	**iterations**	**CPU time**
oscillating	101	708	1401	600	38	69.3s
smoothed	101	708	1401	600	23	79.3s

Table C.1: Technical details of the optimization of the six state model using TransWORHP for the case of re-entry onto Mars with $\frac{C_L}{C_D} = 0.3$.

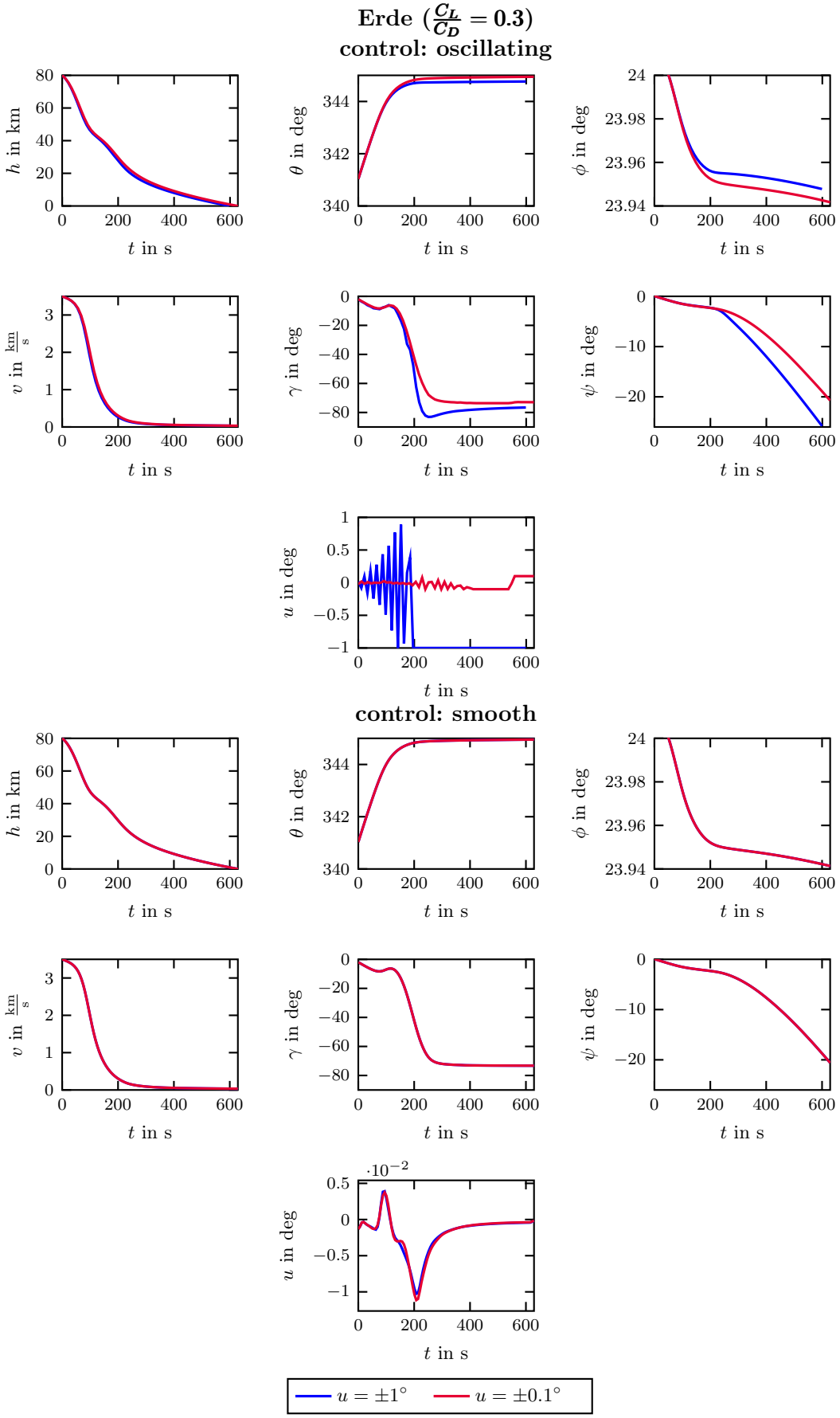

Figure C.5: Controlled re-entry onto Earth with aerodynamic parameters $B_C = 72.8 \frac{\text{kg}}{\text{m}^2}$ and $\frac{C_L}{C_D} = 0.3$. As atmosphere model the Earth Atmosphere Model (EAM) by NASA is used.

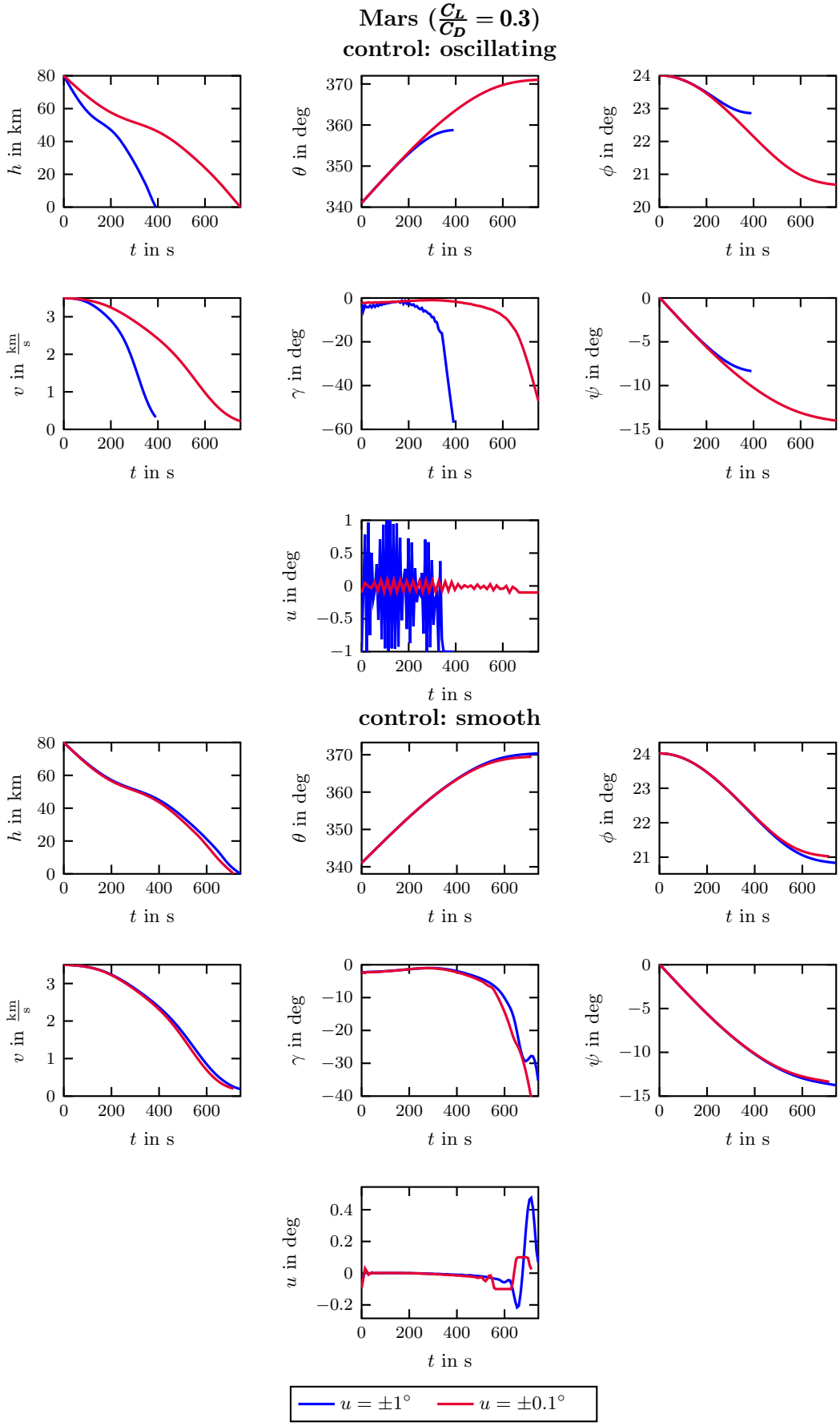

Figure C.6: Controlled re-entry onto Mars with aerodynamic parameters $B_C = 72.8 \frac{\text{kg}}{\text{m}^2}$ and $\frac{C_L}{C_D} = 0.3$. As atmosphere model the one established by Noton is used.

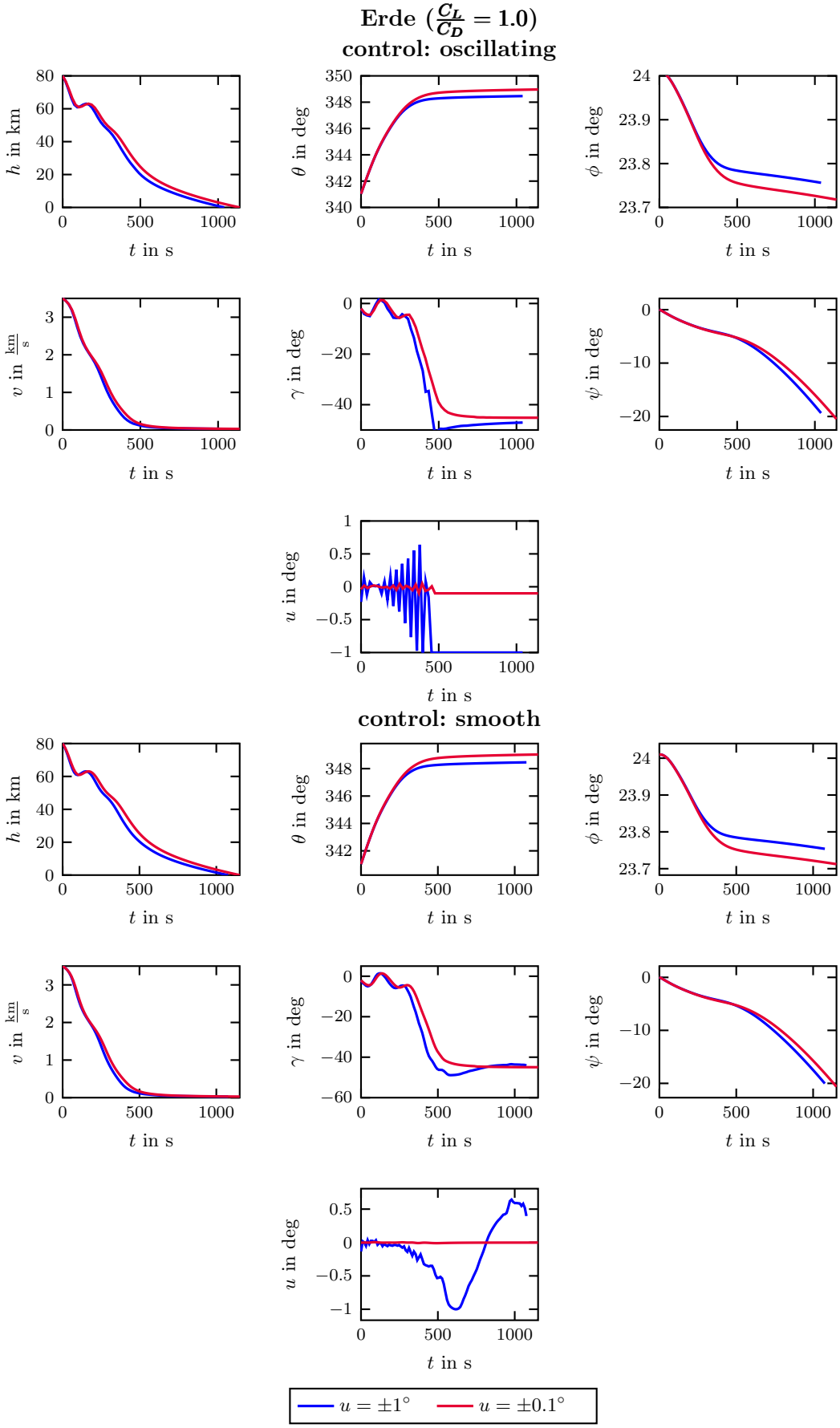

Figure C.7: Controlled re-entry onto Earth with aerodynamic parameters $B_C = 72.8 \frac{\text{kg}}{\text{m}^2}$ and $\frac{C_L}{C_D} = 1.0$. As atmosphere model the Earth Atmosphere Model (EAM) by NASA is used.

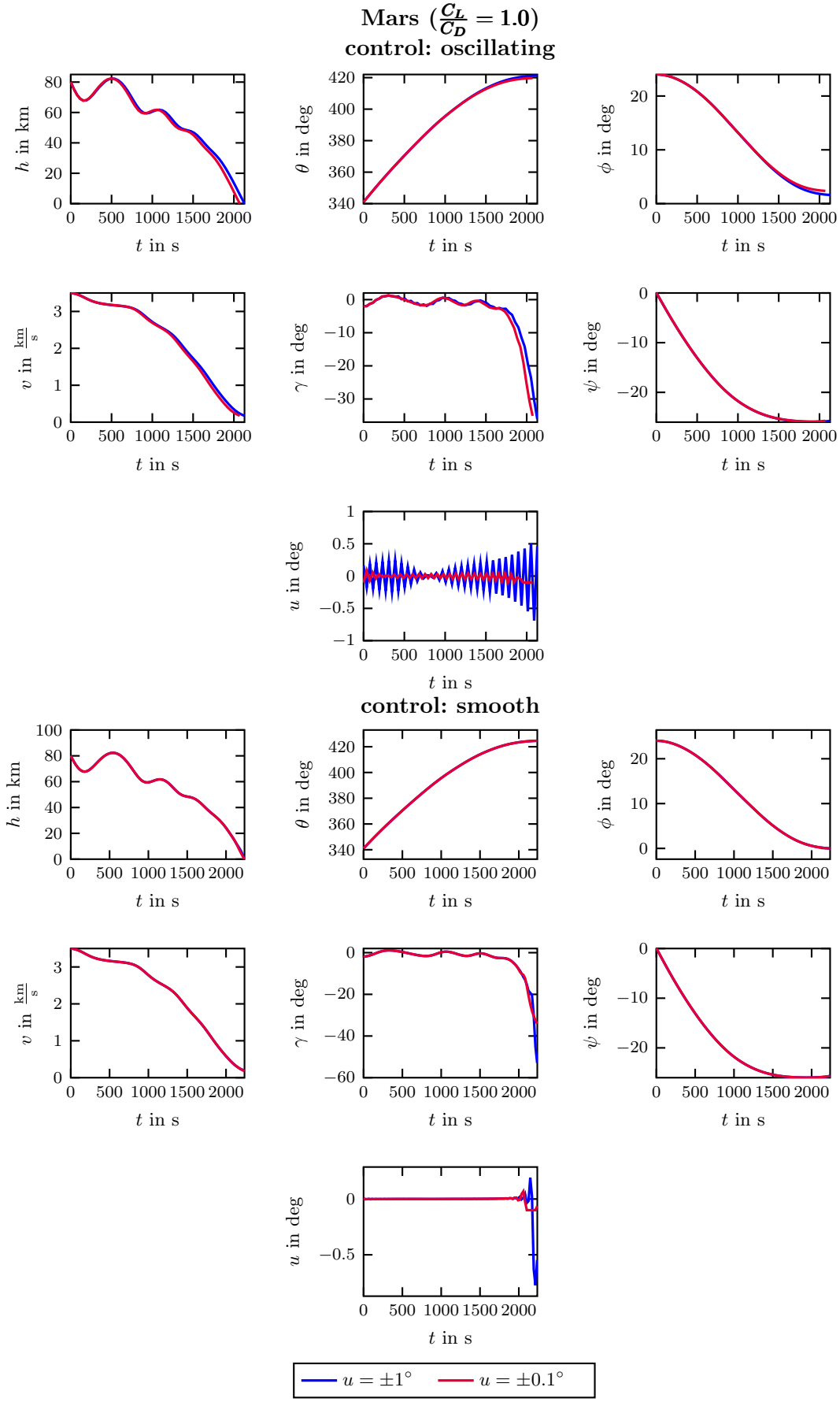

Figure C.8: Controlled re-entry onto Mars with aerodynamic parameters $B_C = 72.8 \frac{\text{kg}}{\text{m}^2}$ and $\frac{C_L}{C_D} = 1.0$. As atmosphere model the one established by Noton is used.

Bibliography

[1] A. Halder, R. Bhattacharya: *Beyond Monte-Carlo: A Computational framework for Uncertainty Propagation in Planetary Entry, Descent and Landing,* Texas A&M University, in: AIAA Guidance, Navigation, and Control Conference, Toronto, Ontario Canada, 2nd – 5th August 2010.

[2] A. Halder, R. Bhattacharya: *Dispersion Analysis in Hypersonic Flight During Planetary Entry Using Stochastic Liouville Equation,* Texas A&M University, In: Journal of Guidance, Control, and Dynamics, Vol. 34, Issue 2, pp. 459-474, 2011.

[3] N. X. Vinh, A. Busemann, R. D. Culp: *Hypersonic and Planetary Entry Flight Mechanics,* University of Michigan Press: 1980.

[4] A. Tarantola, B. Valette: *Inverse Problems = Quest for Information,* Institut de Physique du Globe, Université Pierre et Marie Curie,Paris in Journal of Geophysics, No. 50, pp. 159-170, 1982.

[5] A. Tarantola: *Inverse Problem Theory and Methods for Model Parameter Estimation,* Society for Industrial and Applied Mathematics, Paris: 2005.

[6] M. Ehrendorfer: *The Liouville Equation and Its Potential Usefullness for the Prediction of Forecast Skill. Part I: Theory,* American Meteorological Society: 1994.

[7] M. Ehrendorfer: *The Liouville Equation and Its Potential Usefullness for the Prediction of Forecast Skill. Part II: Application,* Monthly Weather Review, Volume 122: 1994.

[8] M. Ehrendorfer: *The Liouville Equation in Atmospheric Predictability,* Seminar on Predictability of weather and climate, 9-13 September 2002.

[9] D. K. Geller: *Linear Covariance Techniques for Orbital Rendezvous Analysis and Autonomous Onboard Mission Planning,* Utah State University in: Journal of Guidance, Control, and Dynamics, Vol. 29, No.6, 2006.

[10] D. K. Geller: *Linear Covariance Analysis for Powered Lunar Descent and Landing,* Journal of Spacecraft and Rockets, Vol. 46, No. 6 (2009), pp. 1231-1248.

[11] R. Motion: *Returning from Space: Re-entry,* https://www.faa.gov/other_visit/aviation_industry/designees_

delegations/designee_types/ame/media/Section%20III.4.1.7%20Returning%20from%20Space.pdf, called: 26th September 2016.

[12] Z. Papp: *Mission Planner for Heating-Optimal Re-Entry Trajectories with Extended Range Capability,* Master Thesis, Delft University of Technology: 2014.

[13] J. C. Adams: *Atmospheric Re-Entry,* Arnold Engineering Development Center: June 2003.

[14] E. Messerschmid, S. Fasoulas: *Raumfahrtsysteme, Eine Einführung mit Übungen und Lösungen,* 3. Auflage, Springer, Stuttgart: 2009.

[15] L. D. Ely: *Return From Space: An Explanation of Re-entry Problems and Factors of Re-entry Vehicle Design and Performance,* Charles C Thomas Publisher, Springfield, Illinois: 1966.

[16] R. Meisinger, T. Karaca, M. Taufer: *Simulation der Wiedereintrittsbahn der ISS-Rettungskapsel,* Schriftenreihe der Georg-Simon-Ohm-Fachhochschule Nürnberg: 2002.

[17] R. H. Battin: *An Introduction to the Mathematics and Methods of Astrodynamics,* Revised Edition, MIT, AIAA Education Series: Reston 1999.

[18] N. X. Vinh: *Optimal Trajectories in Atmospheric Flight,* Department of Aerospace Engineering, University of Michigan, Elsevier Scientific Publishing Company: 1981.

[19] M. Noton: *Spacecraft Navigation and Guidance,* Advances in Industrial Control, Springer Verlag: 1998.

[20] A. Tewani: *Atmospheric and Space Flight Dynamics: Modelling and Simulation with MATLAB and Simulink,* Springer: 2007.

[21] W. Demtröder: *Experimentalphysik 1, Mechanik und Wärme,* 5., neu bearbeitete und aktualisierte Auflage, Springer, Kaiserslautern: 2008.

[22] N. Henze: *Stochastik für Einsteiger,* Springer Fachmedien Wiesbaden: 2013.

[23] H.-O. Georgii: *Stochastik: Einführung in die Wahrscheinlichkeitstheorie und Statistik,* 4. überarbeitete und erweiterte Auflage, Walter de Gruyter, Berlin: 2009.

[24] A. Klenke: *Wahrscheinlichkeitstheorie,* 3. Auflage, Springer Spektrum, Mainz: 2013.

[25] J. Hartung, B. Elpelt: *Multivariate Statistik: Lehr- und Handbuch der angewandten Statistik,* 7. unveränd. Auflage, Oldenbourg, München: 2007

[26] U. Krengel: *Einführung in die Wahrscheinlichkeitstheorie und Statistik,* 8. Auflage, Vieweg + Teubner Verlag: 2007.

[27] F. Schwabl: *Statistische Mechanik,* 3. Auflage, Springer Lehrbuch, München: 2006

[28] G. Leitmann, et. al.: *Optimization Techniques, with Applications to Aerospace Systems,* Academic Press, New York: 1962.

[29] M. Papageorgiou, M. Leibold, M. Buss: *Optimierung; Statistische, dynamische, stochastische Verfahren für die Anwendung,* 3. Auflage, Springer Vieweg, München/Chania(Griechenland): 2012.

[30] C. Büskens: *Optimierung dynamischer Systeme,* Vorlesungsskript, Universität Bremen: 2015.

[31] J. T. Betts: *Practical Methods for Optimal Control and Estimation Using Nonlinear Programming,* Second Edition, Society for Industrial and Applied Mathematics, Philadelphia: 2010.

[32] H. R. Schwarz, W. Köckler: *Numerische Mathematik,* 8. Auflage, Teubner Verlag, Wiesbaden: 2011.

[33] J. Nocedal, S. J. Wright: *Numerical Optimization,*Springer: 1999.

[34] M. Knauer: *Optimierung in Weltraumanwendungen,* Vorlesungsskript, Universität Bremen: 2012.

[35] D. Wassel: *Numerik der hochdimensionalen, nichtlinearen Optimierung,* Vorlesungsskript, Universität Bremen: 2014.

[36] S. Roy: *Parameter Identification and Optimisation in Robotics,* Vorlesungsskript, Universität Bremen: 2016.

[37] G. Fasano, J. D. Pinter: *Modeling and Optimization in Space Engineering,* Springer Optimization and Its Applications, Volume 73: 2013.

[38] W. Alt, C. Schneider, M. Seydenschwanz: *EAGLE-STARTHILFE Optimale Steuerung: Theorie und numerische Verfahren,* 1. Auflage, Edition am Gutenbergplatz Leipzig: 2013.

[39] M. Gerdts: *Optimale Steuerung,* Vorlesungsskript, Universität Würzburg, Wintersemester 2009/ 2010.

[40] C. Büskens: *Optimierungmethoden und Sensitivitätsanalyse für optimale Steuerprozesse mit Steuer- und Zustands-Beschränkungen,* Dissertation, Westfälische Wilhelms-Universität Münster, 1998.

[41] *Users' Guide to WORHP 1.9,* Steinbeis Forschungszentrum Optimierung, Steuerung und Regelung: 2016.

[42] M. Knauer, C. Büskens: *From WORHP to TransWORHP,* In: Proceedings of the 5th International Conference on Astrodynamics Tools and Techniques, 2012.

[43] M. Knauer: *TransWORHP - User Guide,* Steinbeis-Forschungszentrum für Optimierung, Steuerung und Regelung, Version: 2. Februar 2017

[44] J. W. Wittwer: *Monte Carlo Simulation Basics,* June 1, 2004, https://www.vertex42.com/ExcelArticles/mc/MonteCarloSimulation.html, called: 4th January 2017.

[45] P. C. Knocke, G. G. Wawrzyniak, B. M. Kennedy, P. N. Desai, T. J. Parker, M. P. Golombek, T. C. Duxbury, D. M. Kass: *Mars Exploration Rovers Landing Dispersion Analysis,* AIAA 2004-5093, AIAA/AAS Astrodynamics Specialist Conference and Exhibit, Providence, Rhode Island, August 16-19th, 2004.

[46] J. E. Potter: *Space Guidance Analysis Memo # 29, Subject: Error Ellipsoids,* Massachusetts Institute of Technology, Instrumentation Laboratory: 1962.

[47] D. R. Williams: *Planetary Fact Sheet – metric,* NASA Goddard Space Flight Center, http://nssdc.gsfc.nasa.gov/planetary/factsheet/, called: 12th October 2016.

[48] G. Tiruneh: *Explaining Planetary-Rotation Periods Using an Inductive Method,* Department of Political Science, University of Central Arkansas, https://arxiv.org/pdf/0906.3531v3.pdf, called: 12th October 2016.

[49] Nancy Hall: *Mars Atmosphere Model, Metric Units,* NASA Glenn Research Center, https://www.grc.nasa.gov/www/k-12/airplane/atmosmrm.html, called: 5th October 2016.

[50] C. G. Justus: *Mars Global Reference Atmospheric Model for Mission Planning and Analysis,* presented Paper at AIAA 28th Aerospace Sciences Meeting, Reno, NV, Jan. 8-11, 1990.

[51] C. G. Justus, A. Duvall, V. W. Keller: *Atmospheric Models for Mars Aerocapture,* Morgan Research Corporation, NASA Marschall Space Flight Center: 2005.

[52] Nancy Hall: *Earth Atmosphere Model, Metric Units,* NASA Glenn Research Center, https://www.grc.nasa.gov/www/k-12/airplane/atmosmet.html, called: 16th January 2017.

[53] R. A. Braeunig: *Atmospheric Properties,* http://www.braeunig.us/space/atmos.htm, called: 16th January 2017.

[54] N. Papitashvili: *NRLMSISE-00 Atmosphere Model,* http://ccmc.gsfc.nasa.gov/modelweb/models/nrlmsise00.php, called: 17th January 2017.

[55] R. A. Braeunig: *Basics of Space Flight,* http://www.braeunig.us/space/atmmodel.htm, called: 16th January 2017.

[56] Nancy Hall: *Lift to Drag Ratio,* NASA Glenn Research Center,https://www.grc.nasa.gov/www/k-12/airplane/ldrat.html, called: 27th April 2017.

[57] Nancy Hall: *The Drag Coefficient,* NASA Glenn Research Center,https://www.grc.nasa.gov/www/k-12/airplane/dragco.html, called: 27th April 2017.

[58] Nancy Hall: *The Lift Coefficient,* NASA Glenn Research Center,https://www.grc.nasa.gov/www/k-12/airplane/liftco.html, called: 27th April 2017.

[59] S. Reza, R. Hund, F. Kustas, W. Willcockson, J. Songer: *Aerocapture Inflatable Decelerator for Planetary Entry,* American Institute of Aeronautics and Astronautics.

[60] S. Gaddis: *Hypersonic Inflatable Aerodynamic Decelerator (HIAD).* https://gameon.nasa.gov/projects-2/archived-projects-2/hypersonic-inflatable-aerodynamic-decelerator/, called: 2nd June 2016.

[61] European Space Agency: *The Hazards of Landing on Mars,* http://exploration.esa.int/mars/58307-the-hazards-of-landing-on-mars/, called: 19th May 2017.

[62] European Space Agency: *Exomars 2018: Landing Site Search to Narrow,* http://exploration.esa.int/mars/56622-exomars-2018-landing-site-search\-to-narrow/, called: 19th May 2017.

[63] European Space Agency: *ESA Reentry Vehicle on Track for Flight in 2013,* http://www.esa.int/Our_Activities/Space_Transportation/ESA_reentry_vehicle_on_track_for_flight_in_2013, called: 19th May 2017.

Eidesstattliche Erklärung

Hiermit versichere ich an Eides statt, dass ich die vorliegende Arbeit selbständig verfasst und ausschließlich die angegebenen Quellen und Hilfsmittel verwendet habe.

Bremen, den 12. July 2017